August 2020

Rigidity in Frictional Particle Packings and Dynamics in Living Polymeric Packings

Kuang Liu
Syracuse University

Recommended Citation

Liu, Kuang, "Rigidity in Frictional Particle Packings and Dynamics in Living Polymeric Packings" (2020). *Dissertations - ALL*. 1239.
https://surface.syr.edu/etd/1239

Abstract

As indicated by the title, this is a thesis in two acts. The first act encapsulates a study of the rigidity transition in frictional particle packings, or how a packing goes from floppy-to-rigid as its particle density increases, for example. While consensus has emerged regarding the nature of the rigidity transition in frictionless packings, there is much less consensus with frictional packings. Therefore, I introduce two new complementary concepts, frictional rigidity percolation and minimal rigidity proliferation, to help identify the nature of the frictional rigidity transition. To probe frictional rigidity percolation, I construct rigid clusters using a (3,3) pebble game for sliding and frictional contacts first on a honeycomb lattice with next-nearest neighbors, and second on a hierarchical lattice. For both lattices, I find a continuous rigidity transition. My numerically obtained transition exponents for frictional rigidity percolation on the honeycomb lattice are distinct from those of frictionless/central-force rigidity percolation. I propose that localized motifs, such as hinges connecting rigid clusters that are allowed only with friction, could give rise to this new frictional universality class. I also develop a minimally rigid cluster generating algorithm invoking generalized Henneberg moves, dubbed minimal rigidity proliferation. For both frictional and central-force rigidity percolation, these clusters appear to be in the same universality class as connectivity percolation, suggesting superuniversality between all three transitions for such minimally rigid clusters. These combined results allow me to directly compare two universality classes on the same lattice in rigidity percolation, for the first time.

Grounded in this lattice work, I then turn towards identifying and analyzing rigid clusters within experimental packings to determine what aspects of the simpler lattice models are experimentally relevant. I use two approaches to identify the rigid clusters. Both approaches, the force-based dynamical matrix and the coordination-based rigidity percolation, agree with each other and identify similar rigid structures. As the system becomes jammed, at a contact number of $z = 2.4 \pm 0.1$, a rigid backbone interspersed with floppy, particle-filled holes of a broad range of sizes emerges, creating a sponge-like morphology. I also find that the pressure within rigid structures always exceeds the pressure outside the rigid structures, i.e. that the backbone is load-bearing. These findings show that continuous transition observed in the lattice models persists in experiments and that mechanical stability arises through arch structures and hinges at the mesoscale.

In the second act of this thesis, I turn towards biology for inspiration, namely biology in the form of the cell nucleus. The cell nucleus houses chromatin, which is linked to a protein shell called the lamina. Protein motors and chromatin binding proteins in the nucleus are thought to drive correlated chromatin dynamics and nuclear shape fluctuations. To test this notion, we develop a minimalistic model in which an active, crosslinked Rouse chain linked to a polymeric shell. System-scale correlated motion occurs and requires both motor activity and crosslinks. Contractile motors, in particular, enhance chromatin dynamics by driving anomalous density fluctuations. Nuclear shape fluctuations depend on motor strength, crosslinking, and chromatin-lamina linkage. Complex chromatin dynamics and nuclear shape, therefore, both emerge from this minimal, yet composite, system.

Rigidity in Frictional Particle Packings and Dynamics in Living Polymeric Packings

by

Kuang Liu

B.S., Peking University, 2013

Dissertation

Submitted in partial fulfillment of the requirements for the degree of

Doctor of Philosophy in Physics

Syracuse University

August 2020

Contents

Chapter 1

Introduction

Let us begin with the first act on the nature of the frictional rigidity, or jamming, transition. I will first discuss the notion of emergence of rigidity in disordered networks and then move on to discuss rigidity, or jamming, in particulate systems with no friction in order to lay the groundwork for subsequent chapters.

1.1 Rigidity in networks

FIVE YEARS LATER as I face the computer, I remember that distant winter afternoon when I borrowed *Introduction to Percolation Theory* from the library. At that time, I was a second-year graduate student. Many department buildings, built on the hill by Marshall Street with its many restaurants, were covered by snow and so white and enormous, like works of art. Every weekend, one of my roommates, whose major was chemistry, would pour lots of magnetic bars and steel balls on a large table and would display how he constructed a large molecule from many small pieces. He compressed or stretched the molecules and some times it deformed easily, while other times it did not. "It's simply a matter of waking up the structure's rigidity." I explained.

——Homage to *ONE HUNDRED YEARS OF SOLITUDE*

1.1.1 Connectivity percolation

For network structures at different length scales, from bridges to the cell cytoskeleton, it is key for functionality to maintain shape under stress. Physicists are interested in studying the process by which the rigidity of individual bars/springs/components emerges in a network at the system-wide scale, i.e. spanning it. The concept of spanning is distinct from rigidity since it only relies on connectivity. The study of the emergence of system-wide connectivity is called **percolation**, which was first developed by Flory and Stockmayer [1, 2] to describe how small molecules react to form larger molecules. Later, this concept was applied to lattice models and the field of connectivity percolation evolved rapidly. In a network composed of nodes and with bonds between nodes, if there is no occupied bond, there is certainly no connected path spanning the network. With increasingly more bonds on the network being occupied, finite clusters, or groups of connected occupied bonds but disconnected from each other, emerge until, finally, at least one connected cluster spanning the entire network emerges. This emergence is identified as the connectivity percolation transition. An example of this emergence on a two-dimensional square lattice is shown in Fig 1.1.

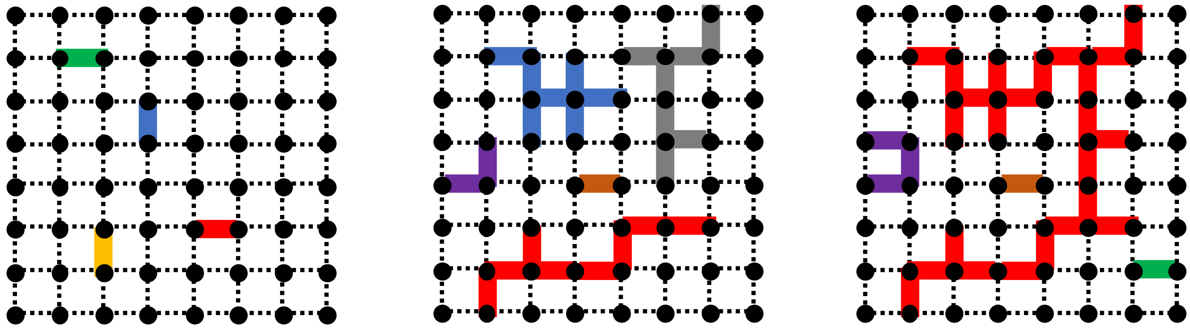

FIGURE 1.1: Schematic for connectivity percolation in a finite 2d square lattice. Bonds with same color belong to the same cluster. Dotted bonds are not occupied. Left: Only a few bonds are occupied. Middle: Some finite-sized clusters emerge. Right: There is a spanning cluster colored red.

Usually in percolation theory, the number of occupied bonds is controlled by the probability for one bond to be occupied, denoted as p. There exists a critical p_c at which the percolation transition occurs. Specifically, for bond percolation on an infinitely large square lattice, $p_c = 1/2$, i.e. the occupation probability at which an infinitely-large cluster emerges. Typically, the probability that a bond a distance r from an occupied bond belongs to the same finite cluster is to the order of $exp(-r/\xi)$, where ξ is defined as the correlation length. Near the transition point, $\xi \sim |p - p_c|^{-\nu}$ with ν as a key scaling exponent characterizing the connectivity percolation transition and called the correlation length exponent. For percolation in two-dimensions, rigorous arguments yield $\nu = 4/3$ and serve as a check on the numerical results [3, 4, 5]. It turns out that the connectivity percolation transition is a continuous one, which is consistent with the divergence of the correlation length at the transition.

Connectivity percolation requires only a connectivity between nodes via occupied bonds, while rigidity in a network structure demands more than that. It demands that the connected structure span the network and that the structure be rigid in the sense that the connected structure retain its shape under some small amount of strain. We can, of course, debate how small is small. I will sweep this technical point under the rug for now. To probe this demand, the occupied bonds become springs to which strain can be applied and one can study the emergence of a rigid, spanning structure, i.e. a rigidity percolation transition. Given the above discussion about connectivity percolation, we ask: What kind of transition is the rigidity percolation transition? Is it a continuous transition? If so, it is in the same universality class as connectivity percolation, i.e. the exponents, such as the correlation length exponents, are the same? Or, is the rigidity percolation transition a discontinuous one? To answer these questions, let me now be more specify, more concretely, rigidity percolation.

1.1.2 Central-force rigidity percolation

Spring networks are the basis of many man-made materials. Network structures composed of bars, or infinitely stiff springs, connected at nodes are very common in bridges, scaffolds, and wood house roofs. Random spring networks are common in living systems, such as the cellular cytoskeleton. In such networks, rigidity is obtained because it costs energy for the bars/springs in the network to stretch, compress or bend. Forces due to the tensile or compressive stiffness of the bars belong to **central forces**, while forces related to the bending of springs belong to **angular forces**. A randomly-diluted lattice is considered as a simplified network to study various features of disordered spring networks. By randomly occupying now springs in a triangular lattice, in Fig 1.2 I construct a two-dimensional minimal rigid structure between two plates that has a nonzero bulk modulus under applied pressure. On the left, I use angular springs, and on the right I use springs that can freely rotate at the nodes. With angular springs, we only need two bonds occupied, which also trivially satisfies connectivity percolation, while with central forces, a more complex structure is required to be rigid. Let us now, therefore, focus on central-force rigidity percolation.

The simplest way to model a central-force network is to consider bonds between neighboring nodes in a network to be identical springs. Rigidity percolation in such elastic network is achieved once there is nonzero shear modulus and bulk modulus. In 1984, Feng and Sen did numerical simulations to study central-force rigidity percolation in a diluted two-dimensional triangular lattice [6]. They found that the bulk and shear modulus vanish with some scaling exponent at a threshold p_c, which is critical bond occupancy probability (and different from the connectivity percolation p_c). Specifically $K, G \sim (p - p_c)^f$ when $p > p_c$, where K and G are the bulk modulus and the shear modulus, respectively. They also showed that p_c and f varies for different

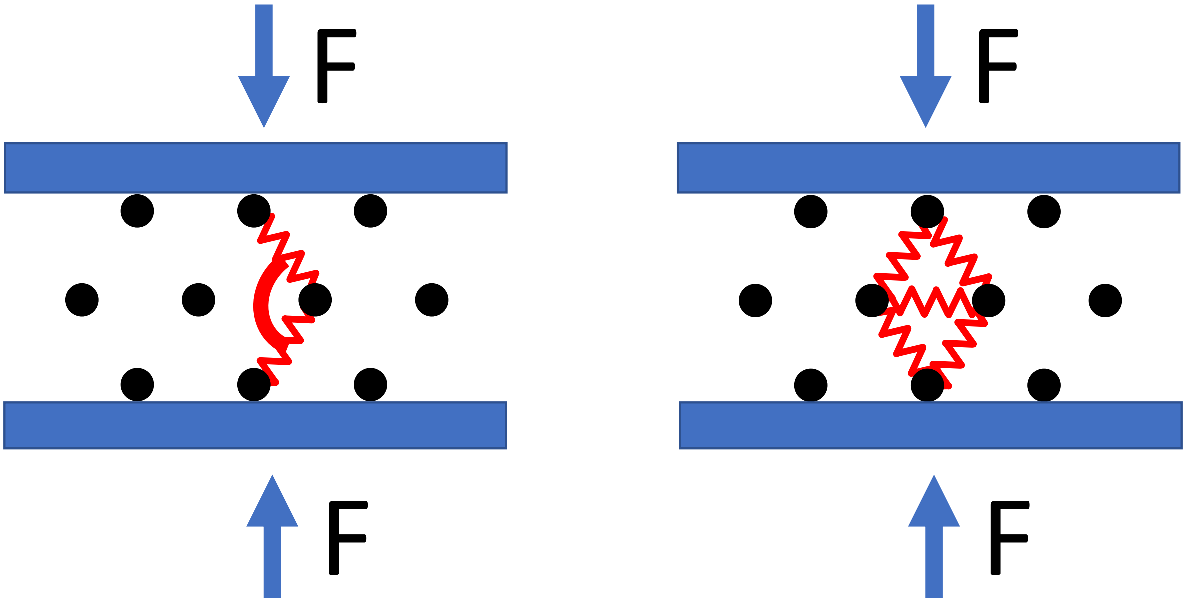

FIGURE 1.2: Schematic for rigidity percolation. Left: minimal rigid structure in angular-force-dominated rigidity percolation. Right: minimal rigid structure in central-force rigidity percolation.

lattice types. In addition to exponent f, there are other exponents ν and β to quantify the rigidity transition. The correlation length ξ behaves as $\xi \sim |p-p_c|^{-\nu}$ around p_c, just as with connectivity percolation. The fraction of bonds in the spanning rigid cluster, denoted as P_∞, behaves as $P_\infty \sim (p-p_c)^\beta$ for $p \geq p_c$ and near the transition. The exponent β is known as the order parameter exponent. To understand central-force rigidity percolation analytically, in 1985, Feng, Thorpe and Garboczi developed an effective-medium theory of percolation in central-force elastic networks [7]. Even though the theory demands that fluctuations in displacements vanish, i. e. it is a mean field approach, the theory gives an description of the shear modulus and bulk modulus that matches numerical results very well. See Fig. 1.3. This analysis suggests that the central-force rigidity transition is a continuous transition.

Rather than going through the nuts and bolts of effective medium theory, let's look at an exactly solvable, yet somewhat artificial, model of central-force rigidity percolation. Let us start with the construction of a particular hierarchical lattice known as the

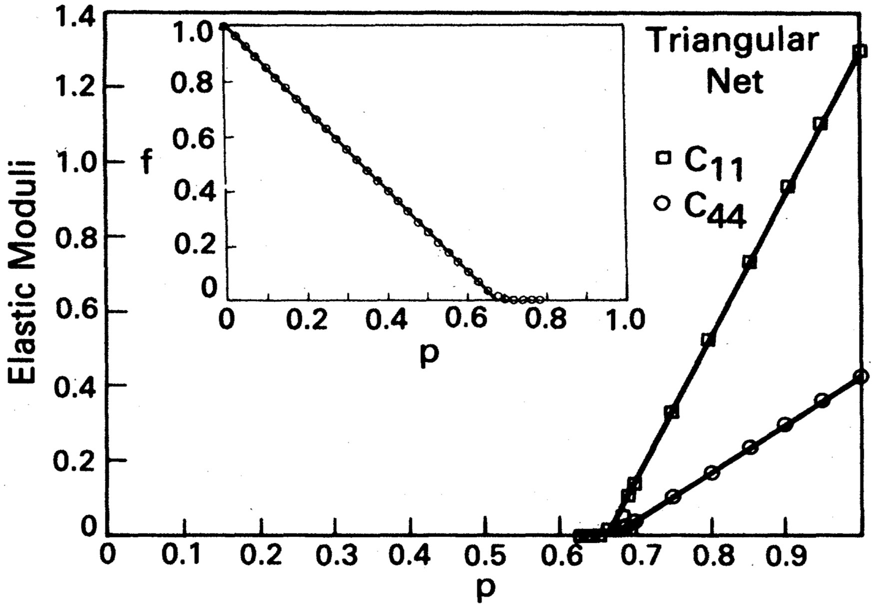

FIGURE 1.3: C_{11} and C_{44} represent the bulk and shear modulus respectively from numerical results. Lines are from effective-medium theory. The inset is fraction of zero-frequency modes averaged from triangular networks. [7]

Berker lattice. [9] Given two points and a bond, as in Figure 2.11a, replace the bond with some additional structure to generate the first generation hierarchical structure. This replacement continues ad infinitum to arrive at a network with an infinite number of sites between two initial points. For this particular lattice, the n^{th} generation contains 8^n bonds (with the exception of $n = 0$). To embed this lattice in two-dimensions, the bond length decreases with each generation.

To analyze rigidity in this hierarchical lattice, assume each bond has a probability $p < 1$ to be occupied. In the $n = 0$ graph, the probability of having a spanning rigid cluster between the two ends (black dots) is $p_0 = p$. In the $n = 1$ graph, the probability of being rigid between two ends can be found by subgraph counting: If all eight bonds are occupied in the $n = 1$ network, there is a spanning rigid cluster between the two ends. The probability of such a structure existing is p^8, while the probability for any bond belonging to the spanning rigid cluster is 1. All other subgraphs that contain

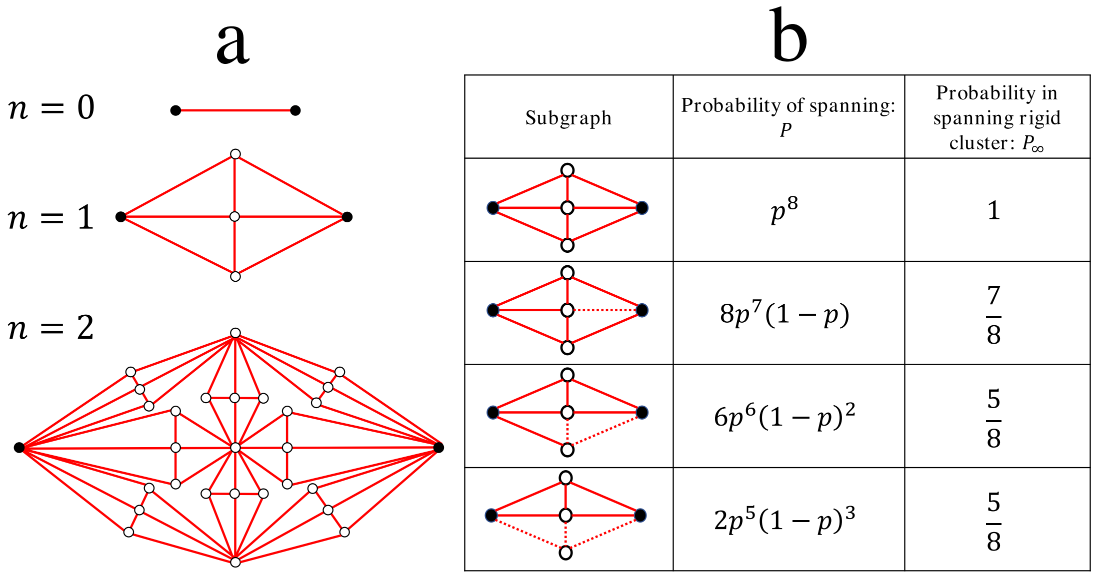

Subgraph	Probability of spanning: P	Probability in spanning rigid cluster: P_∞
	p^8	1
	$8p^7(1-p)$	$\frac{7}{8}$
	$6p^6(1-p)^2$	$\frac{5}{8}$
	$2p^5(1-p)^3$	$\frac{5}{8}$

FIGURE 1.4: *Central-force rigidity percolation on a hierarchical lattice.* (a) First three generations of hierarchical Berker lattice. (b) Subnetwork counting: dashed bonds are not occupied. Every type of subnetwork is a way to obtain a spanning rigid network between two ends(black dots) and its probability is calculated, as well as the probability for an occupied bond to be in the spanning rigid cluster. [8]

a spanning rigid cluster and their respective probabilities are listed in Figure 2.11b. Summing up all ways of having a spanning rigid cluster between the two ends of the $n = 1$ graph, we obtain $p_1 = 2p^5 + 2p^7 - 3p^8$. Given the hierarchical structure of the lattice, it is trivial to generalize this relation to $p_{n+1} = 2p_n^5 + 2p_n^7 - 3p_n^8$, from which we can solve for a fixed point, $p_c = 0.9446$, as the system approaches the thermodynamic limit, i.e. $p_{n+1} = p_n$.

In such way p_n will converge to a step function which jumps from 0 to 1 at p_c as n goes to infinity. Meanwhile, we use $P_R(p)$ to denote the probability for a bond to belong to the spanning rigid cluster. By similar argument we can obtain the recurrence relation for $P_R(p)$ is $P_{R,n+1}(p) = \lambda P_{R,n}(p)$. Near p_c, $\lambda = 0.9554 < 1$ demonstrates that the probability of a bond belonging to the spanning rigid network will approach zero as p approaches p_c. This trend suggests a continuous transition, as discussed above.

Expanding about p_c in both recurrence relations leads to $(p_{n+1} - p_c) = \lambda_1(p_n - p_c)$

and $P_{n+1}(p) = \lambda_2 P_n(p)$ such that $\lambda_1 = b^{1/\nu}$, $\lambda_2 = b^{-\beta/\nu}$, and $\lambda_3 = b^{d_f}$, where d_f is the fractal dimension of spanning rigid cluster at the transition and b is the length scaling factor from one generation of the hierarchical lattice to the next. For the Berker lattice, $\lambda_3 = 8$. We can therefore determine $\beta = -log(\lambda_2)/log(\lambda_1)$ and $\nu d_f = log(\lambda_3)/log(\lambda_1)$, which are both quantities that are independent of b, resulting in $\beta = 0.078$ and $\nu d_f = 3.533$. We now know the order parameter exponent β and a relationship between two additional exponents.

1.1.3 Pebble game and rigid cluster decomposition

During a rigidity percolation process, with more and more springs being added to the lattice, it is useful to think about how and when isolated springs are connected locally and finally exhibit rigidity at the system-size scale. According to the Maxwell counting method [10], in the d-dimensional central-force rigidity percolation problem, a network with N nodes and B bonds/springs has dN free motion modes in total, i.e. or dN degrees of freedom. These free motion modes can be constrained by springs. A key quantity to understanding rigidity is, therefore, the number free/floppy modes per degree of freedom, denoted as f. With enough constraints, f drops to zero such that the network becomes rigid. Assuming the bond occupation probability is p and the average coordination number of network is z, then f is given by $f = (dN - \frac{1}{2}Nzp - dNn_r)/(dN) = 1 - p/p^* + n_r$, where n_r represents the redundant bonds per degree of freedom. Therefore, $p_c^* = 2d/z$ gives an approximation of the location of the rigidity transition point, assuming $n_r = 0$. This estimated p_c^*, also known as the **isostaticity point**, typically gives a lower bound of the rigidity transition point because not all bonds are independent constraints and there are some redundant bonds. For example, in a square with all four edge bonds and two diagonal bonds occupied, any five among six bonds are independent constraints and the sixth bond is a redundant constraint. Given this fact, developing a method to check bonds individually to determine whether or not they are an independent constraint is necessary to pinpoint the location of the rigidity transition.

In terms of small rigid structures, it's easy to imagine that a triangle is the smallest minimal rigid structure composed of multiple springs. But it's hard to imagine whether the structure can bear stress or not if there are hundreds of springs. Going back to 1970, Laman investigated the combinatorial properties of rigid plane skeletal structures and mathematically proved Laman's theorem [11], which gives a necessary and sufficient condition on rigidity. Specifically, a random network consists of N nodes and B bonds, where $B = 2N - 3$, is rigid if and only if any sub-network with n nodes and b bonds satisfies $b = 2n - 3$. Note that Laman's theorem can identify instantaneous rigidity of a network under infinitesimal perturbation regardless how perturbation is applied. Also the theorem deals with connectivity but not position of nodes, so it holds for generic networks, i.e network without any symmetry, and there is no degeneracies of motion modes for nodes. In the two-dimensional central-force rigidity percolation problem, this theorem offers a guideline that rigid structures in a very large network can be found by checking the conditions stated in the theorem. There are also other routes as well, such as Callandine's theorem [12].

Invoking Laman's theorem, in 1995 Jacobs and Thorpe implemented the pebble game, which is a powerful algorithm to track rigidity in a random 2d central-force network [13]. Generally, each node in the network is assigned with **two** pebbles, representing the two free motion modes. Then they assign pebbles to bonds connecting the nodes to mimic the process that the free motion modes are constrained by bonds using rules that will be discussed in detail in Chapter 2. Finally, they count pebbles left in the network to determine its rigidity. If there are only **three** free pebbles left, the network is rigid since two global translational modes and one global rotational mode are trivially rigid. If there are more than 3 pebbles left, it is floppy. This algorithm is called (2,3) pebble game with 3 trivial global free motions and 2 pebbles on each node. The advantage of (2,3) pebble game is it can evaluate the rigidity of network in a programmed way and only relying on the connectivity, or topology, of the network. No explicit forces are required. An example of rigid cluster decomposition using (2,3) pebble game in a honeycomb lattice is shown in Fig 1.5. In this sample, bonds between nearest neighbors and between**next nearest neighbors**(**NNN**) are occupied with the same probability. Different colors represent different rigid clusters computed from the (2,3) pebble game. Nodes colored black belong to the largest rigid cluster, while grey belong to smaller rigid clusters. Note that from left to right rigid cluster spans the system with only one bond added, shown in the red circle. The fraction of of bonds in the largest rigid cluster jumps from a small number to almost 1, which indicates a discontinuous rigidity transition. Details will be discussed in Chapter 2.

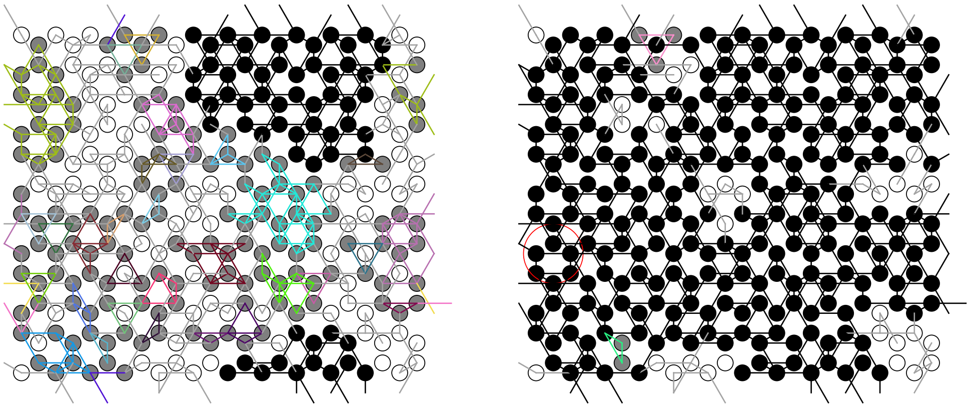

FIGURE 1.5: Rigid cluster decomposition in a honeycomb lattice with next-nearest-neighbors. Left: Before the transition. Right: At the transition.

When Jacob and Thorpe applied the pebble game to the generic triangular lattice [14], they found that the rigidity percolation occurs at $p_c = 0.6602 \pm 0.0003$. Moreover, the correlation length exponent is $\nu = 1.21 \pm 0.06$ and the fractal dimension of the spanning rigid cluster is $d_f = d - \beta/\nu = 1.86 \pm 0.02$. The order parameter exponent $\beta = 0.18 \pm 0.02$. They concluded that central-force rigidity percolation is a continuous transition and is a different universality class from connectivity percolation with $\nu = 4/3$ and $\beta = 5/36$. In 1995 Moukarzel and Duxbury studied the stressed backbone of random central-force systems [15]. They supplemented used a cluster labeling algorithm. A key step in their algorithm is to determine whether a newly-added bond is redundant with respect to the bonds that are already in the network. In this way, a stressed backbone can be obtained. They estimated that $\nu = 1.16 \pm 0.03$ and $d_f = 1.78 \pm 0.02$, which are close, but a bit different to Jacob and Thorpe's results. These differences could come from their estimate of p_c since p_c in an infinite network is unknown. It turns out that p_c can be extracted from the finite-size scaling function $|p_c^L - p_c| \sim L^{-1/\nu}$ after ν is extracted from $\Delta(L) = \sqrt{\overline{p_c^{L^2}} - \overline{p_c^L}^2} \sim L^{-1/\nu}$, where p_c^L is the critical probability found in a system with size L.

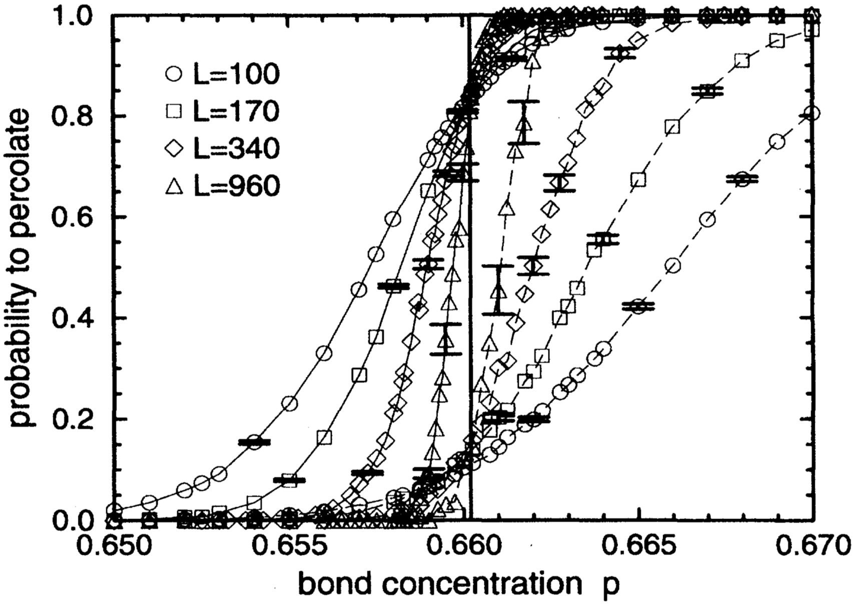

FIGURE 1.6: The probability of having a spanning rigid cluster as a function of occupation probability p is plotted with periodic(dots connected by solid line) or free(dashed line) boundary condition for various system sizes. [14]

In typical phase transition analysis, the above scaling relations and exponents associated with a diverging length scale, suggest a continuous transition. But signs of a discontinuous transition are also found in rigidity percolation, depending on the type of lattice. In addition to finding a discontinuity in the order parameter as a function of p on the honeycomb lattice [16], if **next nearest neighbor**(**NNN**) bonds are added to a square lattice, the system experiences a sharp first-order-like transition in terms of the order parameter at which only one NNN bond can connect many small rigid regions together and form a large rigid bulk structure in the lattice. Our work was, in part, inspired by these findings and demonstrates that even central-force rigidity percolation is so “simple”.

If a phenomenon seems complex, it is sometimes better to think more broadly. In another type of materials called "granular materials", there is a transition similar to the rigidity percolation transition. Can we extract some features from this type of system to help understand the rigidity percolation transition and vice versa? In order to understand similarities and differences between the two phenomena, first we are going to review some of the history of jamming, or the rigidity transition in granular materials (particulate packings).

1.2 Jamming in granular materials

In my childhood, I had an interesting experience. When I was pouring beans into bottles through a funnel, I wished to do it well and fast, but I failed because my beans got clogged if I poured too fast. This could be explained philosophically by "haste brings no success" but was physically a mystery for me. When I was playing near the sea, I liked to put my hand gently on the wet sand and see the sand "swallowing" my hand slowly like a swamp. I enjoyed doing this but, for one moment, I wondered why people can still walk on beach safely. Such questions lingered in my mind until I learned about "granular materials".

1.2.1 Jamming transition

Granular material refers to a system containing a large amount of athermal particles with short-range interactions between neighboring particles, such like foams, non-thermal colloids, or a pile of sand, or a bottle of beans. When driven by external forces, such as compression or shear, the system experiences a transition from fluid-like to solid-like behavior, which is called "jamming", just like beans getting clogged when flowing through a funnel or sand becoming too hard to deform when being compressed heavily. Dating back to 1980s, physicists already made some progress in studying granular materials.

In 1987 Pusey and Megen studied concentrated suspensions in a liquid of solid colloidal spheres with a narrow particle-size distribution [17]. During the experiment, different phases were observed. The system was in a fluid phase at low packing fraction and at glass phase at high packing fraction. **Packing fraction**, usually denoted as ϕ, refers to volume fraction of colloidal spheres in the system space, which is a key characteristic property in granular materials. In their experiment, they fluid-glass transition packing fraction is around 0.56. Even though glass transition was observed in suspensions, by that time the authors were not sure if the glass state was a long-lived metastability or not.

Besides interests in solid granular materials, foams was considered to be a vechile for doing surface treatments in paper coating, fabric finishing and the mobility nature of foams in porous media was useful to oil and gas industry. The study of foam flow under shear stress was motivated by these practical applications. By 1988 [18], **yield stress** was already found that, below such shear stress, the deformation rate of foams is zero and viscosity goes to infinity. Many experiments were conducted and features of data are represented by $\tau_y = \sigma\phi_d^{1/3}F(\phi_d)\bar{R}_b$, where τ_y, σ, $\bar{R}_b$ are yield stress, surface tension, average bubble radius respectively. Also, ϕ_d represents dispersed-phase volume fraction and experimental determined function $F(\phi_d)$ increases by an order when ϕ_d increases in the range between 0.75 and 0.98. This implies volume fraction plays an important role in the mechanical and dynamical features. In 1990, Bolton and Weaire developed code to simulate a disordered, two-dimensional soap froth with volume fraction less than 1 [19]. Their major finding was that the critical value of gas fraction, denoted as ϕ_c, is around 0.84. When the gas fraction approaches this critical fraction from 1, the average contact number decreases from 6 to 4, yield stress and shear modulus vanishes smoothly.

Later in 1995 Durian also numerically studied foam mechanics at the bubble scale [20]. In this simulation, interactions between neighboring bubbles are modeled as center-to-center forces and the foam is sheared in a quasi-static way. As shown in Fig 1.7, above $\phi_c = 0.841 \pm 0.002$, the shear modulus and average contact number are well described by $G \sim (\phi - \phi_c)^\theta$ and $Z - Z_c \sim (\phi - \phi_c)^\theta$, respectively, which are consistent with Bolton and Weaire's arguments. All of these studies pointed to a volume/area fraction as characterizing the transition point between a rigid/jammed state and a floppy/unjammed state. Meanwhile large external loads, for example stress larger than some yield stress, could also "break" the jammed state.

In 1998, Liu and Nagel proposed a landmark phase diagram as shown in Fig1.8 [21]. This diagram ties different systems together and points out that the jamming transition can be found in many types of systems. In the load-free scenario, there is a phase transition between liquid and glass as a function of temperature. In the zero-temperature case, there exists a jamming transition in granular materials. Based on this diagram, jamming can occur only when the packing fraction, or density, is high enough. One

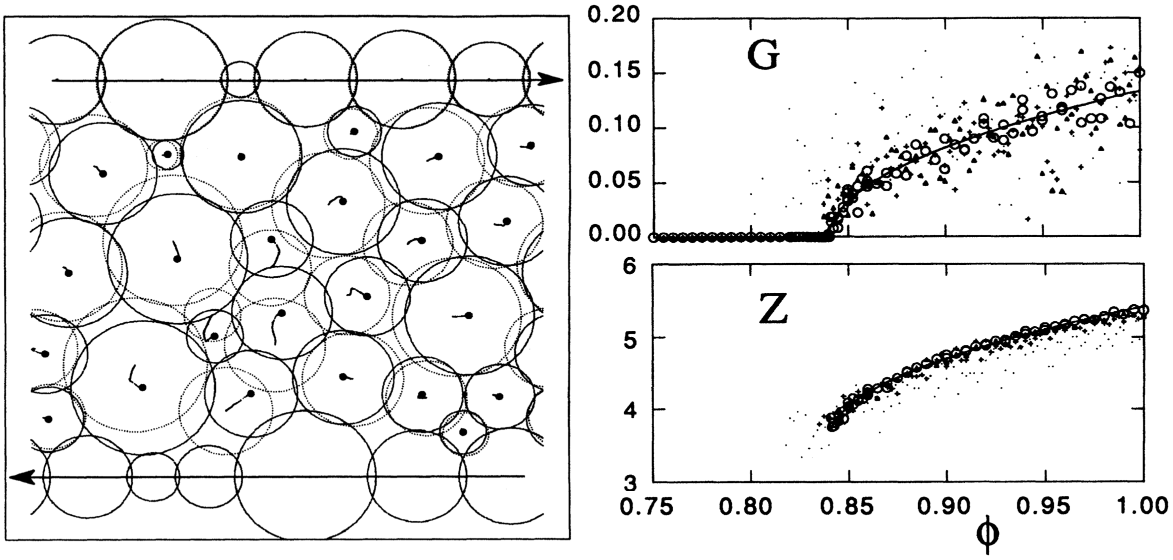

FIGURE 1.7: Left: Durian's schematic of shearing process, arrows represent trajectories of bubble centers. Right: shear modulus G and average contact number Z as function of packing fraction ϕ. [20]

can also unjam a jamming system by raising the temperature or applying more external stress. This paper is titled *Jamming is not just cool anymore*.

1.2.2 A frictionless jamming model

From the jamming phase diagram Fig 1.8, the jamming transition condition in granular materials is controlled by three quantities. For different types of systems, it is hard to compare their behavior near the transition quantitatively. So, in 2003, Corey O'Hern and company numerically studied a system of repulsive soft particles in a region around point J [22], which is shown in the left figure in Fig 1.9 and adapted from Fig 1.8, representing the jamming transition point under zero external stress and

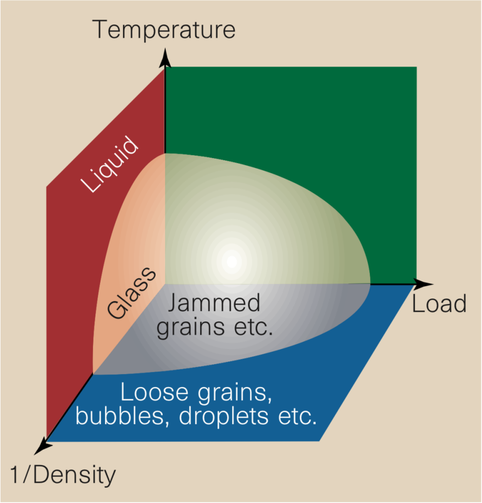

FIGURE 1.8: Phases separation depends on three properties: temperature, density and load. [21]

temperature. They studied the systems' behavior in both two-dimensional and three-dimensional systems made up of particles interacting with finite range, repulsive potentials expressed as:

$$V(r_{ij}) = \begin{cases} \epsilon(1 - r_{ij}/\sigma_{ij})^{\alpha} & r_{ij} < \sigma_{ij} \\ 0 & r_{ij} \geq \sigma_{ij} \end{cases} \tag{1.1}$$

where ϵ is typical scale of energy, r_{ij} is distance between particles i and j and σ_{ij} is the sum of radii of them. Different α represents different types of repulsive potentials. Interactions between the particles are purely central forces, which means there is no friction included. In their simulations, they measurde the static shear modulus G, by applying a very small shear strain, minimizing the energy with the conjugate gradient technique, and measuring the final induced stress. In all cases, no matter if the system was 2D bidisperse, 3D bidisperse, or 3D monodisperse system, $\alpha = 3/2$ or 2 or $5/2$, the fraction of jammed particles raise up to 1 when the packing fraction ϕ approaches 0.58 for a 3D packing and 0.80 for a 2D packing.

This implies that there exists a critical packing fraction ϕ_c which characterize the

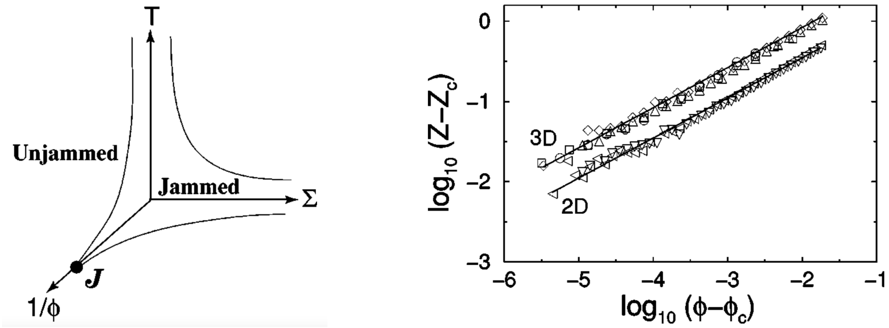

FIGURE 1.9: Left: adapted phase diagram. Right: relation between excess number of contacts per particle and distance to critical packing fraction. [22]

jamming transition while being independent from the type of interactions between particles. At this critical point the system is also an isostatic configuration such that the number of contacts in the system equals to the number of force balance equations: $z_c N/2 = Nd$. Thus, $z_c = 2d$ at the transition point, where d is system dimension. Below transition point z is zero and above transition point within a short range z has a scaling relation to ϕ shown in fig 1.9. $(z - z_c) \sim (\phi - \phi_c)^{\beta}$ can be extracted from the figure, where $\beta = 0.50 \pm 0.03$ for all potentials, dimensions, and polydispersity studied. Another impressive fact about z is that always equals to 0 for $\phi < \phi_c$, which means z experiences a sudden change at transition point. This is due to relaxation of overlapping between particles since there is no friction at all. If one analyzes the rigid clusters in this frictionless packing, in two-dimensions, the onset of the rigid cluster is discontinuous. So while the order parameter behaves discontinuously, there are several diverging correlation lengths, demonstrating that the frictionless jamming transition is a hybrid transition (a mix of continuous and discontinuous elements).

1.2.3 Shear jamming in frictional packings

In the framework described by the phase diagram in Fig 1.8, athermal granular materials experience a jamming transition at a critical packing fraction ϕ_c, which is supported by frictionless simulatons. However, the role of friction in this transition is not readily apparent. Majmudar and Behringer did experiments to look at the jamming transition in frictional granular systems [23]. They studied a 2d bi-disperse system with approximately 3000 polymeric photoelastic disks. In their experiment, they compressed the disks and measured the packing fraction and the pressure. After extracting the contact number, their data fit to the power law relations $(z - z_c) \sim (\phi - \phi_c)^{0.5}$ and $P \sim (\phi - \phi_c)^{1.1}$, where the exponents are in good agreement with the frictionless simulations. But one difference between the frictional system from frictionless system is that the isostatic point z_c is modified. In the frictional case, there are more constraints from friction and ideally z_c becomes 3 instead of 4 for strong friction in two-dimensions. Typically, z_c can be some value in between 3 and 4 (in two-dimensions). Also, ascertaining that system is jammed requires non-zero pressure and stress and the ability to resist any small incremental stress. This jammed state can be clearly identified in the frictionless system due to the sudden change for z from 0 to $z_c = 4$ at ϕ_c. But in the frictional case, the jammed state and unjammed state are not clearly distinguishable.

To further investigate frictional packings, in 2011, Otsuki and Hayakawa studied critical scaling laws near the jamming transition in frictional simulations [24]. Hysteresis was observed in the stress-strain rate curves. They found that scaling laws of pressure, stress and contact number are characterized by two critical packing fractions defined as ϕ_S and ϕ_J. In that same year, Bi and company presented a generalized jamming diagram in the stress-density plane as shown on the right in Fig 1.10 [25]. They discovered a shear jamming state and fragile state in frictional granular materials, which are located out of jamming region in original phase diagram. This shear jamming phase diagram is supported by Otsuki and Hayakawa's numerical results.

Since 2011, there have been many studies to understand how frictional jamming

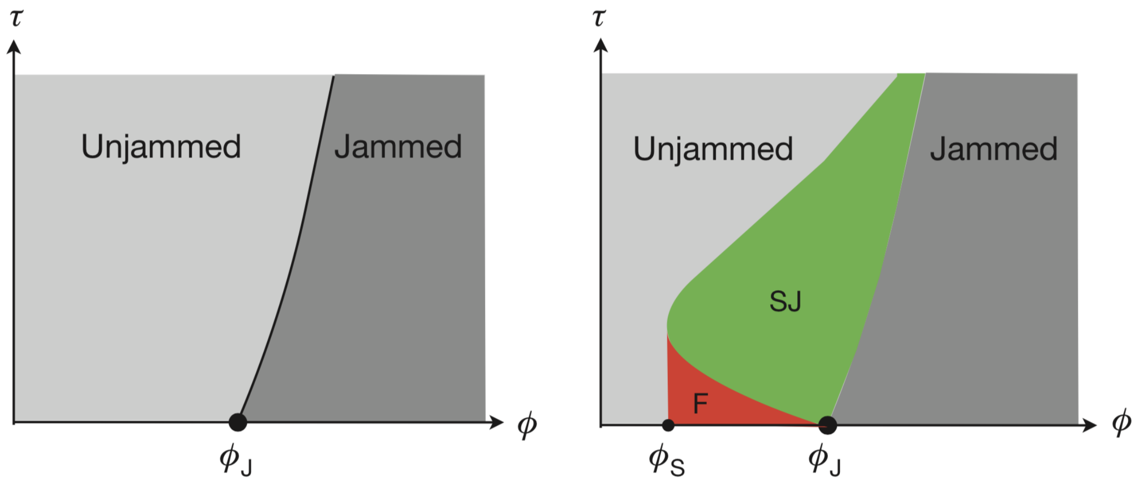

FIGURE 1.10: Original phase diagram and generalized jamming phase diagram with shear jamming. Region labeled SJ represents shear jamming states, F represents fragile states. [25]

extends beyond the traditional jamming phase diagram. In one such study, a rigid cluster decomposition for frictional packings was developed and tested on simulated packings [26]. They utilized concepts from rigidity percolation that I reviewed in first part of this introduction and extended the pebble game algorithm to a frictional (3,3) pebble game to adapt to friction contacts in two-dimensionalfrictional granular packings. Thus they were able to identify rigid clusters in quasi-statically sheared packings. This methodology also allowed them to find microscopic relations between rigid clusters, stresses and nonaffine motion. I will show in Chapter 2 that the frictional (3,3) pebble game connects rigidity percolation and frictional jamming via lattice model and, in Chapter 3 apply these methods to experimental packings for the first time.

1.3 Dynamics in the cell nucleus

And now for the introduction to Act 2 of the thesis.

"How many pairs of chromosomes do you have?" asked my teacher.

"25." I said.

"What's your purpose to come here on Earth?" asked my teacher.

1.3.1 Structure in cell nucleus

A cell nucleus houses its genetic material, or the instructions for building the proteins that a cell needs to function. This material is meter-scale DNA plus proteins to form chromatin and is packaged to fit inside a $\sim$10 μm-scale nucleus. The spatial structure of chromatin, therefore, contains multiple scales as shown in fig 1.11. In a full cell cycle, interphase lasts the longest. Structure and function of the interphase nucleus is studied in experiments or numerical models, where chromatin exists as 30nm-fibers. As shown in Fig 1.12 [27], the nucleus of all eukaryotic cells is bounded by a double phospholipid membrane (purple) composed of an inner and outer leaflet. The nuclear envelope serves as (1) a physical barrier between the chromosomes (blue) and the cell cytoplasm, (2) a structural scaffold for the nucleus, and (3) a permeability barrier between the nucleoplasm and the cytoplasm. It is perforated by nuclear pore complexes (pink) through which small molecules diffuse and larger molecules are selectively transported. In human cells, the inner nuclear membrane is lined by the nuclear lamina (red) to which heterochromatin(dark blue) and specific chromosome domains are anchored, whereas euchromatin (light blue) is enriched in the nuclear interior. Heterochromatin refers to part of chromosome that is densely packed and genetically inactive while euchromatin refers to loosed packed and genetically active part.

To dig into the microscopic spatial structure of chromatin, in 2009 Lieberman-Aiden and company invented Hi-C [29], a method that probes the three-dimensional architecture of whole genomes by coupling proximity-based ligation with massively parallel sequencing. From the map constructed from the Hi-C method, they confirmed the presence of chromosome territories, which is consistent with spatial structure of

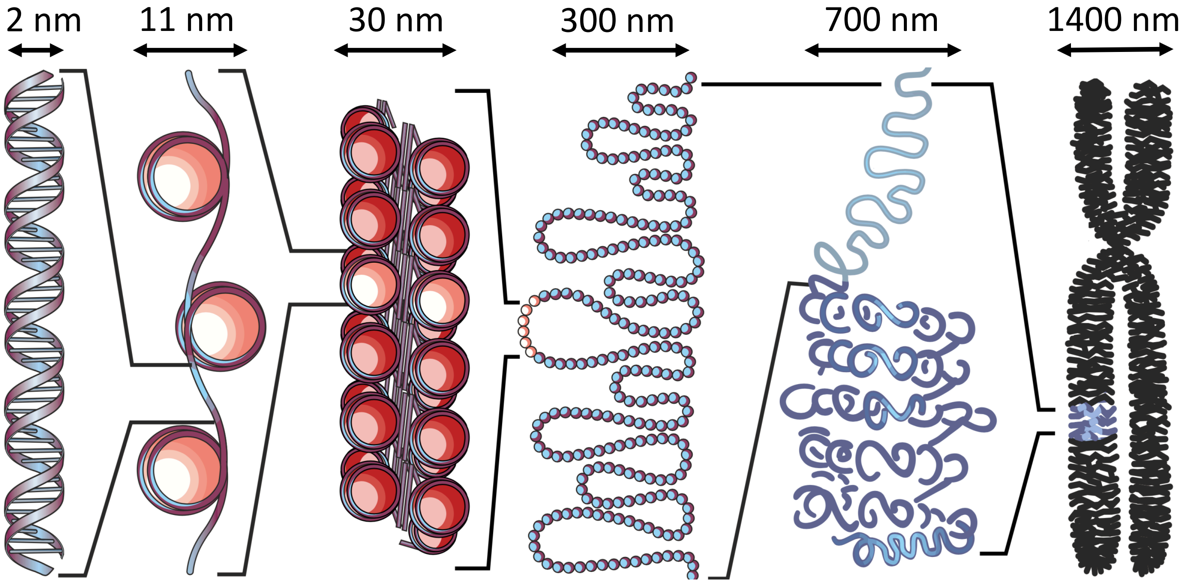

FIGURE 1.11: Different scales of DNA packaging in the cell nucleus. [28]

a fractal globule, a polymer model of chromatin that had been predicted years earlier [30, 31]. the Fractal globule is a knot-free polymer conformation that enables maximally dense packing while preserving the ability to easily fold and unfold any genomic loci. In a fractal globule, the radius of gyration R_s of a subchain with length s is scaled as $R_s \sim s^{1/3}$ while this relation in common-used globular equilibrium globule is $R_s \sim s^{1/2}$ [32].

1.3.2 Modeling correlated motion

Not only does the spatial structure of chromatin matter for cell nucleus functionality, chromatin is also moving inside the nucleus and such motion could cause rearrangement of nuclear structure to potentially affect gene expression. The obvious example is the transcriptional motor RNA polymerase II that walks along DNA. The unwinding of DNA around histones is needed for transcription and so while there is dynamics/motion of the DNA at the nanometer scale, is there larger scale motion? Nontrivial,

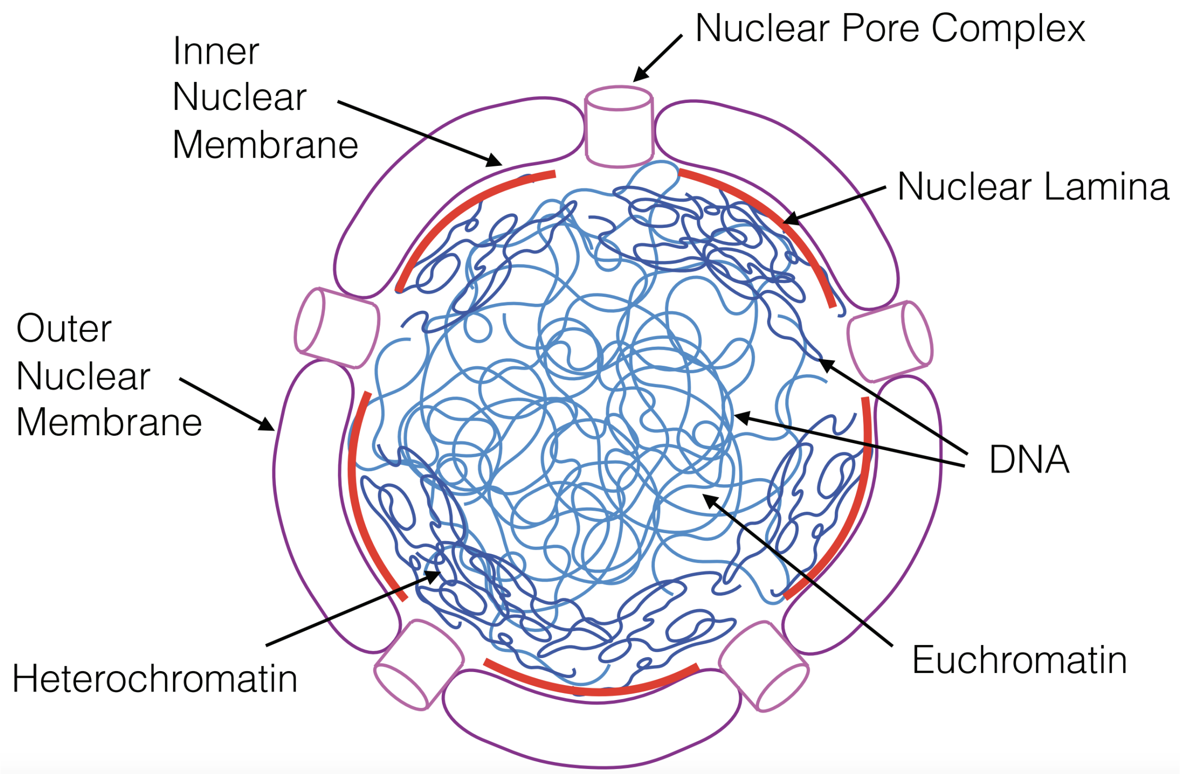

FIGURE 1.12: Schematic of a human cell nucleus. [27]

larger scale chromatin motion indeed occurs. To be specific, correlated motion of genomic regions on the length scale of microns over the time scale of tens of seconds has been observed [33]. In 2013, Zidovska, Weitz and Mitchison analyzed time-resolved images of the nucleus and calculated the displacement correlation function [33]. This function can be described by $Cr(\Delta r) = A(\Delta r)^n e^{-\Delta r/\xi}$, where Cr, ξ are correlation and correlation length respectively. They found that such correlated motion spans across around 4-5 microns for several seconds and is diminished under perturbation of ATPases, such as DNA polymerase, RNA polymerase II, and topoisomerase II. This implies that motor proteins consuming ATP are playing a role in the correlated motion of chromatin.

The Rouse model is a simplest theory of polymer dynamics and it explains well the dynamical properties of polymer in the absence of hydrodynamics and entanglements [34]. It is simply a string of beads connected by springs. Since the 30 nm chromatin fibers are polymer chains at a length scale larger than 30 nm, and there motors acting on them, Osmanovic and Rabin modeled active forces as non-thermal random forces on the Rouse chain [35]. They analytically found that random-direction active forces on the Rouse chain induce an effective additional temperature. They also found that the polymer is self-correlated over some timescale. They did not consider confinement in their calculations. There are other polymer models of chromatin under confinement. In 2018, Saintillan, Shelley and Zidovska constructed a polymer model of chromatin [36] including active force dipoles (one applied on polymer and the other on liquid background), hydrodynamics, and fixed spherical boundary conditions. In their model they obtained strong correlated motion for extensile activity (force dipole back to back) and but not in the contractile active case (force dipole face to face) and passive case (force dipole turned off). Clearly, hydrodynamics introduces long-range correlations between different regions of the chromatin

In addition to activity and confinement, there are two additional features of chromatin that the 2018 chromatin model neglected: chromatin crosslinks and linkages between chromatin and the lamina. Motor cluster complexes may provide a mechanism for cross linking chromatin as indicated by inhibition of active RNAPII leading to larger mean-squared displacements of nucleosomes, shown in Fig 1.13. Chromatin binding proteins, such as heterochromatin protein 1 (HP1), also function as chromatin crosslinkers[37]. Rheological studies found that chromatin crosslinks were required in a computational model to replicate the force extension curves of isolated, stretched nuclei [38]. Chromatin motors and binding proteins, thus, may remodel as well as crosslink, to arrive at a more collective picture of chromatin. Moreover, the cell nucleus contains 10-30-nanometer thick [39, 40] filamentous network of intermediate filaments, known as lamins, between the chromatin and the inner nuclear membrane. Interactions between the chromatin and lamin, such as lamin-associated domains along chromatin, provide linkages of the chromatin to the filamentous, lamina shell.

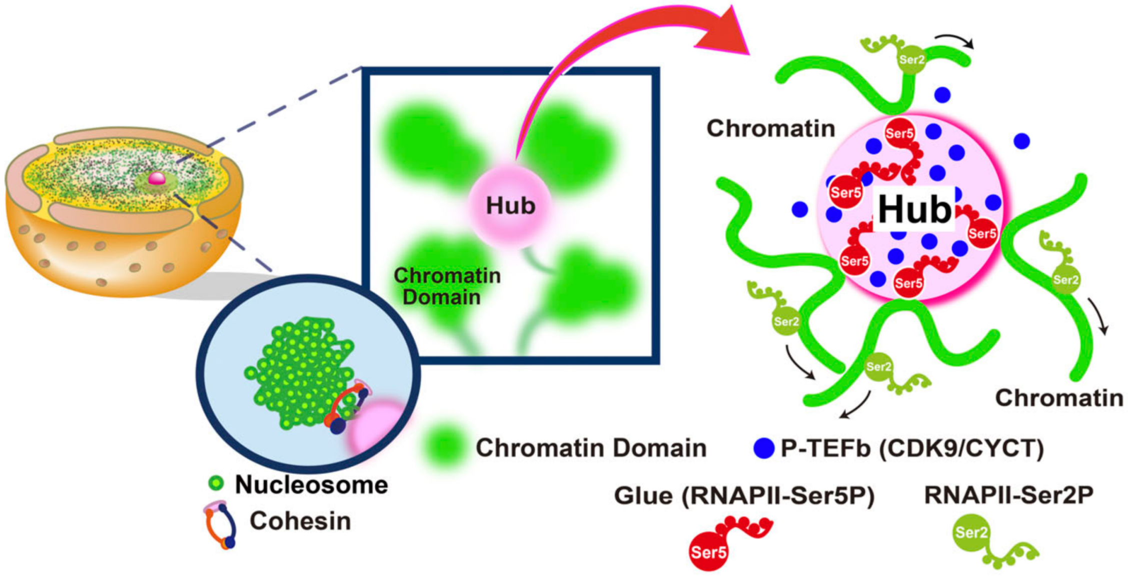

FIGURE 1.13: A model for the formation of a loose spatial genome chromatin network via RNAPII-Ser5P, which can globally constrain chromatin dynamics. [41]

Based on these, and earlier, developments, in Chapter 4 to understand how the correlated chromatin dynamics emerges and how nuclear shape is affected, I am going to construct a model with motor activity for the composite chromatin-lamin system, with the chromatin modeled as an active Rouse chain with excluded volume interactions and the lamina as an elastic, polymeric shell with bindings between the chain and the shell. I will also include chromatin crosslinks and linkages between the chromatin and the lamina.

1.4 Outline

In this thesis of two acts, first I will address a problem that seems to emerge in two classes of systems in different ways in Chapters 2 and 3. A rigidity transition occurs in central-force networks and a shear jamming transition occurs in granular packings. Typically, the former is characterized by scaling exponents near the transition, such as correlation length exponent ν and the order parameter exponent β, while the latter is studied by evaluating the evolution of force chains or particle flows. My goal is to unify these two transition by looking at their macroscopic behaviors and localized motifs.

Specifically, in Chapter 2 I encode typical mechanical constraints in frictional particle packings into a lattice network. Within this framework, I study the frictional rigidity percolation to identify the nature of the frictional jamming transition as well as significantly broaden the scope of rigidity percolation. I construct rigid clusters using a frictional (3,3) pebble game algorithm on a honeycomb lattice with next-nearest neighbors, and second on a hierarchical lattice. For both lattices, I find a continuous rigidity transition. The numerically-obtained transition exponents for frictional rigidity percolation on the honeycomb lattice are distinct from those of central-force rigidity percolation. Some localized motifs are proposed and could give rise to this new frictional universality class. And yet, the distinction between the exponents characterizing the spanning rigid cluster for frictional and central-force rigidity percolation is small, motivating me to search for mechanisms of superuniversality. I construct a minimally rigid cluster generating algorithm invoking generalized Henneberg moves, dubbed minimal rigidity proliferation. For both frictional and central-force rigidity percolation, these clusters appear to be in the same universality class as connectivity percolation, suggesting superuniversality between all three transitions for such minimally rigid clusters. These combined results allows me to directly compare two universality classes on the same lattice and to highlight unifying and distinguishing concepts of rigidity transitions in disordered systems.

In the third chapter, I show how rigidity emerges in experiments of sheared frictional granular materials by using generalizations of two methods for identifying rigid structures. Both approaches, the force-based dynamical matrix and the connectivity-based rigidity percolation, agree with each other and identify similar rigid structures. As the system becomes jammed, a rigid backbone interspersed with floppy, particle-filled holes of a broad range of sizes emerges, creating a sponge-like morphology. I also found that the pressure within rigid structures always exceeds the pressure outside the rigid structures. These findings shows that it is necessary to look at emergence of localized backbones to capture the physics of frictional jamming and also suggests that mechanical stability arises through arch structures and hinges at the mesoscale.

The second part of this thesis, presented in Chapter 4, addresses chromatin dynamics. Chromatin dynamics is believed to be very important in that it causes rearrangements of the locus of genome. The pattern of chromatin dynamics is highly nontrivial since spatial-temporal correlated motion was found between different chromosome regions. Hydrodynamics is usually included in chromatin models exhibiting correlated motion. Yet, chromosomes are linked to a protein shell called the lamina and protein motors and chromatin binding proteins in the nucleus drive nuclear shape fluctuations. In Chapter 4, a minimalistic chromatin-lamina model is developed in which an active, crosslinked Rouse chain is locally linked to a polymeric shell. System-sized correlated motions occur require both motor activity and crosslinks. Contractile motors in particular enhance chromosome dynamics by driving anomalous density fluctuations. Nuclear shape fluctuations depend on motor strength, crosslinking, and chromosome-lamina binding. Complex chromatin dynamics and nuclear shape, therefore, both emerge from this minimal, composite chromosome-lamina system.

Finally in Chapter 5, I will summarize the various results presented. To conclude, I will end with a discussion of future directions and implications of rigidity in particulate system and dynamics in polymeric system.

Chapter 2

Frictional rigidity percolation in lattice model

This chapter is based on work primarily presented in the article "Frictional rigidity percolation: A new universality class and its superuniversal connections through minimal rigidity proliferation" co-authored by Silke Henkes and J. M. Schwarz and published in the journal Physical Review X in the year 2019. We came up with the model together and I was responsible for doing most of the numerical work. The paper itself was primarily written by J. M. Schwarz. Silke Henkes and I also contributed to some editing.

2.1 Rigidity transition and jamming transition

At the heart of every rigidity transition is the emergence of a spanning rigid cluster–an entity of interconnected bonds that are rigid with respect to each other. For disordered systems, the starting point of choice has become randomly-diluted spring networks with central-force interactions [6, 7, 42, 43]. As bonds are randomly diluted from a triangular lattice, either a regular one or with slightly randomized lattice points (a generic lattice), the system goes from rigid with a non-zero shear modulus to floppy without this feature [44, 13, 14, 15]. Underlying this mechanical phase change is the transition from a system with a spanning rigid cluster to a system without one, as identified by the combinatorial (2,3) pebble game [45]. The location of this rigidity transition occurs approximately at isostaticity where the number of degrees of freedom are frozen out by the number of force-balance equation constraints, known as Maxwell constraint counting [10].

The rigidity transition in the central-force, randomly bond-diluted triangular lattice was numerically found to be a continuous one with a correlation length exponent, $\nu = 1.21 \pm 0.06$, an order parameter exponent $\beta = 0.18 \pm 0.02$, and a fractal dimension of the spanning rigid cluster, $d_f = 1.86 \pm 0.02$ [13, 14]. These exponents differ slightly from two-dimensional connectivity percolation where $\nu = 4/3$, $\beta = 5/36$, and $d_f = 91/48$ [46]. Despite the small difference in exponents, it was eventually argued that central force rigidity percolation (RP) is in a separate universality class since there are nonlocal effects in terms of how rigid clusters grow that differ from connectivity percolation [13, 14]. Meanwhile, Bethe lattices with no loops are amenable to analytical treatment and demonstrate that the spanning rigid cluster at the transition is not fractal [47, 48]. To add to the complexity, numerical simulations of three-dimensional lattices with central-force interactions indicate a discontinuous rigidity transition as well, in contrast to the two-dimensional case [49]. Finally, central-force models with next-neighbor springs can exhibit hybrid rigidity transitions with both continuous and discontinuous features [16]. With this rather varied set of phase transitions when changing just the type of lattice, the general solution to the central-force RP problem is far from clear, if it is even possible.

Rigidity percolation with bond-bending forces adds another “dimension” to the problem [50, 51, 52, 52, 53, 54]. Numerical simulations of two-dimensional systems measuring elastic properties suggest that bond-bending forces drive the transition into a different universality class [55]. However, since there is currently no pebble game

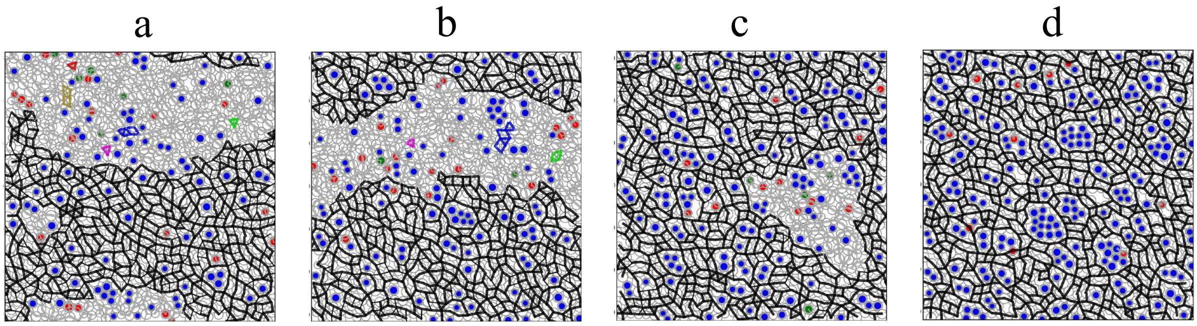

FIGURE 2.1: *Rigid clusters in simulated frictional packings under slow shear.* Four snapshots from the molecular dynamics simulation showing partially rigid systems close to the frictional rigidity transition. In black is the largest rigid cluster, while floppy regions are colored gray. Blue, green and red disks correspond to three, two and one leftover pebble, respectively. The range of partial rigidity decreases with increasing friction coefficient μ, or equivalently, increasing q. (a) $\mu = 0.2$, with a transition at $q = 0.78$ and average coordination number $z = 3.35$. (b) $\mu = 0.3$, with a transition at $q = 0.86$ and $z = 3.15$, (c) $\mu = 0.5$, with a transition at $q = 0.95$ and $z = 3.0$, and finally (d) $\mu = 10$ with a transition at $q = 1.0$ and $z = 2.8$. The last value is due to the large number of contactless particles (rattlers) in the packing, visible in blue.

for bond-bending forces even in two-dimensions, a direct comparison to central-force rigidity percolation in terms of ν, β, and d_f has yet to be made.

Particle packings also undergo a rigidity transition as a function of the packing fraction [20, 22, 56] and additionally feature contact network rearrangements, unlike the randomly-diluted spring networks. The rigidity transition in such systems has been labeled the *jamming transition*, where the system moves from a zero to non-zero bulk and shear modulus with increasing packing fraction, suggesting the emergence of a spanning rigid cluster [22]. This suggestion was made explicit by first extracting the contact network of a two-dimensional *frictionless* (i.e. central forces only) particle packing at jamming. Second, constructing the rigid clusters from this network via the (2,3) pebble game shows that at the onset of rigidity/jamming every particle participating in the contact network is part of one rigid cluster, i.e. the spanning rigid cluster is bulky at the transition [57].

In *frictional* particle packings, jamming is even less understood. Recently two of us [26] developed a new pebble game algorithm incorporating both particle translations and rotations to compute rigid clusters for networks abstracted from two-dimensional frictional particle packings. We applied it to molecular dynamics simulations of frictional particle packings at a fixed packing fraction experiencing slow shear, and determined rigid clusters at constant strain intervals as the packing repeatedly goes through jamming/unjamming. The size of the largest rigid cluster indicates a continuous transition, and so does the observation of a roughly power-law distribution of rigid cluster sizes near the jamming transition [26]. Within the spanning rigid clusters, we found regions of floppiness, showing partial rigidity. The floppy regions are also physically relevant as the non-affine motion of the particles is smaller inside the rigid cluster compared to outside, and the pressure is higher. We present four such rigid cluster images close to the transition for four different values of the friction coefficient μ in Fig. 2.1. The major open question arising from this recent study of frictional rigid clusters is whether or not the rigidity transition is actually continuous or not, as a continuous rigidity transition would be very different from the frictionless case. Unfortunately, the molecular dynamics simulation could not tune the system to be arbitrarily close to the rigidity transition, and so it remains difficult to assess the nature of the transition using such simulations.

Here, we ascertain the nature of the rigidity transition in frictional systems with the introduction of *frictional RP*, that is the study of rigid clusters constructed via the frictional (3,3) pebble game, on randomly-diluted lattices with bonds denoted either as frictional or sliding. We study two types of lattices: the honeycomb lattice with next-nearest neighbors and a hierarchical lattice. The former can be studied numerically, while the latter is amenable to analytical calculations. The results for both lattices can then be compared to results for central-force RP to arrive at the first direct comparison *ever* between different types of forces on the same lattice. In generalizing rigidity percolation, we can now take a step back to look a broader set of problems to be more readily able to identify special cases in a forest of rather eclectic trees.

The structure of the rest of chapter one is as follows. We first describe frictional rigidity percolation on the honeycomb lattice with next-nearest neighbors and present our results. We then describe frictional rigidity percolation on a hierarchical lattice and discuss how our analytical calculations can help bolster the numerical results on the honeycomb lattice. Moving on, we present minimal rigidity proliferation and argue how its strategic bond occupation method is different enough from our earlier random bond occupation to lead to superuniversality amongst the different models. We then conclude with a discussion of the implications of our results. A graphical abstract is provided in Fig. 2.2 and serves as a roadmap for the manuscript.

2.2 Lattice models

2.2.1 Honeycomb lattice with next-nearest neighbors

Model

To motivate the model we begin with by reviewing Maxwell constraint counting in two-dimensional frictionless packings (or central-force spring networks) with N particles (vertices) and average coordination number z [10]. The total number of degrees of freedom is $2N$, while there are $\frac{Nz}{2}$ force-balance constraints. When the number of degrees of freedom is equal to the number of force-balance constraints, the system is minimally rigid, i.e.

$$2N - 3 = \frac{z_c N}{2}, \tag{2.1}$$

where the number of global rigid body translations and rotations has been subtracted out since they are trivial. This equation yields the critical average coordination number $z_c = 4$ (as $N \to \infty$) for the onset of rigidity. Much numerical work with frictionless particle packings has shown that this counting is an extremely good method to determine the rigidity transition point [58, 59, 60]. No states of self-stress are observed in particle packings at the transition, since the values of the purely repulsive forces are uniquely determined by the boundary conditions at this point, such that a more involved constraint counting approach is not needed [11].

For two-dimensional frictional particle packings, some contacts are below the Coulomb threshold with the magnitude of the tangential force less than the magnitude of the repulsive, central force times the friction coefficient. At such contacts, two particles can only rotate and translate with respect to one another just as a gear does, and these are denoted as frictional contacts. There are also contacts at the Coulomb threshold in which two particles slide with respect to each other. For these sliding contacts, the magnitude of the tangential force is set by the magnitude of the repulsive, central force, i.e. there is only one constraint. We distinquish between these two types of contacts by denoting q to be the probability of having a frictional contact with $1-q$ denoting the probability of having a sliding contact, i.e. if $q = 1$, all contacts are frictional. Then, performing the Maxwell constraint counting as above, since each particle has 3 translational and rotational degrees of freedom, there are $3(N-1)$ total degrees of freedom (subtracting out the trivial global degrees of freedom in which there is no relative motion between the particles). Moreover, the interparticle forces yield $\frac{z(1+q)N}{2}$ total constraints. We, therefore, arrive at the minimal rigidity criterion, or

$$3N - 3 = \frac{(1+q)z_c N}{2}, \tag{2.2}$$

where q denotes the probability of having a frictional bond. For $N \to \infty$ and $q = 1$, all bonds are frictional and $z_c = 3$. If $q = 1/2$, we have $z_c = 4$. Therefore, Eq. 2.2 describes a *line* of transition points interpolating from $z_c = 3$ to $z_c = 4$ as the ratio of frictional to sliding bonds changes. This method of counting is now known as generalized isostaticity [61, 62]. Such bounds are indeed observed in experiments [63]. Note that increasing the friction coefficient μ increases q, and in addition, that one cannot smoothly interpolate between frictional and frictionless packings as one cannot smoothly interpolate between 2 and 3 local degrees of freedom.

To construct a lattice model for frictional particle packings, we consider a honeycomb lattice with additional next-nearest neighbor (NNN) bonds. This modified honeycomb lattice has a maximum coordination number of $z_{max} = 9$. We define p as the probability of bond/contact occupation. The reason we employ the honeycomb lattice with next-nearest neighbors is because we can explore geometry to determine whether or not it is relevant for determining the nature of the phase transition. We do so by constructing and studying two different models for bond occupation, see Figure 2.3. For the first model, we fully occupy the honeycomb backbone such that $p = 1/3$ and then occupy the additional NNN bonds occupied randomly such that $p \geq 1/3$. We dub this first strategy of bond occupation $HC1$. We also implement a second strategy of bond occupation in which the bonds, both nearest-neighbor or next-nearest-neighbor, are occupied at random, which we dub $HC2$. For $HC1$, since the honeycomb backbone is fully occupied, the central forces on each particle can be balanced, which is required by local mechanical stability in frictionless, but not frictional, packings. Therefore, $HC1$ will allow us to more readily compare with the geometry of frictionless packings in order to see how frictionless differs from frictional. The frictional bonds are then randomly assigned with probability q, and periodic boundary conditions are implemented.

Now we address the frictional versus sliding bonds for this lattice model. Since frictional bonds randomly occur with probability q, using Eq. 2.2 the critical occupation probability predicted by Maxell constraint counting is

$$p_c = \frac{z_c}{z_{max}} = \frac{2}{3(1+q)}. \tag{2.3}$$

Equation 2.3 tells us how p_c depends on q, therefore, denoting a phase transition line between floppy and rigid phases just as in generalized isostaticity.

Once the frictional and sliding bonds have been identified, we construct a constraint network in which frictional bonds below the Coulomb criterion are denoted as double bonds in the constraint network and sliding bonds at the Coulomb threshold are denoted as single bonds in the constraint network. We then play the $(3,3)$ pebble game on this constraint network in which the first number denotes the number of local degrees of freedom and the second number denotes the number of trivial global degrees of freedom, which does depend on boundary conditions. However, Ref. [26] found that changing the number of trivial global degrees of freedom from 3 to 2 due to periodic boundary conditions did not significantly affect the rigid cluster analysis for both frictional and frictionless particles and so we stick with the $(3,3)$ and $(2,3)$ pebble games.

We illustrate the $(3,3)$ pebble game algorithm using several very simple constraint networks in Fig. 2.4. A more detailed explanation can be found in Appendix 2.4. Examples or the rigid clusters we find below, at, and above the rigidity transition for both HC1 and HC2 are shown in Figure 2.5. To compare frictional RP with central force RP, we complement our analysis with an approach where any double bond is converted to a single bond and a (2,3) pebble game is played since each site contains now only two degrees of freedom. Examples of the corresponding rigid clusters are shown in Figure 2.6. Finally, we implement finite-size scaling analysis to quantify the transition for $HC1$ and $HC2$ for different qs for the frictional $(3,3)$ pebble game and for the central-force $(2, 3)$ pebble game.

Results

Spanning probability: We first identify the location of the rigidity transition by determining whether or not there exists at least one spanning rigid cluster in the x or y direction as both p and q are varied. We do this for all four variants, $HC1$ and $HC2$ for both the frictional $(3, 3)$ game and the frictionless $(2, 3)$ game. For $HC2$ we study $q = 0.5$ and $q = 1.0$, the two extreme values of q. For $q = 1$, isostaticity predicts $p_c(1) = \frac{1}{3}$. For the $HC1$ model, this is identical to the initial occupation of the honeycomb lattice backbone, and for this regular lattice, we expect one spanning rigid cluster with a unity probability of spanning, i.e. a first-order transition. Therefore, for $HC1$, we study $q = 0.5$ and $q = 0.7$ and do not explore the limit $q \to 1$ since $q = 1$ is a special case.

Figure 2.7 plots the probability that the system contains at least one spanning rigid cluster as a function of p for different system lengths L. Figure 7a presents data for $HC1$ with $q = 0.5$, while Figure 7b presents data for $HC1$ with $q = 0.7$. In both subfigures, different curves with different system sizes cross near a particular value of p, which indicates the location of the transition point denoted hereafter as $p_c(q)$. In particular, $p_c(0.5) \approx 0.447(1)$ and $p_c(0.7) \approx 0.396(1)$. These two critical points are very close to the results from the generalized isostaticity counting in Equation 2.3 with $p_c(0.5) = \frac{4}{9} \approx 0.444$ and $p_c(0.7) = \frac{20}{51} \approx 0.392$.

The probability of spanning for $HC1$ at $p_c(q)$ for both $q = 0.5$ and for $q = 0.7$, is approximately 0.6. Since this value is significantly less than unity, our findings suggest a continuous transition for the onset of the spanning rigid cluster. Typically, the value of probability of spanning at the transition is not a universal quantity and depends on details of the model. For the frictionless version of $HC1$, shown in Figure 7c, the crossing point is more difficult to determine but we estimate it to be near $0.448(1)$.

For the $HC2$ version of the model (bottom row of Fig. 2.7), we again find crossing points near the predicted generalized isostaticity counting since the formula also applies to this variant of the bond occupation. Since there is no ordered honeycomb backbone that is initially occupied, we explore both the lower and upper bounds of q, i.e. $q = 0.5$ and $q = 1.0$ (Figures 7d and 7e). Our results can be found in the first column of the Table in Figure 2.9. We note that there is greater discrepancy of the estimated p_c from generalized isostaticity for $HC2$ than for $HC1$. We also note that the probability of spanning at the transition (the crossing point) now differs between $q = 0.5$ and $q = 1.0$, which does not imply a different universality class because the crossing point depends on details of the lattice. The frictionless version of $HC2$ is plotted in Figure 7f.

Correlation length: The correlation length ξ quantifies how two distant particles/sites interact. In a continuous transition, the correlation length diverges at the transition, while near the critical point, $\xi \sim |p - p_c(q)|^{-\nu}$ on either side of the transition, where ν is the correlation length exponent. In a finite-size system and near the transition, ξ is replaced by the system length L. For each realization, after this replacement, the system has a finite-size critical point $p_c^L(q)$ when the system contains a spanning rigid cluster, with $|p_c^L(q) - p_c^\infty(q)| \propto L^{-\frac{1}{\nu}}$. Since the location of the transition fluctuates for each realization, we therefore obtain a distribution of finite-size critical points as observed in Figure 2.7. The standard deviation of this distribution, Δ, yields a measurement of the correlation length exponent [4]. More precisely,

$$\Delta(L) = \sqrt{\overline{p_c^L(q)^2} - \overline{p_c^L(q)}^2} \sim L^{-1/\nu}. \tag{2.4}$$

Using error function fits to the data in Figure 2.7, we numerically differentiate the curves and fit to Gaussians to compute $\Delta(L)$ and extract the correlation length exponents $\nu = 1.58 \pm 0.13$ for $HC1$ with $q = 0.5$ and $\nu = 1.48 \pm 0.20$ for $q = 0.7$. Both values are within one standard deviation of each other. For the frictionless version of $HC1$, we obtain $\nu = 1.50 \pm 0.07$. For $HC2$, we find $\nu = 1.48 \pm 0.05$ for $q = 0.5$, $\nu = 1.43 \pm 0.04$ for $q = 1.0$, and $\nu = 1.33 \pm 0.05$ for the frictionless version. Figure 2.8e shows the width of the transition for the six different variations of the honeycomb lattice model.

Spanning rigid cluster: We now study the properties of the spanning rigid cluster using P_∞, the fraction of occupied bonds in the spanning rigid cluster. Fig. 2.8a shows P_∞ for increasing p for different system lengths for $HC1$ with $q = 0.5$. We note that P_∞ at $p_c(0.5)$ decreases as the system size increases, which, again, suggests that rigidity transition here is continuous. The behavior of this curve just above the critical point $p_c(q)$ is described by the order parameter exponent β with $P_\infty \sim (p - p_c(q))^\beta$ for $p \geq p_c(q)$, for an infinite size system. As long as $L >> \xi$, the equation applies and $P_\infty \sim \xi^{-\frac{\beta}{\nu}}$. However, when $L << \xi$, the length scale will be set by L such that $P_\infty \sim L^{-\frac{\beta}{\nu}}$. We therefore introduce a universal scaling function $f(\frac{L}{\xi})$ that interpolates between these two regimes, or

$$\begin{aligned} P_\infty(p, L, \xi) &= (p - p_c(q))^\beta f(\frac{L}{\xi}) \\ &= (p - p_c(q))^\beta f(L(p - p_c(q))^\nu) \\ &= L^{-\frac{\beta}{\nu}} \tilde{f}(L^{1/\nu}(p - p_c(q))), \end{aligned} \tag{2.5}$$

with $f(\frac{L}{\xi}) = (\frac{L}{\xi})^{-\frac{\beta}{\nu}}$ for $L << \xi$ and a constant for $L >> \xi$. The universal scaling function $\tilde{f}(\frac{L}{\xi})$ can be obtained by rescaling

$$P_\infty L^{\frac{\beta}{\nu}} = \tilde{f}((p - p_c(q))L^{1/\nu}) \tag{2.6}$$

as is done in Fig. 2.8b for $q = 0.5$, with $\nu = 1.56$ and $\beta = 0.18$ used as fitting parameters to obtain the optimal collapse. This estimate for ν is consistent with our previous measurement for the same q from $\Delta(L)$ in Fig. 2.8e. The collapse supports the notion of a continuous rigidity transition. We implement the same protocol for the remaining cases to look for a continuous rigidity transition.

With the exception of the frictionless version of $HC1$, shown in Fig. 2.8c-d, the order parameter exponent does not vary too much between the different models, as summarised in Fig. 2.9c, though given the smallness of β, it is more difficult to measure as precisely as ν. The small value of $\beta \approx 0.07$ for the frictionless version of $HC1$ perhaps suggests that this model is similar to the square and kagome lattices with next-nearest neighbors studied in Ref. [16]. There, a hybrid transition was found, where the onset of the spanning cluster was discontinuous, but with a diverging correlation length, though the correlation length exponent appeared to be unity.

In addition to the order parameter exponent, one can also measure the fractal dimension of the spanning cluster to determine whether or not it is, indeed, fractal. To test for this possibility, the fractal dimension is determined by measuring the number of bonds in the spanning rigid cluster, M, as a function of system length such that $M \sim L^{d_f}$. In Figure 2.8f, we see that when $q = 0.5$, $d_f = 1.81 \pm 0.06$. For $q = 0.7$, $d_f = 1.80 \pm 0.05$, so we observe little change in the fractal dimension with q, at least for these system sizes, provided q is not close to unity. Similar fractal dimensions were found for both the frictional and frictionless versions of the $HC2$ version of the model and are listed in the table in Figure 9c.

Non spanning rigid clusters: In connectivity percolation, one typically investigates the non spanning cluster size distribution, defined as the number of finite clusters of size s per lattice site/bond, or n_s [4]. At the transition, $n_s \sim s^{-\tau}$, where τ is the cluster size exponent. For connectivity percolation, we hav the inequality $\tau > 2$ strictly. How can we understand this result? We start with $\sum_{s=1}^{\infty} sn_s(p) + P_\infty(p) = p$. Since $P_\infty(p_c) = 0$ for connectivity percolation, then $\sum_{s=1}^{\infty} sn_s(p_c) = p_c$ at the transition. Using the assumption that $n_s \sim s^{-\tau}$ and converting the sum to an integral, $\tau > 2$ for convergence to a finite value, i.e. p_c.

In rigidity percolation, the situation is more complex because there are non-spanning rigid clusters, spanning rigid cluster(s), *and* floppy regions. If both the non spanning rigid cluster size distribution and the floppy cluster size distribution are power laws independently at the transition, each exponent associated with the respective size distribution should be greater than 2. On the other hand, if one of the exponents is less than 2, that would suggest a natural cutoff for that type of cluster and the more tenuous structure could still facilitate a continuous transition. If both exponents are less than 2, then perhaps this aspect of the transition is discontinuous.

As detailed below, we cannot rely on hyperscaling relations for RP. Therefore, we keep track of the non spanning rigid clusters only and posit that their size distribution also behaves as a power law at the transition with exponent τ. If $\tau < 2$, then there is presumably a characteristic cutoff for the non spanning rigid cluster sizes at large enough sizes with coupling to the floppy regions perhaps driving the continuity of the transition. Figure 2.9a shows the probability for having a nonspannning rigid cluster of size s as p is increased through the transition point for $HC1$ with $q = 0.5$ on a log-log scale. Below the transition point, there are many small rigid clusters in the system. As p increases, they merge into larger ones and the distribution broadens to approach a linear function on a log-log scale; the downward trend of the tail is due to finite size effects. We obtain $\tau = 1.90 \pm 0.03 < 2$ from a linear fit to the relevant part of the curve. Above $p_c(q)$, the spanning rigid cluster “swallows” the non spanning rigid clusters and ultimately, as p is increased far beyond the transition point, there is only one spanning rigid cluster left. We have measured τ for the six different cases and find a persistent difference between the frictional and frictionless case in that $\tau > 2$ for the frictionless cases, while $\tau < 2$ for all frictional versions (see Figs. 2.9b and c) indicative of rather different ways the rigid clusters merge and grow in the two cases.

Rigid Cluster Merging Mechanisms

The results of our finite-size scaling analysis are summarized in the Table in Fig. 2.9. We also include the exponents for central-force rigidity percolation using the (2,3) pebble game on the triangular lattice (denoted as TL) and for connectivity percolation (denoted as CP) on the triangular lattice for comparison. For the frictional versions implementing the (3,3) pebble game, we find that $HC1$ and $HC2$ appear to be in the same universality class, with the exception of the special case of $HC1$ at $q = 1$ in which a discontinuous transition emerges as discussed earlier in Sec. II. We also conclude that exponents associated with $HC2$ and the (2,3) pebble game are in the same universality class as the exponents for central-force rigidity percolation on the triangular lattice obtained about twenty years ago. On the other hand, we find that the exponents associated with $HC1$ and the (2,3) pebble game are potentially more related to the square lattice plus braces (i.e., next-nearest neighbors) in which a hybrid transition was found [16], so that this case is special, just as $HC1$ with $q = 1$ is special.

So while our (2,3) pebble game results are consistent with prior central-force rigidity percolation results, our new frictional rigidity percolation compel us to ask the question what mechanism(s) could drive frictional rigidity percolation and central-force rigidity percolation to be in distinct universality classes? To begin to answer this question, we ask the following question: How do two rigid clusters combine to form one larger rigid cluster?

Unlike in connectivity percolation, in rigidity percolation two independently rigid clusters cannot become one rigid cluster by joining via a single bond. For a frictional rigidity percolation example with $q = 1$, consider two triangles, which are individually rigid. If they are now joined by a double bond, 18 degrees of freedom of the now 6 particles, minus 3 global degrees of freedom, are compared with 14 constraints from 7 bonds to ultimately give one floppy mode. However, two distinct rigid clusters connected by two double bonds makes a new rigid cluster (see Fig. 2.10b). Even one double bond and one single bond connecting to the two triangles generates one merged rigid cluster. The two spatially distinct bonds leading to rigid clusters merging in frictional rigidity percolation does not hold for central-force rigidity percolation. For central-force rigidity percolation, at least three bonds are needed to merge two independently rigid clusters. One bond fixes the distance between the two rigid clusters, the second bond the relative rotation between them and the third the shearing, provided the bonds are not all parallel with respect to each other. In the frictional case, the one double bond between the two rigid clusters fixes both the distance and the relative rotation. Rigid hinges are another means by which two rigid clusters can merge at a point and still be rigid. In central-force rigidity percolation, hinges consisting of single bonds between rigid clusters are always floppy, and so rigid hinges cannot exist. However in frictional rigidity percolation, this is not the case, at least for a hinge comprised of all double bonds, see Figs. 2.10b and d.

We conclude that two double bonds and the rigid hinge (composed of double bonds) are distinct means of propagating rigidity in frictional rigidity percolation that do not occur in central-force rigidity percolation. Both frictional motifs are more spatially localized than their central-force analogs even in the absence of floppy regions. The presence of floppy regions indeed complicates matter, as they can become rigid as well due to the merging of rigid clusters. This rigidification of floppy regions can then trigger other rigid clusters to merge, until the rigidity cascade is complete. See Figs. 2.10c, e, f. It is these very local motifs of connecting rigid clusters that can participate in a rigidity cascade to give rise to nonlocal, or distant, rigidity due to the addition of one bond. While both types of models contain such an effect, we believe that the zero-dimensional rigid cluster connector (the hinge) and the three- versus two-bond rigid cluster connectors could potentially account for the difference in exponents reminiscent of correlated percolation models such as k-core percolation where the $k = 2$ behavior is very different from the $k = 3$ behavior [64]. To more thoroughly understand the differences the two types of forces in terms of how does rigidity propagate through the system is combinatorially tricky. In the next subsection we will study a hierarchical lattice where we are easily able to perform such a task.

In contrast, to the ν and τ exponents, the structure of the ultimate spanning rigid cluster appears to not differ as dramatically between the two cases. Specifically, we observe little variation in β for the different models studied. We also observe little variation in d_f for both HC1 and HC2 studied with just central forces and with frictional forces. We will address this finding after presenting our hierarchical lattice results.

2.2.2 Hierarchical lattices

While we have presented predominantly *numerical* results so far for frictional RP and argued for a distinct universality class from central-force RP, one exactly solvable RP model is RP on hierarchical lattices. We can therefore *analytically* determine if indeed the central force RP is in a different universality class than frictional RP. To do so, we will first review prior results using the $(2,3)$ pebble game with central forces only and then generalize to the frictional version.

Review: central forces only

It has been previously shown that central-force RP transitions in such lattices exhibit a continuous rigidity transition [65, 9]. To understand this finding, let us start with the generation of a particular hierarchical lattice known as the Berker lattice [9]. Given two points and a bond as in Figure 2.11a, replace the bond with some base structure to generate a first generation hierarchical structure. This replacement continues ad infinitum to arrive at a network with an infinite number of sites between two initial points. For this particular lattice, the n^{th} generation contains 8^n bonds (with the exception of $n = 0$). To embed this lattice in two-dimensions, the bond length decreases with each generation.

To analyze rigidity in this hierarchical lattice, assume each bond has a probability $p < 1$ to be occupied. In the $n = 0$ graph, the probability of having a spanning rigid cluster between the two ends (black dots) is $p_0 = p$. In the $n = 1$ graph, the probability of being rigid between two ends can be found by subgraph counting: If all eight bonds are occupied in the $n = 1$ network, there is a spanning rigid cluster between the two ends. The probability of such a structure existing is p^8, while the probability for any bond belonging to the spanning rigid cluster is 1. All other subgraphs that contain a spanning rigid cluster, as determined by the $(2,3)$ pebble game, and their respective probabilities are listed in Figure 2.11b. Summing up all ways of having a spanning rigid cluster between the two ends of the $n = 1$ graph, we obtain

$$p_1 = 2p^5 + 2p^7 - 3p^8. \tag{2.7}$$

Given the hierarchical structure of the lattice, it is trivial to generalize this relation to

$$p_{n+1} = 2p_n^5 + 2p_n^7 - 3p_n^8, \tag{2.8}$$

from which we can solve for a fixed point, $p_c = 0.9446$, as the system approaches the thermodynamic limit, i.e. $p_{n+1} = p_n$.

In Fig. 2.11c, p_n as a function of p_{n-1} is plotted for the first four generations. We observe that the curves cross at $p = p_c$ and p_n will converge to a step function which jumps from 0 to 1 at p_c as n goes to infinity. Meanwhile, we use $P_R(p)$ to denote the probability for a bond to belong to the spanning rigid cluster. The recurrence relation for $P_R(p)$ is

$$P_{R,n+1}(p) = \frac{1}{4}\left(5p_n^4 + 13p_n^6 - 14p_n^7\right) P_{R,n} = \lambda P_{R,n}(p), \tag{2.9}$$

and near p_c, $\lambda = 0.9554 < 1$ demonstrating that the probability of a bond belonging to the spanning rigid network will approach zero as p approaches p_c. This trend suggests a continuous transition.

Expanding about p_c in both Eqns. 2.8 and 2.9 leads to $(p_{n+1} - p_c) = \lambda_1(p_n - p_c)$ and $P_{n+1}(p) = \lambda_2 P_n(p)$ such that $\lambda_1 = b^{1/\nu}$, $\lambda_2 = b^{-\beta/\nu}$, and $\lambda_3 = b^{d_f}$, where b is the length scaling factor from one generation of the hierarchical lattice to the next. For the Berker lattice, $\lambda_3 = 8$. We can therefore determine $\beta = -log(\lambda_2)/log(\lambda_1)$ and $\nu d_f = log(\lambda_3)/log(\lambda_1)$, which are both quantities that are independent of b, resulting in $\beta = 0.078$ and $\nu d_f = 3.533$.

Frictional forces

Let us now consider a "frictional" hierarchical lattice with double and single bonds to denote frictional and sliding contacts. Double bonds are introduced at random with probability q. When double bonds are taken into account, they affect subgraph constraint counting in the hierarchical lattice as we now play the $(3,3)$ pebble game to determine whether or not a subgraph has a spanning rigid cluster. Since there is an increased number of possible subnetworks in the frictional case given that the occupied bonds can be either double or single bonds, let us first discuss the $q = 1$ case. Here, there are several additional type of subgraphs containing a spanning rigid cluster that were not allowed in the central force case, as shown in Fig. 2.12a, which we can easily identify. For instance, one of the subgraphs is not allowed in the central force case because it contains a hinge structure. In the frictional case, the frustrated loops of odd numbers of vertices, or "gears", prevent rotation. These additional rigid subgraphs contribute an additional $16p^6(1-p)^2$ to the probability of having a spanning rigid cluster above the central force case. Therefore, the counting for $q = 1$ leads to the recursion relation

$$p_{n+1} = 13p_n^8 - 30p_n^7 + 16p_n^6 + 2p_n^5. \tag{2.10}$$

In the limit $n \to \infty$, we find the unstable fixed point $p_c(q=1) = 0.8533$, in addition to two stable fixed points at $p = 0$ and $p = 1$. Moreover, we can compute $P_{R,n+1}(p, q=1)$ to arrive at

$$\begin{aligned} P_{R,n+1} &= \frac{1}{4}(5p_n^4 + 48p_n^5 - 83p_n^6 + 34p_n^7)P_{R,n} \\ &= \lambda_2 P_{R,n}, \end{aligned} \tag{2.11}$$

such that $\lambda_2(q = 1) = 0.3511$. Since $\lambda_2(q = 1) < 1$, the rigidity transition is continuous with $d_f\nu = 3.181$. *This value is indeed distinct from the central force value on the same lattice thereby indicating two different universality classes.*

Now we consider $q < 1$. After keeping track of what subgraphs are rigid between the two black circles in Figs. 2.11b and 2.12a in the presence of both double and single bonds, we obtain

$$
\begin{aligned}
p_{n+1} &= p_n^8(35q^8 - 244q^7 + 474q^6 - 312q^5 + 60q^4) \\
&\quad + p_n^7(84q^7 - 210q^6 + 96q^5) + 16p_n^6q^6 \\
&\quad + p_n^5(-8q^5 + 10q^4).
\end{aligned}
\tag{2.12}
$$

With $q = 1$, the unstable fixed point occurs at $p = p_c(q = 1) = 0.8533$ with the two stable fixed points at $p = 0$ and $p = 1$. Therefore, p_n will converge to a step function as $n \to \infty$. However, for $0.8465 < q < 1$, both the unstable and nonzero stable fixed points, p_{lower} and p_{higher} respectively, are smaller than 1 so that p_n will converge to a step function which jumps at p_{lower} from 0 to p_{higher}. The reason that p_{higher} is not unity in these cases is because p denotes a double or a single bond such that when $q = 1$, $p = 1$ translates to all double bonds; however, when $q < 1$ and $p = 1$, p_{higher} depends on the ratio of double to single bonds. When $q = 0.8465$, $p_{lower} = p_{higher}$, which means when $q \leq 0.8465$, p_n will always converge to zero and rigidity transition will vanish entirely, showing that the existence of a rigidity transition in this hierarchical lattice very much depends on q. We also compute $d_f\nu$ (for $q > 0.8465$) and find that its value depends on q, as shown in Fig. 2.12b. And while there is one value of q at which the two $d_f\nu$ values are the same, β may also be different. *So, again, we find analytical evidence for two distinct universality classes.* In addition, the fact that the correlation exponent depends continuously on q is not necessarily unique as has been found in Ising models on hierarchical lattices, for example [66]. This sensitivity is presumably due to the special nature of the hierarchical lattice, as detailed in Appendix 2.5.

2.3 Minimal rigidity proliferation

For our numerical studies on the honeycomb lattice we found that the order parameter exponent β and the fractal dimension of the spanning rigid cluster at the transition d_f are not very distinct between frictional and central-force RP. Are they in fact the same, signalling features of superuniversality for the structure of the spanning rigid cluster at the transition? Or is it the case that these exponents are indeed different but the distinction is small, making it hard to detect studying finite-sized systems? If we can find a model where the order parameter exponents are actually the same—a model where the bonds are strategically placed as opposed to randomly placed, for example—this strengthens the potential for superuniversality rather than relying purely on numerical analysis, which has its limitations.

So let us now explore more explicitly connections between frictional RP and central-force RP via a subset of rigid cluster configurations using an algorithmic approach rather different from finite-size scaling. As will become clear below, connectivity percolation also enters the picture, since if we can construct spanning rigid clusters in the same way as geometrically connecting clusters, then we have evidence for superuniversality across all three models.

We will first review invasion percolation, which is motivated by the problem of one fluid displacing another from a random, porous medium [67]. More importantly for us, invasion percolation allows one to create a spanning cluster on a lattice that has the same properties as a spanning cluster in connectivity percolation. Next, we will review the Henneberg moves [68], which are used to grow a large minimally rigid network (a Laman graph) from a small minimally rigid network in the central force case. We will then extend the Henneberg moves to include frictional forces and ultimately unify the two concepts, invasion percolation and Henneberg moves. The final algorithm that we introduce, minimal rigidity proliferation (MRP), allows us to grow minimally rigid networks that span a frictional system, and *only* grow such networks.

Invasion percolation is a modified version of connectivity percolation where the spanning cluster grows along the path of smallest weights, with the following algorithm:

1. Assign uniformly distributed random numbers ranging from 0 to 1 to bonds on a lattice as their weights.
2. Occupy an initial bond, and create a list of all its neighbors. This list creates a boundary of bonds.
3. Occupy the bond from the list that has the smallest weight.
4. Update the list so that it contains all unoccupied nearest neighbors of occupied bond.
5. Repeat 3 and 4, until the occupied cluster spans the entire lattice.

The above algorithm reduces to the Leath algorithm [69], which creates the spanning cluster for bond connectivity percolation for $p > p_c$ in the following limit: Instead of occupying the boundary bond with the smallest weight, all boundary bonds whose weight is less than p are accepted into the cluster, and then the boundary list is updated. The algorithm terminates when there are no bonds on the boundary with weights less than p. This modification from invasion percolation to the Leath algorithm does not affect the large scale structure of the spanning cluster, i.e. they remain part of the same universality class [70].

Let us also review the *Henneberg moves* for building a minimally rigid network with central forces only. A minimally rigid graph in this case is also known as a Laman graph. Minimal rigidity occurs when the degrees of freedom match the constraints and there are no rendundant bonds, as determined through a $(2, 3)$ pebble game. Starting from such a network $G(N, N_B)$ with N_B bonds and N sites, one can extend it using two basic Henneberg moves as illustrated in Figure 2.13 (top):

- add one site and two bonds between this site and two points in G , then $G'(N+1, N_B+2)$ is the new minimally rigid network (Type I move).
- or add one site and three bonds between this site and three prior sites in G, then delete a prior bond between two of the selected three prior sites (Type II move).

Both moves simultaneously add two degrees of freedom and two constraints, which results in a minimally rigid graph by induction.

Now we generalize, for the first time, *Henneberg moves for the (3,3) pebble game* in order to propagate minimal rigidity. We focus on two cases: $q = 1/2$ and $q = 1$. For $q = 1/2$, we consider only a Type I move by adding a site and then adding three bonds, one double bond and one single bond (see Figure 2.13, middle). This move perpetuates minimal rigidity since no dependent constraints are introduced. For $q = 1$, i.e. all double bonds, we consider two Type II moves in series, if you will, by adding two sites, where the first site connects to two existing sites and the second new site must attach to the initial new site as well as an older site. Then, any one of the double bonds between the first new site and either old site is removed, though not the bond between the two new sites, to preserve minimal rigidity (see Figure 2.13, bottom).

Having discussed invasion bond percolation and the “growing” of minimal rigidity via generalized Henneberg moves, we are now ready to introduce *minimal rigidity proliferation*. We will first focus on $(2, 3)$ minimal rigidity and then address $(3, 3)$ minimal rigidity.

2.3.1 Central force case

To create a spanning minimally rigid cluster as defined by the $(2,3)$ pebble game, we combine the Henneberg move Type I and invasion bond percolation in the following algorithm (see Fig. 2.14 for an illustration):

1. Assign uniformly distributed random numbers ranging from 0 to 1 to bonds on the honeycomb lattice as their weights.
2. Begin by occupying a random triangle between three closest sites and create a list of all nearest and next-nearest neighbor bonds of these sites.
3. Determine the sum of the weights of any two bonds from the sites on the list that join at one site and the existing sites in the graph, find the smallest sum and occupy those two bonds.
4. Update the bond list such that it contains any unlisted nearest and next-nearest neighbor bonds of the newly added site.
5. Repeat 3 and 4, until the graph spans the lattice.

Though the graph is grown by adding two bonds at a time, as opposed to one, we still expect that this process will fall under the connectivity percolation universality class. Why? Because adding two bonds (with their additive weights) at a time involves a simple rescaling of time in which two bonds are added in one time step as opposed to two bonds in two time steps. *With this simple rescaling of time, we do not expect the structure of the spanning cluster to change between standard invasion percolation and minimal rigidity proliferation, i.e. they are the same.* Please also note that in MRP there are no floppy regions and so there is no distant, or nonlocal, rigidity.

In Fig. 2.15 we show an example of a spanning minimally rigid cluster on the honeycomb lattice with NNN bonds using minimal rigidity proliferation. We measure the fractal dimension by computing the number of sites in the cluster M as a function of total number of sites N, as shown in Figure 2.16a, and obtain $M = N^{0.958}$. Since $N = L^2$, this leads to a fractal dimension of the spanning rigid cluster at the critical point of $d_f = 1.916$, which is consistent with connectivity percolation. Figure 2.16b shows P_∞, the fraction of the system in the spanning cluster, converging to zero when system becomes infinitely large, suggesting a continuous transition just as with connectivity percolation.

2.3.2 Frictional case

Since we have extended the Henneberg moves to the $(3,3)$ pebble game for $q = 1/2$ and $q = 1$, we can generalize minimal rigidity proliferation to the frictional case. For the $q = 1$ case, two Henneberg Type II moves are made in sequence to arrive at one gowth step. With bond removal, it is not immediately clear that the minimally rigid cluster growth results in the same cluster structure as the $q = 1/2$ case, and so we leave this for future study. However, since the Type I move for $q = 1/2$ corresponds precisely to the Type I move for the central force case just with one single and one double bond, we expect the same configurations as above. *Thus, both central-force percolation and frictional RP collapse to an identical construction in this case.* Since we have already argued in the central force case, that adding two bonds at a time is a simple rescaling of time from adding one bond at a time, we also expect the $q = 1/2$ frictional process to be in the same universality class as connectivity percolation via transitivity. In other words, within this subset of growing minimally rigid configurations, we expect superuniversality to emerge: All three universality classes collapse into one all with the same exponents!

Should we have expected this result? Indeed, we should have because this strategic bond occupation does not contain floppy regions, so there is no nonlocal rigidity, and the minimal rigidity constraint maps to either adding one or two bonds at a time. In other words, MRP is a simpler model than random bond occupation given that there is no nonlocal rigidity. Interestingly, transfer matrix methods (not focusing on minimally rigid clusters) argued that connectivity and central-force percolation were in the same universality class but their results were later discounted [44, 13]. We now perhaps have some understanding as to why some exponents appear to be quite close in value in that one can add floppy, or redundant, bonds in some perturbative manner and interpolate between the two limits.

2.4 The pebble game

Maxwell constraint counting discussed in Section II assumes that every bond/constraint is an independent one. However, not every bond is an independent constraint in a random network. There may exist some redundant bonds. In order to more accurately locate the critical point where RP occurs in two-dimensional networks by keeping track of independent and redundant constraints, one can invoke the pebble game. This algorithm was described in Ref. [45] and is rooted in the following Laman condition: A two-dimensional network with N sites is minimally rigid if and only if it has $2N - 3$ bonds and no subnetwork of k sites has more than $2k - 3$ bonds [11]. To implement the Laman condition numerically requires checking all possible subnetworks, which is comptuationally expensive. The pebble game is a more computationally efficient method with a running time proportional to the number of sites times the number of bonds.

Here are a few more details of the pebble game. In a network extracted from a frictionless particle packing, since each site has 2 local degrees of freedom and there are 3 global degrees of freedom, one plays the (2,3) pebble game. Initially, there are two pebbles on each site, then these pebbles are assigned/covered to bonds one by one based on specific rules. The rules stem from an alternate version of the Laman condition, namely that the bonds in the network are independent from each other if and only if for each bond, the network formed by quadrupling the bond has no induced subnetwork of k sites and greater than $2k-3$ bonds. With this reformulation, one can check when a new bond is added to the existing set of independent bonds is itself independent via quadrupling the bond in question and invoking the Laman condition. To do this, the pebble game quadruples the new bond and tries to find a pebble covering for the 4 new bonds. If a pebble covering is not found, the new bond is not an independent constraint from the others. More specifically, the pebble game is as follows:

1. Start with a set of covered bonds and add a new bond.
2. Look at the sites emanating from the new bond. If any of those sites has a free pebble, use it to cover the bond. Give a direction to this bond such that it points away from the site that has given up the pebble. Continue with another copy of the new bond. If the pebbles of the neighboring sites already cover existing bonds, then search for free pebbles in the directed network of existing edges. Once a free pebble is found, swap pebbles and reverse the arrows on the bonds appropriately, so that the new bond is covered. Repeat this three more times. If a free pebble is found for each of the 4 copies (the quadrupled bond), then remove three of the copies and retain one bond (with its pebble and its direction) since it is added to the existing set of independent bonds. If no free pebble is found for any of the four copies, then the new bond is not independent of the current set and it is not added to the independent set of bonds.

3. Once all the bonds in the network have been tested, if $2N-3$ independent bonds are found, then the network is minimally rigid. If there are less than $2N-3$ independent bonds and no free pebbles, the network is overconstrained, or simply rigid, and if there are less than $2N-3$ independent bonds and free pebbles, the network is underconstrained, or floppy.

To identify rigid clusters in the network, one introduces a new cluster label for an unlabeled bond and gathers three pebbles at its two incident sites. Then, three free pebbles are temporarily pinned down and the two incident sites marked as rigid. For each new nearest neighbor site (to the two incident sites), a pebble search is performed. If a free pebble is found, the nearest neighbor site is not mutually rigid with respect to the initial bond nor is any other site that was encountered during a pebble re-arrangement, all these sites are floppy with respect to the initial bond. However, if a free pebble is not found, the site is mutually rigid with respect to the initial bond as well as all other sites that make up the failed pebble search and so these sites are marked as rigid. Then the next-nearest neighboring sites are visited until all nearest neighbors to the set of rigid sites have been marked floppy. All bonds between pairs of sites marked as rigid are given the same cluster label. Finally, floppy and rigid marks are removed from all sites (since a site is not unique to a rigid cluster) and the process continues until there are no unlabeled bonds. In mapping out the rigid clusters, there will be two types of bonds: isostatic bonds and redundant bonds. Isostatic bonds are critical for maintaining the rigidity of the cluster, while redundant bonds can be removed without changed the overall rigidity. Only the redundant bonds can carry stress.

For the frictional case, we must incorporate the additional rotational degree of freedom for each particle into the pebble game. In addition, to account for the additional constraints due to tangential forces in the frictional case, we introduce a second bond for each frictional contact into the network. The pebble game then explores the network to see if that additional rotational degree of freedom can be independently constrained. This second bond in the network is only added to frictional contacts below the Coulomb threshold, i.e. where the normal and tangential forces are independent of each other. For contacts at the Coulomb threshold, the tangential and normal forces are no longer independent so that only one bond in the network is needed. We, therefore, arrive at a (3,3) pebble game where contacts below the Coulomb criterion are denoted as double bonds in the network and contacts at the Coulomb threshold are denoted as single bonds in the network. Two very simple networks were discussed earlier.

2.5 General hierarchical lattices

Let us define a basic network motif with N_B bonds in a hierarchical lattice as the general first generation network and denote it by G_0. Then perform the subnetwork counting, as in Fig. 2.11b. Assuming that we find a_n rigid subnetworks which have n bonds less than the full network motif G_0, then, generically, the recurrence relation between two generations is

$$p_{n+1} = \sum_{n=0}^{N_B} a_n p_n^{N_B - n} (1 - p_n)^n. \tag{2.13}$$

Usually $a_0 = 1$, and in the specific case we discussed in the manuscript, $a_1 = 8$, $a_2 = 6$, $a_3 = 2$, and the others are zeros. The critical point is determined by the crossing point of plots of Eq. 2.13 and $p_{n+1} = p_n$. In Fig. 2.17, we can see that we need at least the first two terms of Eq. 2.13 to obtain a crossing point and that they dominate the remaining terms in determining critical point p_c. With the same method, we can obtain λ_1 by taking derivative of Eq. 2.13, or

$$\lambda_1 = \sum_{n=0}^{N_B} a_n(N_B - n)p_c^{N_B-n-1}(1-p_c)^n - a_n n p_c^{N_B-n}(1-p_c)^{n-1}, \tag{2.14}$$

and use $d_f\nu = \log(N_B)/\log(\lambda_1)$ to find $d_f\nu$. The following table lists how p_c, λ_1 and $d_f\nu$ change when we add higher order terms to first two terms in Eq. 2.13:

number of terms	p_c	λ_1	$d_f\nu$
2	0.9577	1.8290	3.444
3	0.9449	1.8069	3.5149
4	0.9446	1.8016	3.5323

Now let's investigate the first two terms in more detail: We have $p_{n+1} = p^{N_B} + a_1 p^{N_B-1}(1-p)$. To obtain a critical point, we require that

$$p_c^{N_B} + a_1 p_c^{N_B-1}(1-p_c) = p_c. \tag{2.15}$$

To make this equation solvable in the range $[0,1]$, we can rewrite it as:

$$a_1 p_c^{N_B-2} = \frac{1-p_c^{N_B-1}}{1-p_c} = 1 + p_c + p_c^2 + ... + p_c^{N_B-1}. \tag{2.16}$$

We know p_c that is a number between 0 and 1, so a solution requires that $a_1 > N_B - 1$. Since a_1 is the number of rigid subnetworks when just one bond is taken away from G_0, we have $a_1 \leq N_B$. Ultimately, we obtain the equality

$$a_1 = N_B, \tag{2.17}$$

which gives a rough criterion whether a general hierarchical lattice has a critical point, based on simple subnetwork counting.

2.6 Discussion

We have now expanded the notion of rigidity percolation to include friction in two dimensions with the extension of the $(2,3)$ pebble game to the $(3,3)$ pebble game and the incorporation of double bonds representing contacts below the Coulomb threshold. In doing so, we have uncovered a new universality class in the realm of rigidity percolation, namely that of frictional RP, which is directly compared with central-force RP on the same lattice. Such a direct comparison between two universality classes has not been possible until now. By expanding the scope of RP, the direct comparison presented here should help to formulate a more general framework for rigidity transitions just as there exists a general framework for spin systems, with and without disorder, to understand how a transition in the 3-state Potts model is in a different universality class from the one in the Ising model.

We make this direct comparison between central force RP and frictional RP on honeycomb lattices with additional next-nearest bonds. We find different correlation length and non spanning rigid cluster size distribution exponents ν and τ respectively between the two cases, but a statistically similar order parameter exponent and fractal dimension of the spanning rigid cluster at the transition. Given the different ν and τ, we propose that local motifs, such as two double bonds and a rigid hinge composed of double bonds, are ways to connect rigid clusters in frictional RP that are distinct from central-force RP. Neither construct is rigid in central-force RP, and additional supporting bonds are necessary. The less strict rigid cluster connection mechanisms in frictional RP compared to central-force RP potentially drive the distinction between universality classes. For the hierarchical lattice, not only are there two different universality classes, frictional and central-force RP, that can be shown analytically, the exponents also depend continuously on the fraction of double bonds.

Motivated by the small difference in order parameter exponent in central-force and frictional RP, we combined Henneberg moves (here extended to the $(3,3)$ pebble game) and invasion percolation to construct another new model, *minimal rigidity proliferation* (MRP), that can be implemented for both types of forces. The rigid cluster in MRP grows in a simple fashion, unlike in RP where rigid clusters surrounded by floppy regions can lead to a rigidity cascade. With minimal rigidity proliferation, there are no floppy or even redundant bonds—the spanning rigid cluster is built in a "clever" way, which is to be contrasted with the tuning by pruning approaches [71], where springs are removed while conserving the bulk modulus, for example, and the jamming graph approach [72] where minimally rigid clusters follow the geometric constraint of local mechanical stability. With the strategic bond growth in minimal rigidity proliferation, the order parameter exponent is the same across connectivity, central-force RP, and frictional RP. This would be the first time superuniversality is observed in RP in a way that goes beyond transfer matrix methods [44]. Our work also suggests that looking at minimally rigid configurations—a subset of all possible configurations within RP—represents a new way of viewing phase transitions in the sense that nested within two distinct universality classes there could be an underlying superuniversality establishing deeper connections between the classes than previously thought.

Since frictional RP was devised to explore the nature of the jamming transition in frictional particle packings, this work compels us to make a rather strong claim that the rigidity transition in frictionless particle packings with purely repulsive central forces is of a different nature than the rigidity transition in frictional particle packings. In fact, the frictionless case with purely repulsive central forces may indeed be a very special case because even rigid cluster analysis of particle packings with both attractive and repulsive central forces indicates a continuous transition [73]. In frictionless packings, there are no redundant bonds, which makes the constraint counting rather straightforward. However in frictional packings, redundant bonds emerge such that the constraint counting is more intricate and, therefore, perhaps non-mean-field. It will be interesting to apply the frictional (3,3) pebble game to experimental frictional particle packings to test the applicability of our approach as well as to compare the rigid clusters with dynamical matrix calculations. And very recently, the frictional (3,3) pebble game has been applied to frictional packing derived beam networks to predict fracture locations near the brittle-ductile transition [74].

Finally, we are currently exploring a limitation of the $(3,3)$ pebble game [75]. Specifically, if there are four particles forming a square and all four contacts are below Coulomb threshold, then we have a square with all double bonds (like the middle image in Figure 2.4 without the diagonal bond). From the $(3,3)$ pebble game perspective, this configuration is floppy, and there is one floppy mode where the particles are in a gearing motion. However these four particles are rigid under strain, since the pure spin mode does not couple to translations, and so one can play a $(3,4)$ pebble if one is interested only in translational rigidity. More generally, odd loops of double bonds do not contain this pure spin mode, while even loops of double bonds do. This complication can be addressed by keeping track of even and odd loops of double bonds. Any odd loop intersecting an even loop destroys the gearing mode, and we relabel the loop as even. If there are no even loops after looking at intersections of even and odd loops, then the original $(3,3)$ pebble game is robust at all length scales. Near the transition where system-spanning length scales dominate, the initial version of the $(3,3)$ pebble game is also robust as long as there is no cluster-spanning set of even loops, which is unlikely due to the intersection with odd loops such as triangles. Note also that the low-energy normal modes of rigid frictional packings show a rough equipartition between rotational and translational degrees of freedom and do not contain any purely rotational modes [62].

In closing, our work opens up many new avenues for exploration in rigidity percolation with new constraint counting methods and the discovery of potentially new universality classes. It also invites us to explore not only rigid regions but floppy regions as well, which may be the key in constructing field theories of continuous rigidity percolation transitions. Finally, our new optimal rigid cluster growth algorithms do not waste material and, therefore, perhaps have a chance of being realized in living matter as well as provide mechanical examples for decision-based cluster growth that may draw links with explosive percolation [76].

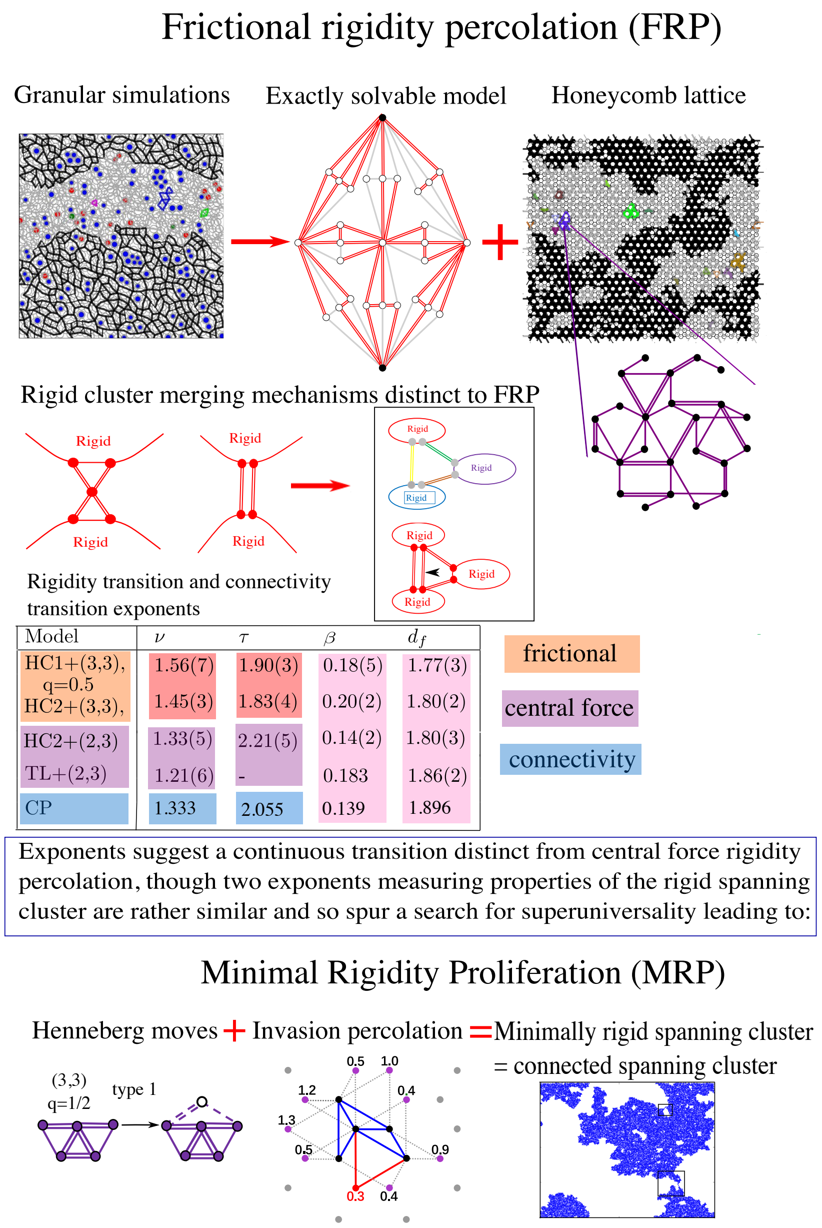

Model	ν	τ	β	d_f
HC1+(3,3), q=0.5	1.56(7)	1.90(3)	0.18(5)	1.77(3)
HC2+(3,3),	1.45(3)	1.83(4)	0.20(2)	1.80(2)
HC2+(2,3)	1.33(5)	2.21(5)	0.14(2)	1.80(3)
TL+(2,3)	1.21(6)	-	0.183	1.86(2)
CP	1.333	2.055	0.139	1.896

Exponents suggest a continuous transition distinct from central force rigidity percolation, though two exponents measuring properties of the rigid spanning cluster are rather similar and so spur a search for superuniversality leading to:

FIGURE 2.2: *Graphical abstract.* In conjunction with the abstract and the introduction, the above serves as a visual guide to the manuscript.

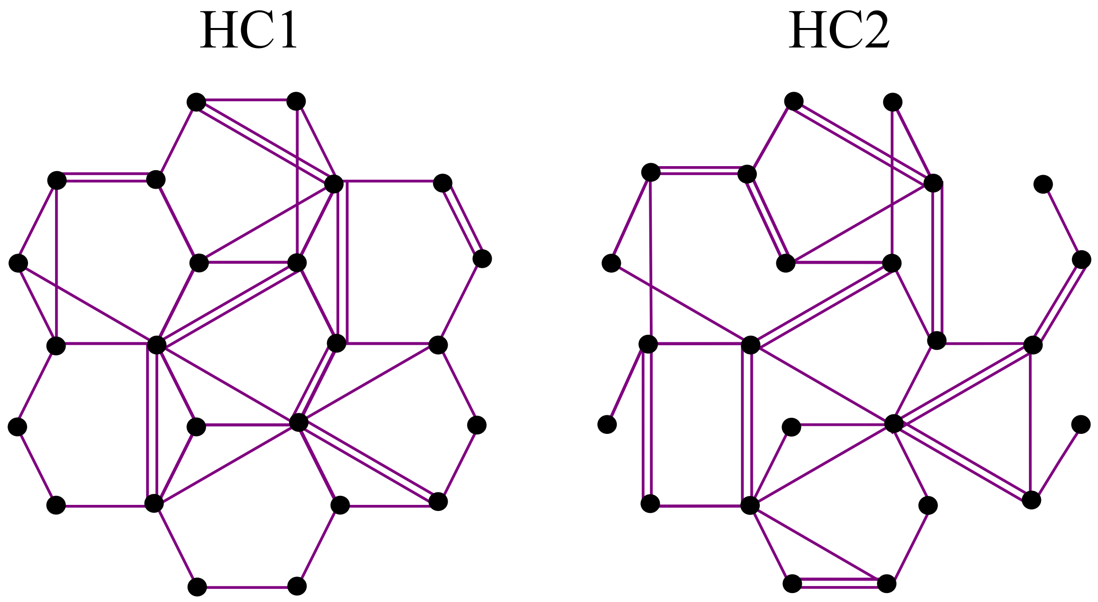

FIGURE 2.3: *Schematic frictional rigidity percolation models HC1 and HC2.* These random networks are constructed by either adding next-nearest neighbor (NNN) bonds to an occupied honeycomb lattice (HC1) or adding random first and second neighbor bonds (HC2), all with probability p. Double bonds denote frictional/gear-like bonds, which occur with probability q, while single bonds denote sliding bonds.

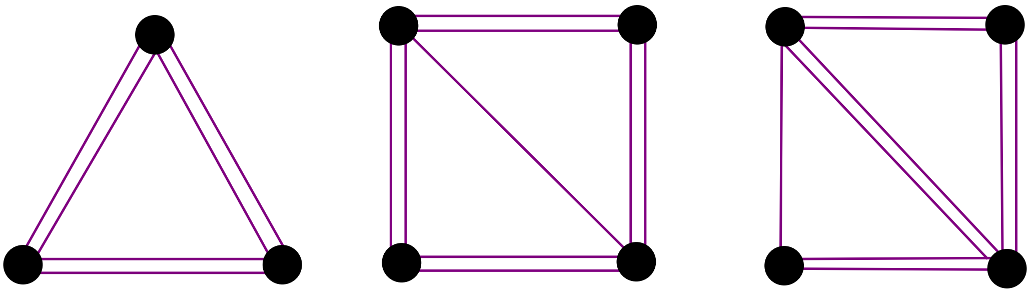

FIGURE 2.4: *Small minimally rigid clusters.* For a triangular constraint network with all double bonds, this network is minimally rigid via the $(3,3)$ pebble game. For a four-site constraint network, there are 5 possible configurations in which this network is minimally rigid via the $(3,3)$ pebble game, two of which are presented.

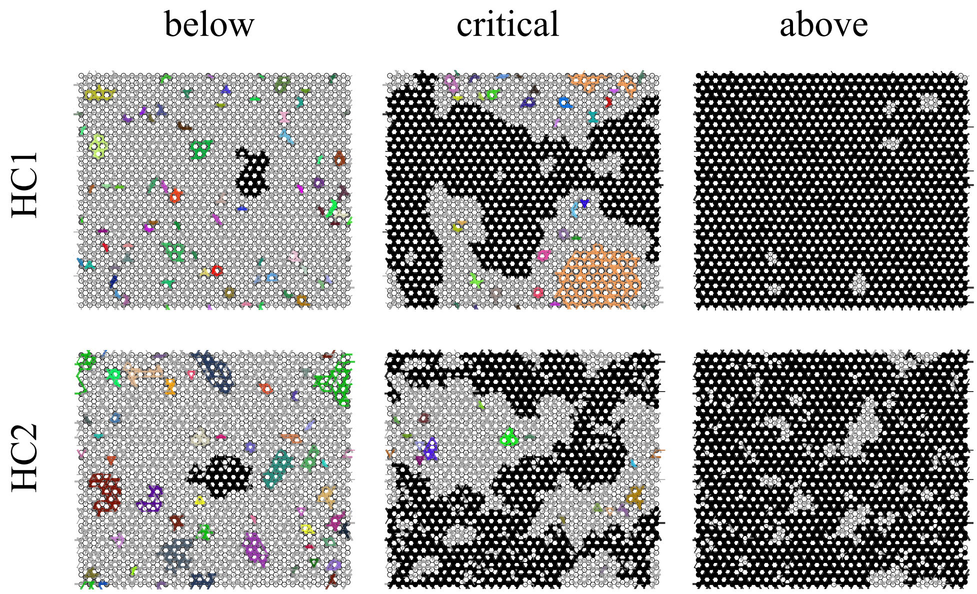

FIGURE 2.5: *Rigid clusters in frictional rigidity percolation.* Rigid clusters below, at, and above the rigidity transition for $HC1$ and $HC2$ with $q = 0.5$. Rigid clusters are colored, with the largest cluster in black, while floppy regions are in grey.

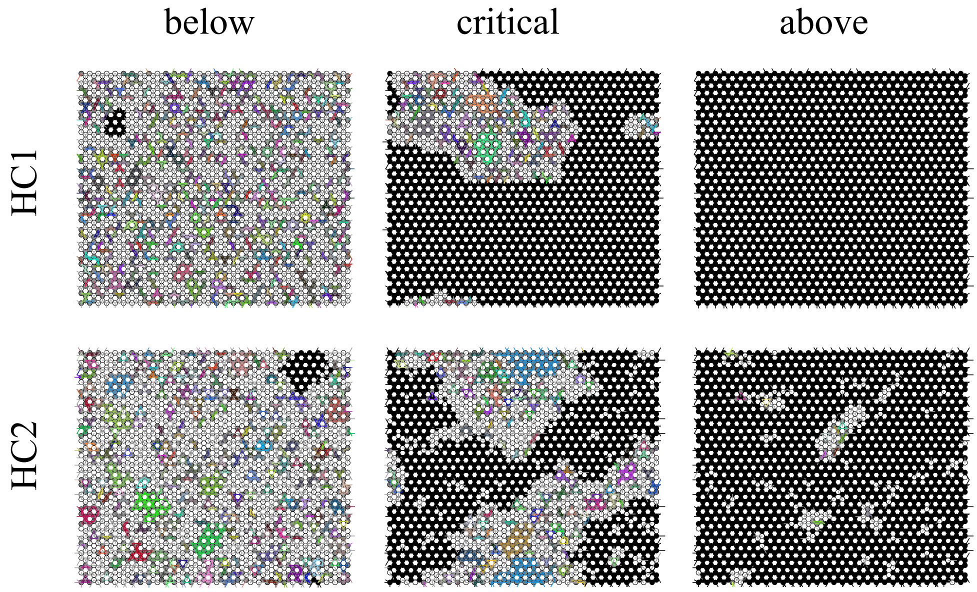

FIGURE 2.6: *Rigid clusters in central-force rigidity percolation.* Rigid clusters below, at, and above the rigidity transition for $HC1$ and $HC2$. The black indicates the largest rigid cluster, and floppy regions are gray again.

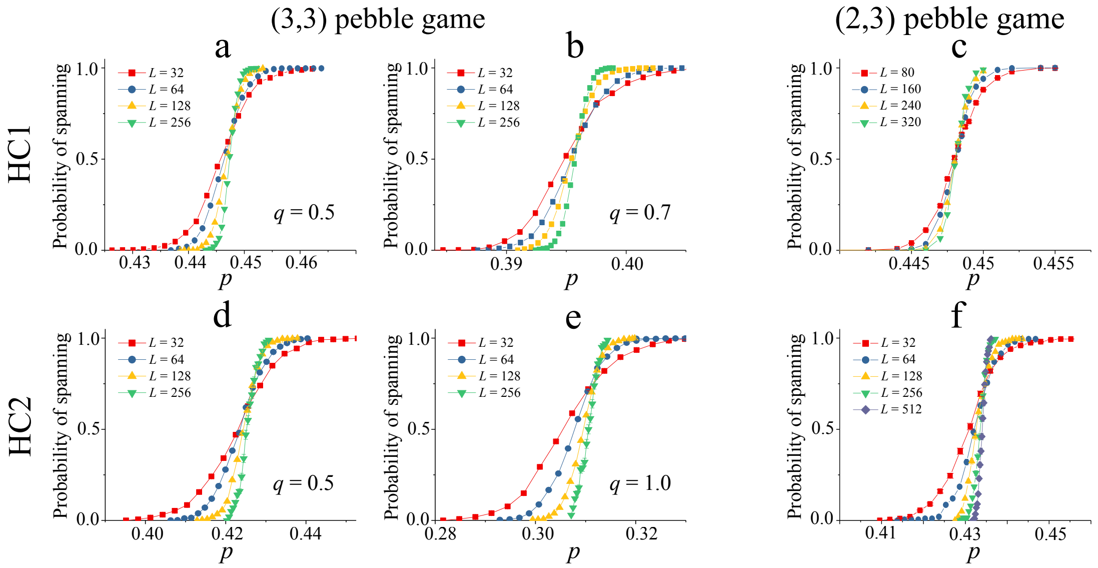

FIGURE 2.7: *Spanning rigid cluster probability.* Probability of having a spanning rigid cluster as a function of p for lattices of different lengths L for different models, with HC1 in the top row and HC2 in the bottom row and the (3,3) pebble game results (frictional) on the left, while the (2,3) pebble game results (central-force) are on the right. Solid lines are fits to the data using an error function as a fitting function. Data points are averaged over 2500 samples for the (3,3) game and over 1000 samples for the (2,3) game.

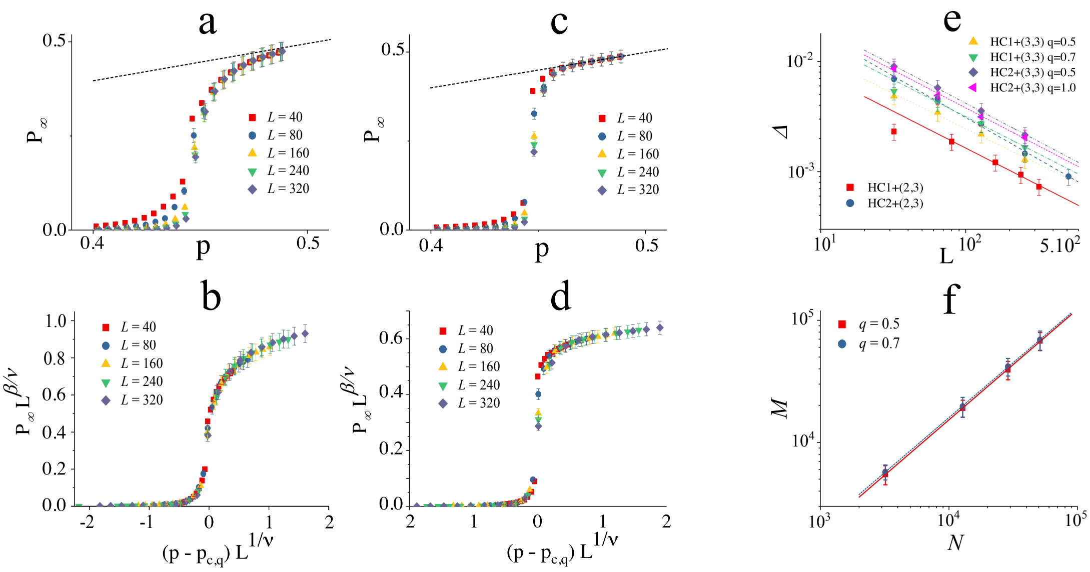

FIGURE 2.8: *Finite-size scaling analysis to obtain exponents β, ν, and d_f.* (a) For $HC1$ with $q = 0.5$, we plot P_∞, the fraction of occupied bonds in the largest rigid cluster, as a function of p for different system sizes. We observe $P_\infty \sim (p - p_c(q))^\beta$ just above critical point and tends towards p further away from the transition. (b) Collapse of (a) using $p_c(q) = 0.448$, $\nu = 1.56$, $\beta = 0.18$. (c) P_∞ for $HC1$ with the $(2,3)$ pebble game as a function of p for different system sizes. (d) Collapse of (c) using $p_c(q) = 0.448$, $\nu = 1.54$, $\beta = 0.07$. (e) Δ, as defined in eq. 2.4, versus system length L for six different cases of the model. (f) Log-log plot of the number of bonds in the spanning cluster M versus L for $HC1$ with $q = 0.5$ and $q = 0.7$.

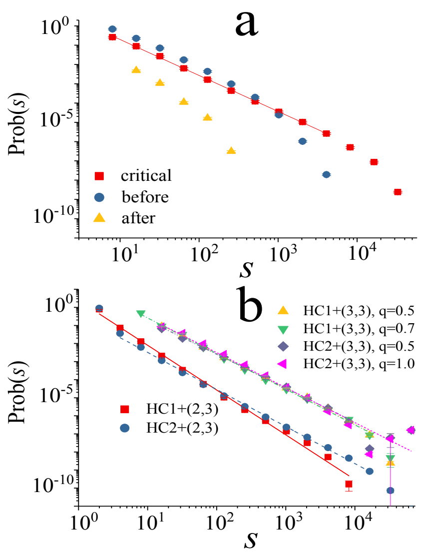

c

Model	p_c	ν	τ	β	d_f
HC1+(3,3), q=0.5	0.447(1)	1.56(7)	1.90(3)	0.18(5)	1.77(3)
HC1+(3,3), q=0.7	0.396(1)	1.49(6)	1.97(3)	0.18(5)	1.74(3)
HC2+(3,3), q=0.5	0.427(2)	1.45(3)	1.83(4)	0.20(2)	1.80(2)
HC2+(3,3), q=1.0	0.312(2)	1.46(7)	1.96(4)	0.20(2)	1.80(3)
HC1+(2,3)	0.448(1)	1.50(7)	2.45(6)	0.07(1)	1.72(2)
HC2+(2,3)	0.434(1)	1.33(5)	2.21(5)	0.14(2)	1.80(3)
TL+(2,3)	0.660(3)	1.21(6)	-	0.183	1.86(2)
CP	0.342	4/3	187/91	5/36	91/48

TL: triangular lattice

CP: connectivity percolation

FIGURE 2.9: *Analysis to obtain exponent τ and summary table.* (a) $HC1$ with $L = 320$ and $q = 0.5$, the red squares show the probability for having finite rigid clusters with different sizes very close to the transition point. Blue circles and yellow triangles show the distribution below and above rigidity transition, respectively. (b) Non spanning cluster size probability distribution at p_c for the six different cases of the model. (c) This table lists the types of rigidity transitions and some critical exponents for the different models defined as follows: $\xi \sim (p - p_{c,q})^{-\nu}$ is the correlation length and diverges at critical point; the non spanning rigid clusters size obeys a broad distribution, $n_s \sim s^{-\tau}$, at the critical point; d_f is the fractal dimension of spanning rigid cluster at the rigidity transition; β is the order parameter exponent; q is the percentage of contacts as double bonds. As a point of references, exponents in RP exponents from the triangular lattice (TL) using the $(2,3)$ pebble game, as well as ordinary connectivity percolation (CP) exponents are listed at the bottom of the table.

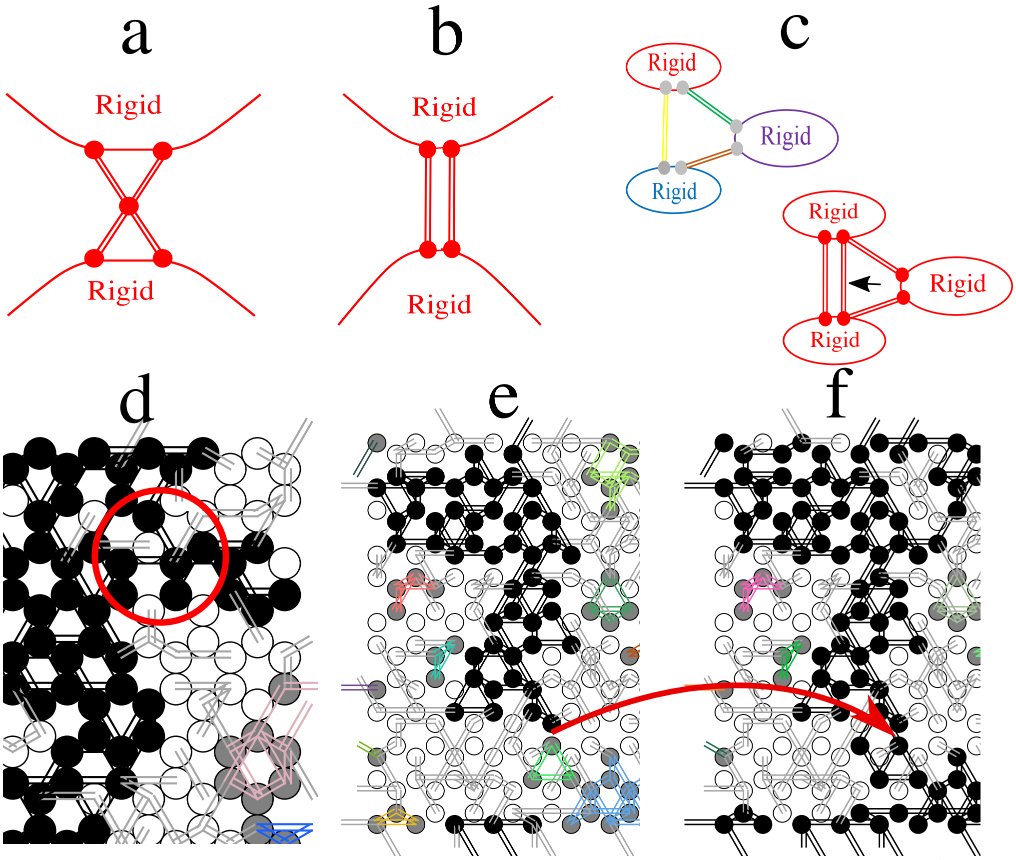

rigid hinge

add one double bond and create spanning cluster

FIGURE 2.10: *Rigid cluster merging mechanisms for frictional rigidity percolation.* (b) Schematic hinge linking two rigid clusters. (a) Schematic double bond linking two rigid clusters. (c) Merging three rigid clusters linked by three floppy double bonds into one rigid structure with the addition of one double bond indicated by the black arrow. (d) Example of a hinge in HC2. (e)-(f) Adding exactly one double bond merges and grows five smaller rigid clusters into a new spanning rigid cluster.

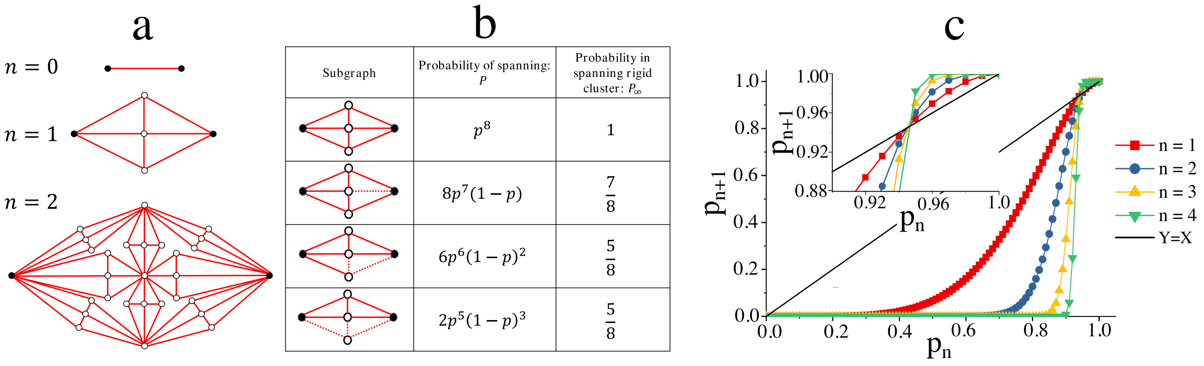

FIGURE 2.11: *Central-force rigidity percolation on a hierarchical lattice.* (a) First three generations of hierarchical Berker lattice. (b) Subnetwork counting: dashed bonds are not occupied. Every type of subnetwork is a way to obtain a spanning rigid network between two ends(black dots) and its probability is calculated, as well as the probability for an occupied bond to be in the spanning rigid cluster. (c) First four p_n as function of p. p_n tends to converge to a step function at $p_c = 0.9446$ which jumps from 0 to 1.

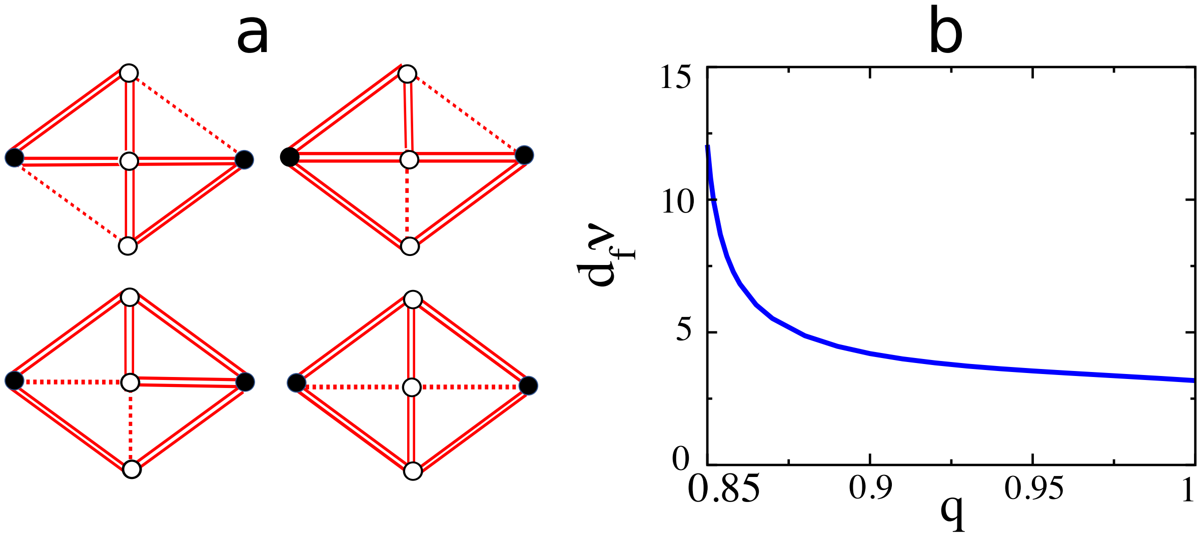

FIGURE 2.12: *Frictional rigidity percolation on a hierarchical lattice.* (a) Allowed rigid subgraphs for the $q = 1$ case with the $(3,3)$ pebble game that are not allowed with the $(2,3)$ pebble game. (b) Plot of $d_f\nu$ versus q for frictional RP on the Berker hierarchical lattice.

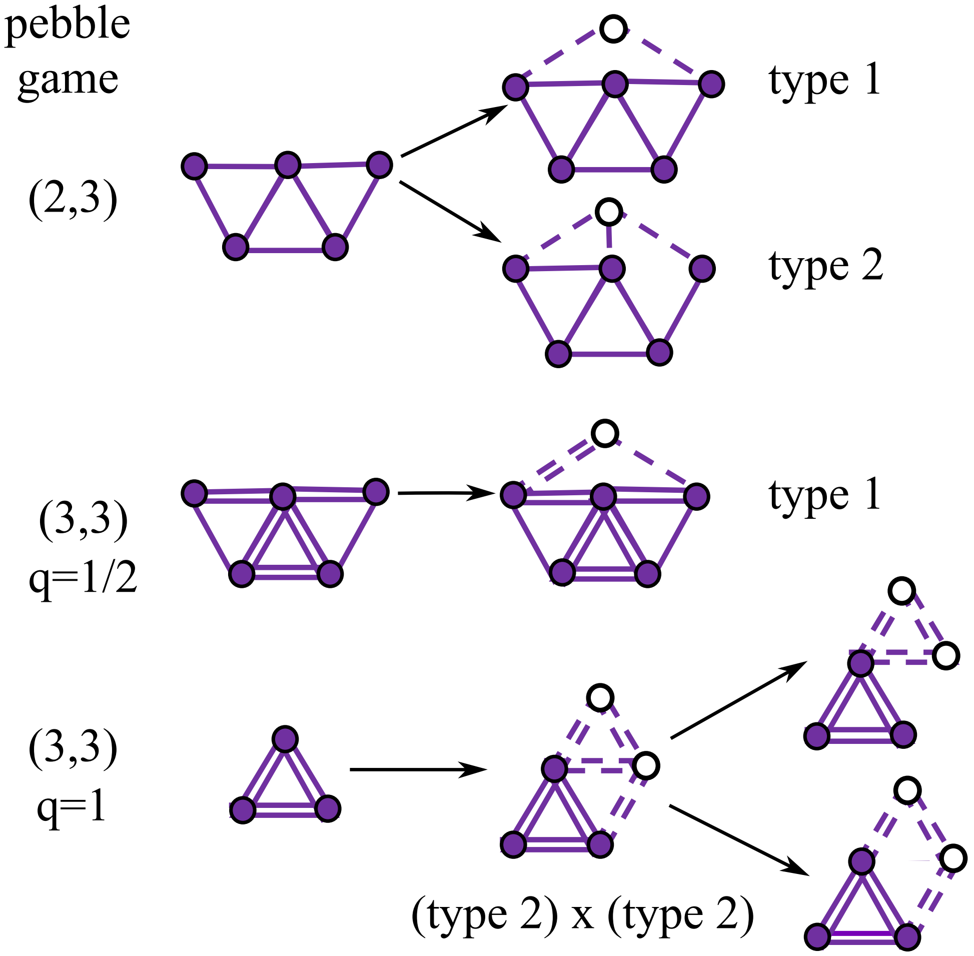

FIGURE 2.13: *Henneberg moves.* Schematic of Type I and Type II Henneberg moves for the central-force (2,3) game (top) and for the frictional (3,3) game (middle and bottom).

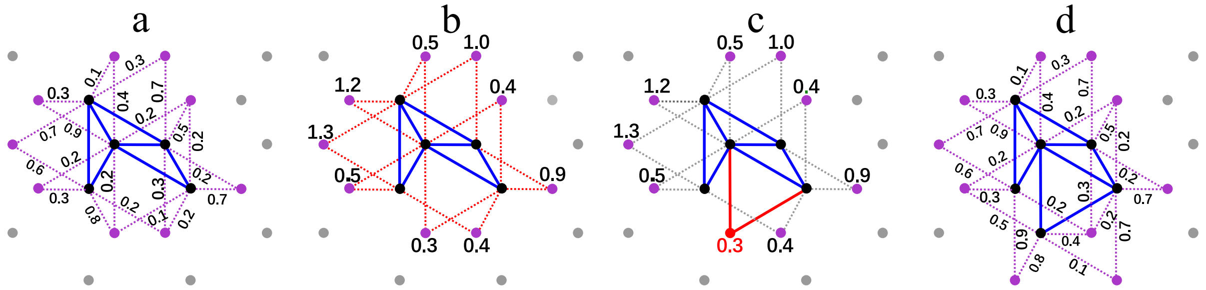

FIGURE 2.14: *Schematic of minimal rigidity proliferation (MRP).* (a) Existing rigid cluster (blue) surrounded by nearest and next-nearest bonds with their respective weights (purple). (b) Minimal sum of weights from bond pair has been associated to sites; candidate Henneberg move pairs are in red. (c) The move is executed at the site with the lowest total weight. (d) New rigid cluster surrounded by nearest and next-nearest bonds.

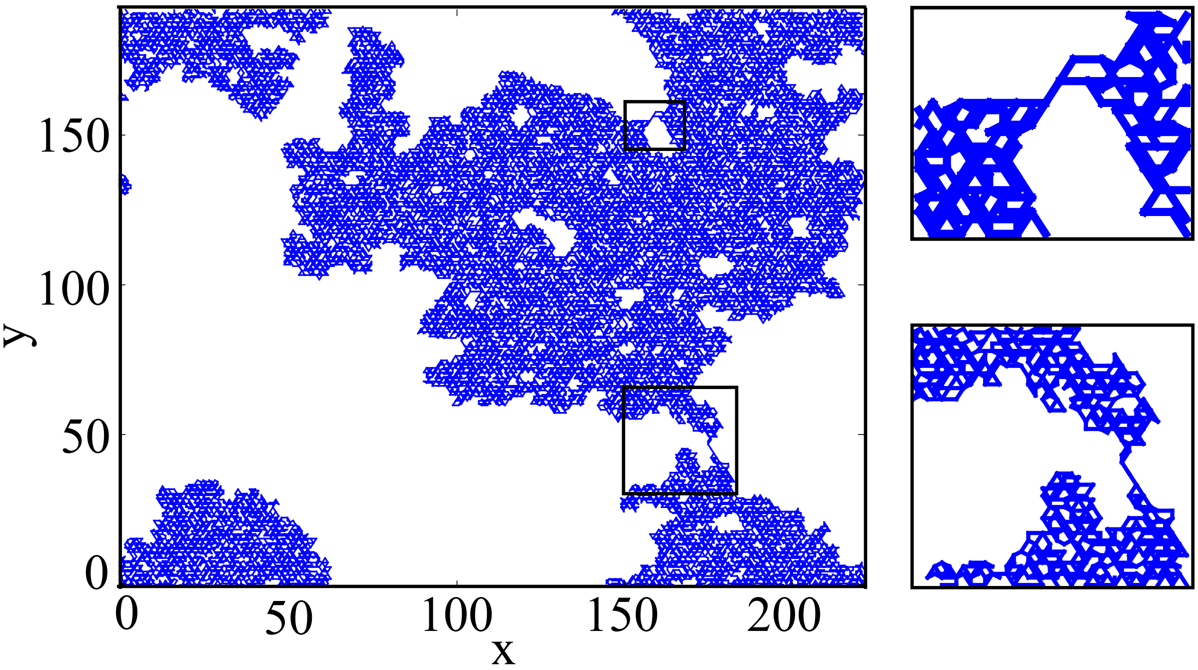

FIGURE 2.15: *Generated spanning clusters.* An example of spanning rigid cluster constructed using minimal rigidity proliferation; two examples of rigid hinges are shown in more detail on the right.

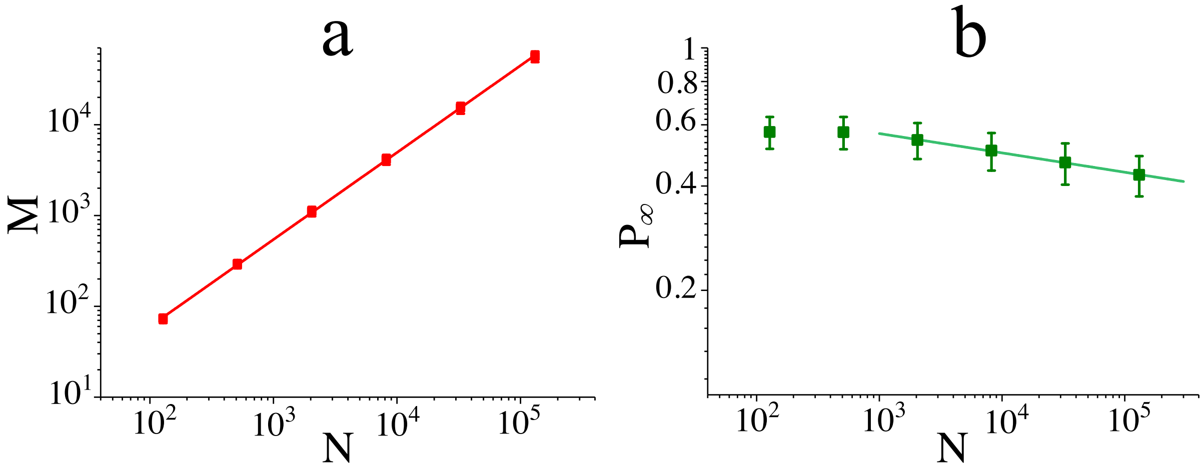

FIGURE 2.16: *MRP cluster property analysis.* (a) Log-log plot between size of spanning cluster at the critical point M and size of whole system N. The slope of less than one indicates that the spanning cluster at the critical point has a fractal dimension $d_f = 1.916 \pm 0.010$. (b) As the system size increases, P_∞ goes to zero, suggesting a continuous transition. All plots have been averaged from 935 samples.

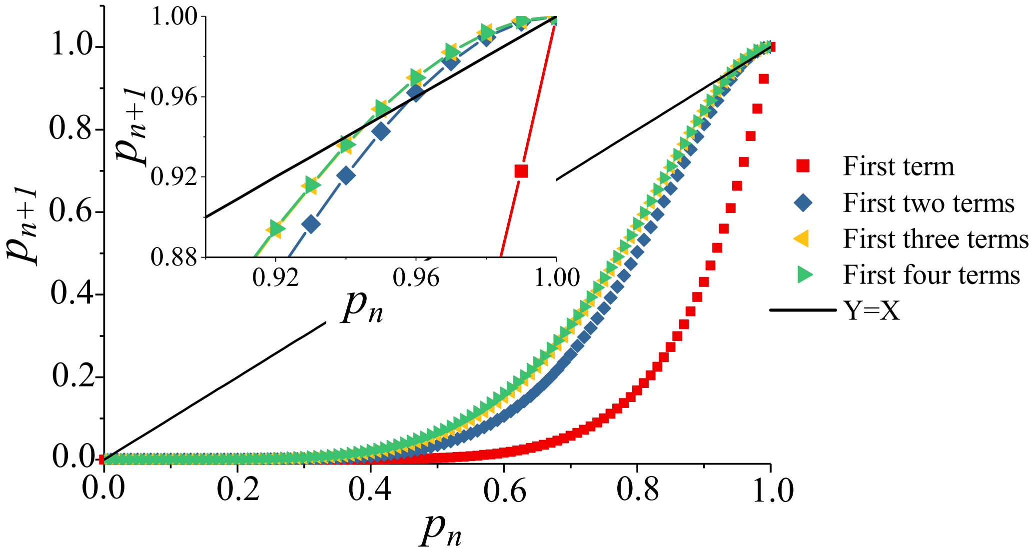

FIGURE 2.17: First four p_n as function of p for the $(3,3)$ game on general hierarchical lattices; p_n needs at least the first two terms to generate a crossing point.

Chapter 3

Rigid clusters in frictional granular packings

This chapter is based on work primarily presented in the manuscript "Sponge-like rigid structures in frictional granular packings" co-authored by Jonathan E. Kollmer, Karen E. Daniels, J. M. Schwarz and Silke Henkes and is in peer review. Manuscript is available on arxiv. Jonathan E. Kollmer and Karen E. Daniels operated all experiment related work. J. M. Schwarz, Silke Henkes and I developed algorithms. Silke and I wrote codes for analysis and I performed all analysis from experimental data. All our co-authors provided valuable suggestions and edits to improve the presentation and the content of this manuscript.

3.1 Two approaches to rigidity

Rigidity is the ability of a system to resist imposed perturbations; for disordered materials, their detailed internal structure determines rigidity [77, 78]. The Maxwell counting criterion [10], first developed for building girder frameworks in 19th century railway bridges, has long been used to compute the stability of system by comparing the number of constraints to the number of degrees of freedom [12]. This simple, effectively mean-field, criterion also correctly predicts the onset of positive bulk and shear moduli in frictionless jamming of spherical particles (e.g. foams or emulsions) [22, 58, 79, 80]. However, when friction is introduced, as required for modeling granular materials, the counting argument no longer works, even with modifications [81, 82, 25]. In particular, systems which acquire rigidity under shear do so at lower packing fractions than those loaded isotropically, via the appearance of anisotropic, load-bearing force chains, in a phenomenon known as shear-jamming [25]. These findings highlight the importance of local structure, and raise the question of the suitability of a mean-field criterion. The common practice of counting Maxwell constraints only after removing the *rattlers* [22, 56] (particles with few contacts) has further obscured this issue.

A first approach to local rigidity, linear response theory, uses the detailed local geometry and forces to compute the *dynamical matrix* (or Hessian) of the system [83]. A rigid packing will have no system-spanning zero-modes in the dynamical matrix, except for global translations and rotations; conversely their presence indicates a lack of rigidity. In frictionless systems, this method agrees with the result of Maxwell constraint counting, after removing rattlers [83]. In frictional systems, the same comparison was made using a dynamical matrix extended to include friction [84, 62]. In simulations of frictional packings equilibrated at constant pressure, the results from this extended dynamical matrix match a generalised form of the constraint counting argument, creating a frictional jamming transition along a generalised isostaticity line [82, 62]. Other modified isostatic conditions have been proposed for frictional systems [85, 86], but none have yet been experimentally tested.

A second approach to quantifying local rigidity focuses on the spatial patterns of rigid clusters, which are sets of connected bonds that are mutually rigid with respect to one another [6]. In this *rigidity percolation* framework, the rigidity transition corresponds to the emergence of a spanning rigid cluster in the contact network. In 2D,

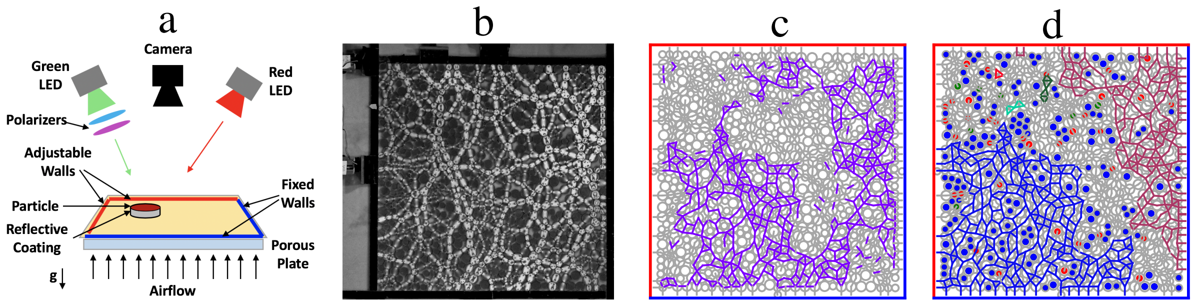

FIGURE 3.1: (a) Schematic of the experimental setup with fixed walls (blue) and moving walls (red). (b) Sample image, showing just the polarized channel (photoelastic respose). (c) Rigid region decomposition of sample (b), computed using the dynamical matrix; the rigid region is purple, and floppy bonds are grey. (d) Rigid cluster decomposition of sample (b), computed using the pebble game; it contains two large rigid clusters (blue and red bonds), some smaller rigid clusters (other colors), and regions of floppy bonds (grey). Blue particles are rattlers with zero constraints.

the *pebble game* [45] uses Laman's theorem to construct a generic algorithm for decomposing a network into rigid clusters and floppy regions. This theorem depends only on the network topology and does not require information about forces and contact geometry. Analysis of 2D systems show that frictionless packings exhibit a discontinuous rigidity transition [87], while generic central-force networks exhibit a continuous transition [13, 14]. Rigidity percolation has also provided insights into the structure of colloidal gels with attractive interactions [73, 88, 89]. Recent work [26] has extended the pebble game to frictional packings and showed that networks derived from slowly-sheared frictional simulations generate rigid cluster structures consistent with a continuous transition. Using a simplified network model, we have additionally established the transition as continuous, but with exponents that differ from standard (central-force) rigidity percolation [8]. Simulations on shear-jammed states further indicate that the onset of shear jamming corresponds to the percolation of overconstrained regions with a broad range of sizes [90]. Experimental tests of rigidity percolation for frictional systems are absent.

In this chapter, we apply both the dynamical matrix and the pebble game to data from experiments on 2D *frictional* granular packings. We measure particle positions and forces within a monolayer of quasi-statically sheared grains floating on a gentle cushion of air [91, 92], with interparticle forces obtained using photoelasticity [93, 94]. We find that both the frictional dynamical matrix and the frictional pebble game agree with each other, providing nearly identical decompositions of the packings into rigid and floppy regions, and that there is a strong correlation between local pressure and local rigidity. The transition in our finite-sized system occurs at $z_c = 2.4 \pm 0.1$, well below the mean field value $z_c = 3$. We discover that the rigid structures are sponge-like, i.e. containing a broad range of floppy hole sizes, particularly near the transition, which is again a signature of a continuous transition inconsistent with mean-field rigidity.

3.2 Experiments

We perform experiments on a monolayer of $N = 826$ photoelastic bidisperse disks (Fig. 3.1a). The two particle radii are $R_1 = 5.5$ mm and $R_2 = 7.7$ mm (with $R_2/R_1 = 1.4$)), and the particles are initially confined to an area of approximately $L = 0.5 \times 0.5\ \mathrm{m}^2$. Details about particles mechanical properties are discussed in Appendix 3.D.1. Two of the confining walls are controlled by stepper motors; to impose simple shear, one wall moves in while the other moves out in a series of quasi-static steps of size $\Delta x = 1.5$ mm, with Δy adjusted to maintain constant area A. After n steps, each resulting in a shear strain $\epsilon = \frac{\Delta x}{L} \approx 0.003$, the shear is reversed back to the initial state. The number of steps is not fixed, but ranges from $n = 8$ (ending at a total stress threshold) to $n = 13$ (pre-defined maximum). The floor of the shear cell is a porous frit through which air flows to allow the particles to float on a gentle air cushion, creating a system without basal friction; this apparatus is largely the same as the one described in [91, 92]. Therefore, the external load from the two walls is the only significant external stress. The complete dataset consists of 24 cyclic runs, with each run starting from randomized particle positions and an initial barely-jammed volume. The packing fraction for each of the 24 runs is in the range $0.746 < \phi < 0.760 \pm 0.006$. During each cycle, contacts are created through shear during the first half of the cycle (dubbed 'shear'), and partially released during the second half of the cycle (dubbed 'unshear'); due to shear-jamming [25, 95], the system does not return to its initial state after a complete cycle. Datasets where we could not track all particles where discarded. A total of 353 images are used in the analysis below. Since the particles are made of a birefringent material (Vishay PhotoStress PSM-4), we are able to use photoelasticity [93, 94] to measure the vector contact forces on all particles; a sample image is shown in Fig. 3.1b. The red channel (not shown) uses unpolarized light and measures particle positions, and the green channel (shown) uses circularly polarized light to measure the photoelastic signal. From the later, we determine the normal and tangential contact forces (f_n, f_t) on each particle using our open-source algorithms [93, 96](see Appendix 3.A). From measurements of the normal f_n and tangential f_t contact forces, we estimate a friction coefficient of $\mu = 0.3$ (see Appendix 3.D.3). The Coulomb threshold for the mobilisation $|f_t|/\mu f_n$ determines whether a contact is sliding (≥ 1) or frictional (< 1); its distribution has so far only been analysed in simulations [82]. The rigidity calculations, described below, depend sensitively on the correct determination of whether two particles are in contact. Rest of sections in this chapter provides information on how we determine the optimal parameters. In all cases, we find that values of the mean coordination number are known to within ± 0.1.

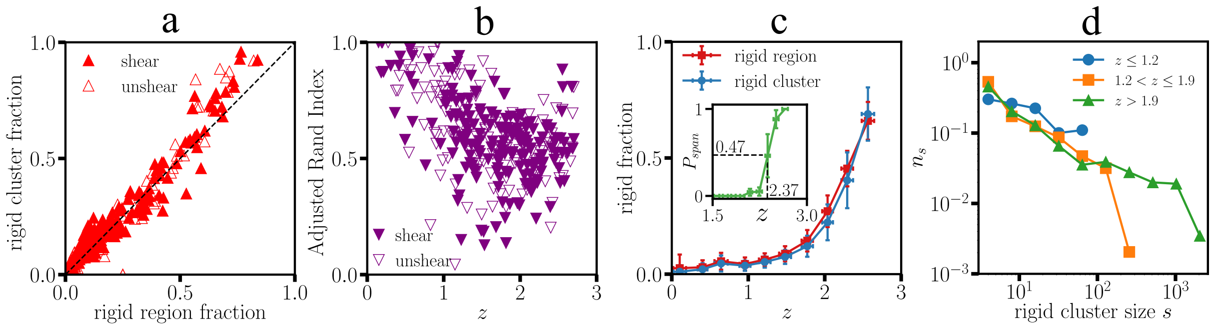

FIGURE 3.2: Correlations between rigid clusters and regions, calculated on the 353-image dataset. (a) Correlation between the rigid cluster fraction and the rigid region fraction. (b) Adjusted Rand index (ARI) between the rigid cluster decomposition and the rigid region decomposition. (c) Fractions of rigid clusters and rigid regions as function of average coordination number, z. Inset: Probability of a spanning rigid cluster. (d) Histogram of cluster size s, taken for three different ranges of z.

3.3 Rigidity computations

We first compute the vibrational modes of the system, starting by expanding the equations of motion about mechanical equilibrium

$$\delta \ddot{r}^i_\alpha = -D^{ij}_{\alpha\beta}\delta r^j_\beta + \text{dissipation}(\delta \dot{r}) + O(\delta r^2), \tag{3.1}$$

where $D^{ij}_{\alpha,\beta} = \frac{1}{\sqrt{m_{i,\alpha}m_{j,\beta}}}\frac{\partial^2 V_{ij}}{\partial r_{i,\alpha} r_{j,\beta}}$ is the dynamical matrix of the system, the indices (i,j) label all disks, (α,β) label the two spatial x, y components and the angular component $R\theta$, and m denotes the particle mass. While frictional interactions are not conservative, one can nevertheless derive an effective potential in linear response (see Appendix 3.C.2). We arrive at $V^f_{\text{eff}} = \frac{1}{2}K_t\delta t^2$ for a contact with stiffness K_t during tangential contact loading, where δt is the tangential displacement at the contact point. For a sliding contact at the Coulomb threshold, we approximate that the shear dynamics does not reverse the sliding direction. We have verified this assumption in sheared simulations and do not include the shear-reversal step in our analysis here. We obtain $V^f_{\text{eff}} = \pm\mu f_n \delta t$, where f_n is the value of the normal force at equilibrium. Then the effective potential becomes [84, 62]

$$V_{ij} = \frac{1}{2}\left[K_n(\delta\mathbf{r}\cdot\hat{\mathbf{n}})^2 - f_n/|\mathbf{r}_{ij}|\left(\delta\mathbf{r}\cdot\hat{\mathbf{t}}\right)^2 + V^f_{\text{eff}}\right], \tag{3.2}$$

with normal elastic stiffness K_n, and where the third term arises only for friction. To construct the dynamical matrix for our experimental data, we use measured masses for m, and estimate K_n from the elastic modulus of the material. To ensure that tangential and normal interactions contribute at the same order, we set $K_t = K_n$. Using the particle positions and interparticle forces, we then construct the dynamical matrix and compute its normalized eigenmodes(see Appendix 3.C.3). The zero eigenvalue modes parametrise the floppy motions, and we determine translational and rotational relative displacements at contacts between disk pairs. We then compute the mean square displacement over floppy modes at individual bonds and mark all bonds with a displacement below (above) a threshold value $2 \cdot 10^{-5}$ as rigid (floppy); there is mild threshold dependence (see Appendix 3.D.3). In the transition region, we obtain sets of contiguous rigid bonds that form *rigid regions*, shown in Fig. 3.1c(more in Appendix 3.C.4).

Our second method of measuring rigidity is to decompose the system into rigid clusters using the frictional pebble game. To do so, we extend the central force $(k = 2, l = 3)$ pebble game applied to a contact network to a $(k = 3, l = 3)$ pebble game in order to incorporate the additional rotational degree of freedom made relevant by the friction between disks. Moreover, each contact below the Coulomb threshold contributes two constraints (one normal and one tangential), while each contact at the threshold (freely sliding) only contributes a normal constraint [26, 8]. To this constraint network, we add an appropriate number of constraint bonds between the four boundaries in the experiment and all contacting particles (see Appendix 3.B.1). A sample decomposition is shown in Fig. 3.1d.

3.4 Results

Using the particle positions and inter-particle forces obtained from experiments, we apply the dynamical matrix method and the frictional pebble game to determine *rigid regions* and *rigid clusters*, respectively. Fig. 3.1c-d, performed on an image near the onset of jamming, illustrates that the identified rigid clusters/regions are closely correlated. This correspondence remains true for our full dataset: Fig. 3.2a is a scatter plot of the measured rigid cluster fraction against the rigid region fraction. All data points are clustered around the diagonal, with no difference between the shear and unshear directions. We find that the pebble game detects a slightly higher rigid fraction at high z, possibly due to boundary effects. This system-scale correspondence carries over to the contact level (Fig. 3.2b), where we compute the adjusted Rand index (ARI) [97, 98] to measure the bond-scale similarity of the detected clusters/regions. We find ARI > 0 (correlation is present), with an average of 0.6 indicating strong positive correlation and some differences again apparent at higher z. This robust high degree of correspondence is significant since the rigid cluster method requires only information about the contact graph (it is simply a *topological* measure), in contrast to the explicit displacement computation in the dynamical matrix, which contains the full spatial information. The correspondence is not exact, and there are specific (known, but rare) configurations where the two approaches give different results [75]. In Fig. 3.2c, we observe that the rigid cluster/region fractions both indicate a continuous rigidity transition, and agree with each other within error bars. Using the probability of a spanning rigid cluster (inset), we measure the transition point of $z_c = 2.4 \pm 0.1$. Fig. 3.2d shows that the rigid cluster size distribution broadens with increasing z. While our data is limited by finite system size and finite statistics, our distributions do not have a gap, and strongly resemble the results found in simulations of frictional disks [26]. These findings are consistent with a continuous rigidity percolation transition at a value of

$z_c < 3$, the mean-field Maxwell criterion with friction, and also with the mechanism of shear jamming. Note that in all of our analyses, we do not remove rattlers, as they are an integral part of the coexisting floppy and rigid regions and can become part of the packing at some point during the shear.

3.5 Discussion

We have investigated the network structure of real, frictional granular materials under shear using two distinct, but compatible, measures of rigidity. We find a frictional jamming transition at $z_c = 2.4 \pm 0.1$, significantly below $z = 3$, the lower bound on stable frictional packings given by mean-field constraint counting and also known as random loose packing [99]. Within the constraints of small system size and limited statistics, we observe a rigid cluster size distribution consistent with a continuous rigidity transition. Our z_c is also lower than simulation results by [90] who observed a rigid spanning cluster at $z_c \approx 2.9$ and the percolation of over-constrained bonds at $z = 3$. Finally, our experimental results contrast with simulations modeling friction with rough, but frictionless particles, for which the transition occurs at the isostatic point [100, 101].

Open questions include what role the mechanics of these rigid structures plays in local failure under shear. While strong force chains often surround a floppy hole with an arch-like shape, we observed only partial correlation with pressure: not all forces within floppy regions are weak. Our results need to be complemented with observations of force chains [102, 103, 104] and cycles [105] to more completely address rigidity in their descriptions. This could be done through topological [106], geometrical [107], or stress-space approaches [108]. Identifying rigid structures will also be important for shear-thickening in dense granular suspensions, where a load bearing rigid cluster abruptly emerges via the exchange of frictionless, lubricated contacts for frictional contacts [109, 110]. Our method provides a framework to go beyond mean-field in particulate systems, to ultimately understand the delicate interplay between constraints, forces, and geometry.

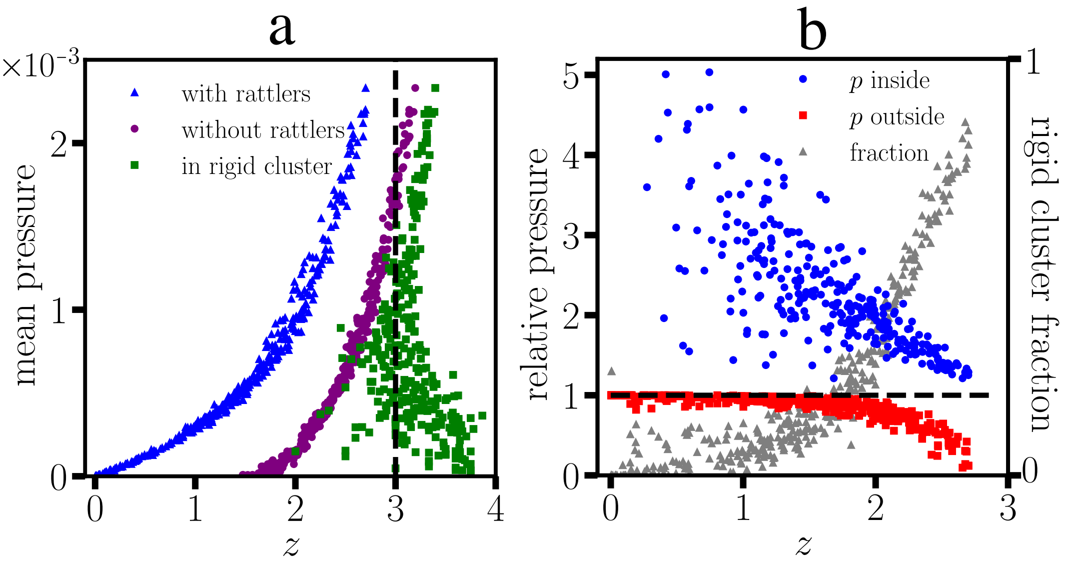

FIGURE 3.3: (a) Mean pressure p as a function of z of the entire packing (blue), within rigid clusters only (green), and with rattlers removed (purple). (b) Pressure inside rigid clusters (blue dots) and outside rigid clusters (red squares) normalized by the mean pressure of the entire packing. The fraction of rigid clusters (grey triangles) is also plotted for reference.

To show that the rigid clusters are mechanically relevant, we calculate the virial pressure p from the contact forces (see Appendix 3.D.2). In Fig. 3.3a, we show $p(z)$, rattlers included: the blue curve rises gradually but z remains well below 3. For comparison, we also include the same data but with the rattlers removed, as is commonly plotted [23]; this curve now crosses $z = 3$. In contrast, when (p, z) are calculated using only bonds within the rigid clusters, we observe that $z \geq 3$ except in some very small clusters. In Fig. 3.3b, we compute the local pressure inside vs. outside the rigid clusters, normalized by p for the entire packing. We find that pressure within rigid clusters is always significantly higher than the mean pressure. In contrast, the pressure in the floppy regions is always below average and drops further for $z > 2$, while the mean pressure, the rigid cluster fraction, and the rigid region fraction all start to rise. We interpret Fig. 3.3 as an emerging rigid backbone, responsible for the rise in pressure and carrying the majority of stress; this same mechanism was previously observed in simulations [26].

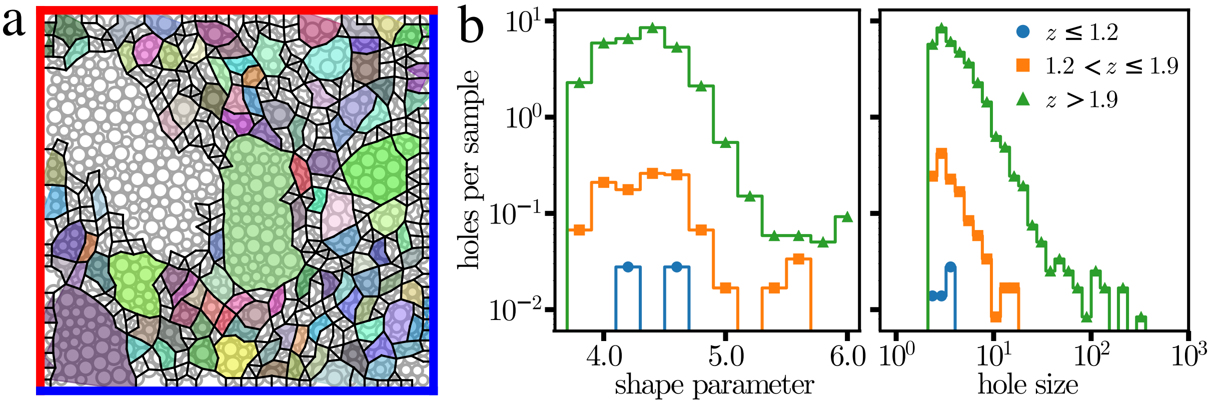

FIGURE 3.4: (a) Rigid clusters (black bonds) decomposed into tiles of closed loops; most colored tiles with $h > 2$ contain non-rigid particles; $z = 2.69$. (b) Histogram of hole sizes, in units of average particle area and histogram of hole shapes.

In Fig. 3.1d, rigid clusters surround large *holes* that contain floppy bonds and rattler particles. To characterize these floppy holes, we decompose the rigid cluster graph into a unique set of tiles, of which the larger ones correspond to the holes. Each tile corresponds to a face of the planar graph where the rigid bonds are the edges connecting vertices at the particle centers. To examine hole statistics, we employ a simple cutoff in hole size $h > 2$, in units of mean particle area, to exclude (most) simple interstices between particles; the remaining tiles are colored in Fig. 3.4a. Detail of floppy hole analysis is discussed in appendix 3.B.2 With increasing z, we observe both more and larger holes (Fig. 3.4b), with the system size as an apparent cutoff in hole size for $z > 1.9$. We quantify changes in shape using the dimensionless shape parameter $p_0 = P/\sqrt{A}$, where P is the hole perimeter and A is its area; a regular hexagon has $p_0 = 3.72$ and larger values indicate less circular due to convexity changes and/or elongation.

As z increases, we observe a broader range of shapes with some jaggedness emerging. Thus, the rigid structures resemble a sponge-like porous medium much like the interior of sourdough bread. This finding is compatible with the presence of arch structures, rigid bridges, and hinges linking up rigid clusters to form a spanning network [8], and contrasts with the rigidity transition in frictionless packings, where such floppy holes are not observed [87].

Appendix 3.A Robustness of contact identifications

Any analysis of a contact network depends crucially on having an accurate determination of whether or not two particles are in contact. Here, we describe how we (1) validated our contact detection and (2) estimated uncertainties for measurements of the mean contact number z. Fig. 3.5 displays examples of under- and over-detection of contacts.

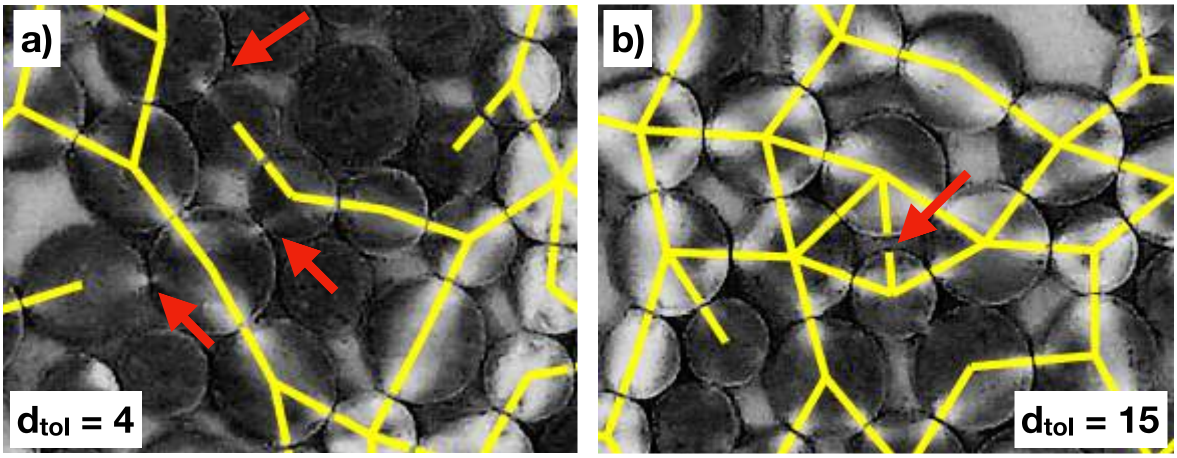

FIGURE 3.5: Example images showing the under- and over-detection of contacts, as a result of a (a) too-strict or (b) too-lenient detection threshold d_{tol}. Bright areas show a photoelastic response from the particles and yellow lines indicate identified contacts. False-negative and false-positive contacts are highlighted by red arrows.

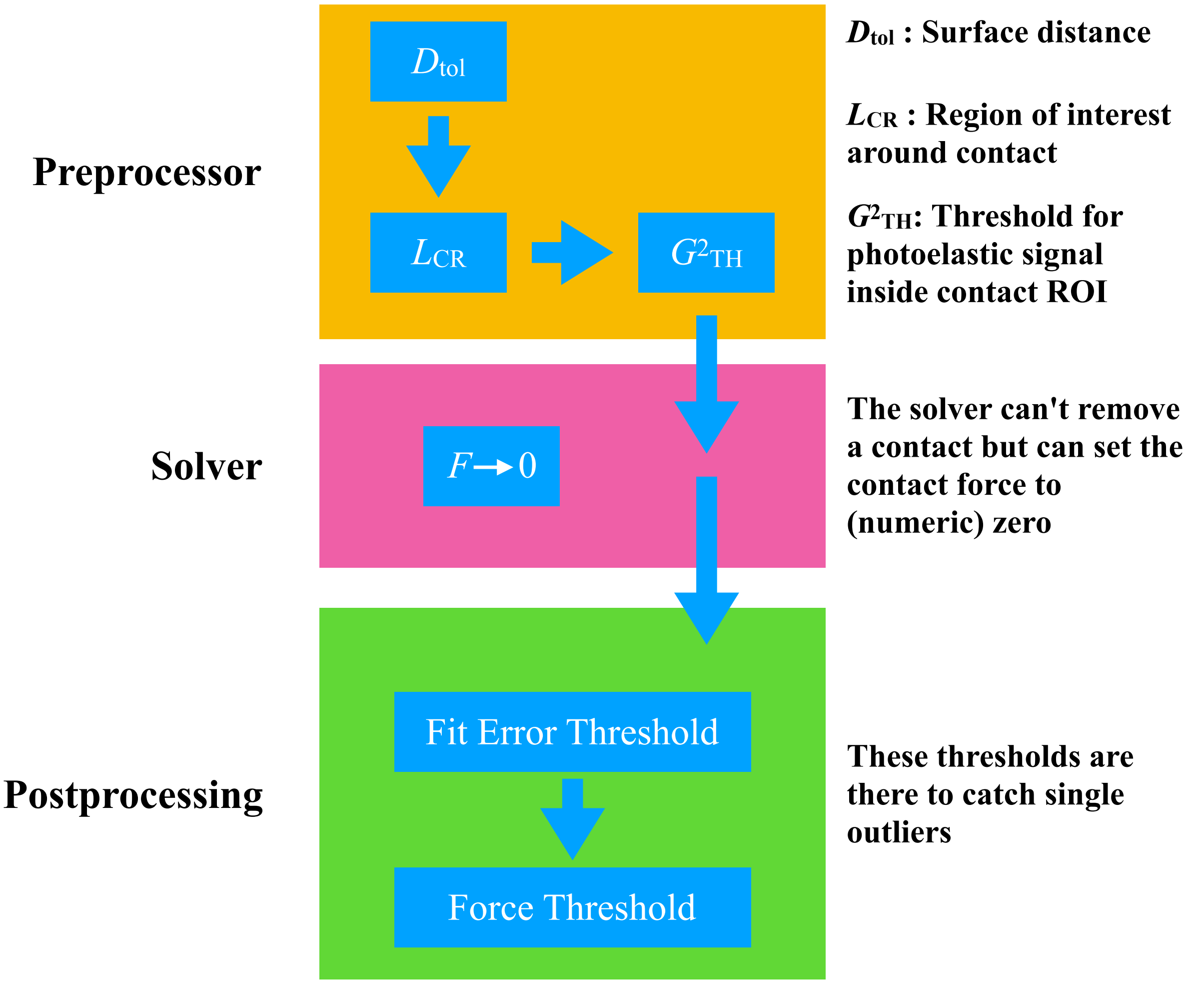

FIGURE 3.6: Contact processing pipeline.

3.A.1 Sensitivity to parameter choices

The open-source PeGS software package [96, 93] consists of three main parts, the preprocessor, the solver, and the postprocessor, as shown schematically in Fig. 3.6. Each of these parts influences what is counted as a *valid contact* in the paper's analyses.

The **preprocessor** detects the particle locations and radii using a Hough transform. As shown in Fig. 3.7, our resolution is 0.1 pixels, or approximately $R_1/200$, where R_1 is the radius of the smaller particles.

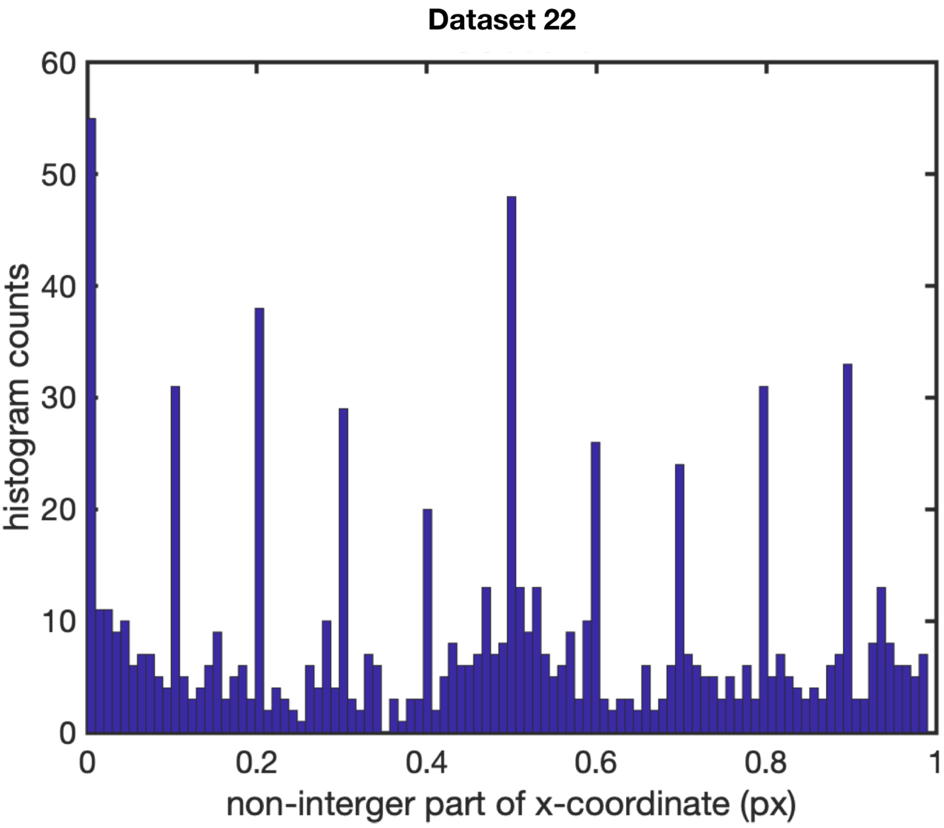

FIGURE 3.7: Histogram of noninteger parts of detected particle-coordinates show distinct peaks at intervals of 0.1 pixels. This value sets the precision of the center-detection of the particles.

For each possible pair of particles, we compute the surface distance as the difference between the measured distance between their centers and the sum of the two particle radii. If this difference is below a threshold d_{tol}, that pair of particles is considered to have a *possible contact*. The quantity d_{tol} is nonzero in order to account for uncertainty in the particle positions and radius detection, not just particle deformation during contacts. For each possible contact, we measure the G^2 (gradient-squared) response [93, 94] within a circular region of interest of radius L_{CR} pixels centered around the contact point. We set a threshold G^2_{th}, above which the contact is accepted into the list of contact points for the packing.

Note that inclusion on this list is a necessary, but not sufficient, condition for being ultimately counted as a valid contact. It is still possible that the solver/postprocessor later determines that a contact has a undetectable level of force, and is discarded from the list. In the text that follows, we use the following values which we found to be appropriate for this particular experiment (combination of particle material and geometry, apparatus, lens, and camera): $d_{\text{tol}} = 0.5R_1$, $G^2_{\text{th}} = 0.15$, and $L_{\text{CR}} = 0.25R_1$.

The **solver** takes the list of possible contacts provided by the preprocessor, and uses a model [96, 93] of the photoelastic response to determine, through optimization, the vector contact force at each contact. For every contact on the list, the solver also returns the residual e between the fit result and the experimental data. A smaller value of e indicates a higher-quality of the fit, to be evaluated during the post processing step (below).

The **postprocessor** creates the final list of valid contacts and forces in the form of an adjacency matrix. To be excluded from this list, two de-selection criteria apply:

1. Force fit quality: if the residual $e > e_{\max}$, all forces from this particle are set to zero, effectively removing the contact from consideration. The value of $e_{\max}$ is set empirically to exclude obvious fit errors.

2. Force magnitude range: if the magnitude of the contact force falls outside a specified range $F_{\text{min}} < |F| < F_{\text{max}}$, then that contact force is set to zero, effectively removing the contact from consideration. Here, we set $F_{\text{min}} = 10^{-3}$ N and $F_{\text{max}} = 2$ N, where the lower limit corresponds to an undetectable force and the upper limit is the force at which we are no longer able to properly resolve the photoelastic fringes.

Setting these 3 values (e_{max}, F_{min}, F_{max}), requires tuning by looking at the images and the output under the particular lighting conditions used in that experiment. Through visual inspection between what the algorithm detects and what is visible in the camera image, we choose an acceptable set of values for each of these three parameters.

3.A.2 Robustness tests

To determine the uncertainty in our contact detection, we conducted a robustness test to examine the sensitivity of contact detection to the choice of each of the parameters describe above. We tested these sensitivities for the preprocessor and postprocessor steps in isolation, and then performed a combined test to evaluate the ability of the solver to recover from poor-quality preprocessor data. We performed these tests on images from two different initial particle configurations (named Dataset 22 and Dataset 26), each under three different states of shear stress, for a total of 6 evaluations.

Preprocessing: For each of the 6 representative images, we varied one of the three parameters $d_{\text{tol}}, G^2_{\text{th}}, L_{\text{CR}}$, while fixing the other two to their default values, and measured the average contact number z after completing only the preprocessor step. The results are shown in Fig. 3.8.

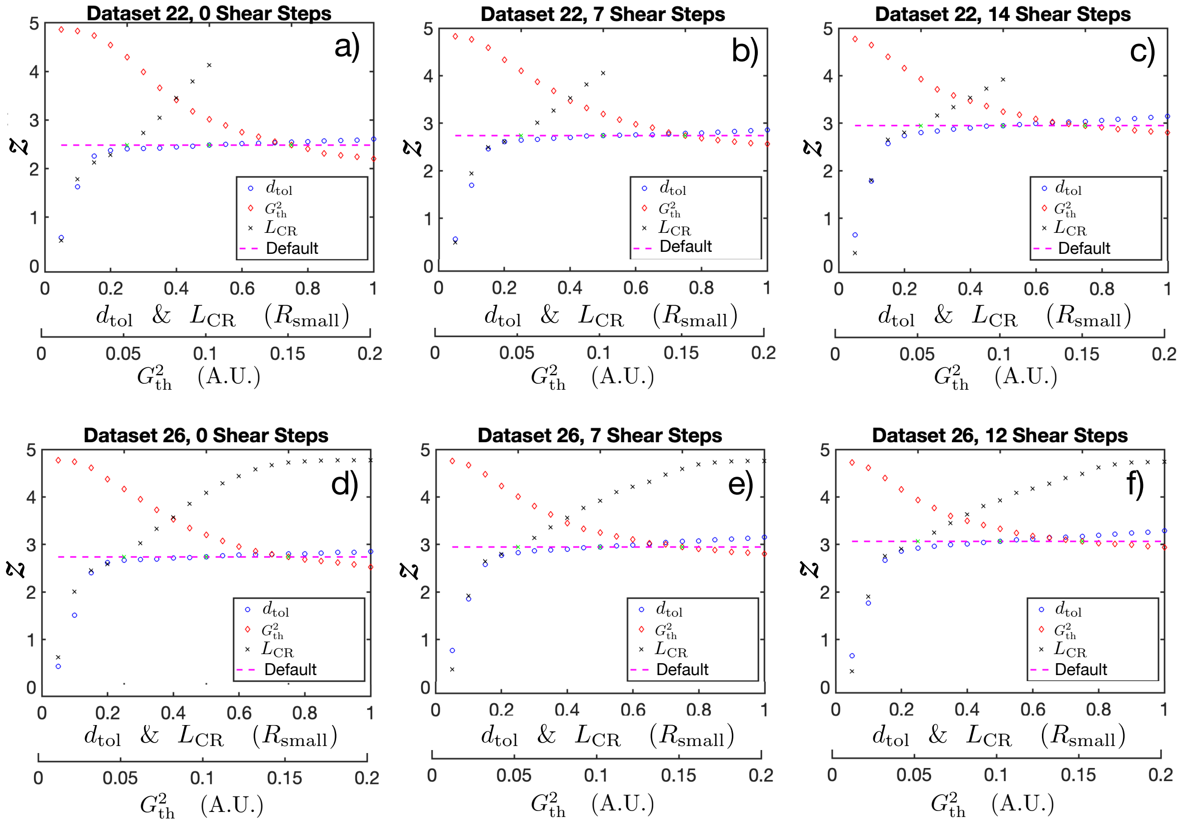

FIGURE 3.8: *Preprocessing robustness test:* The horizontal axis corresponds to varying $0.1R_1 \leq d_{\mathrm{tol}} \leq 1.0R_1$, $0 \leq G^2_{\mathrm{th}} \leq 0.2$ and $0.1R_1 \leq L_{\mathrm{CR}} \leq 1.0R_1$, where R_1 is the size of the small particles in the image, each varied independently (other parameters held at their default value). The dashed line is the result when all parameters are set at their default value.

We observe a strong dependence of the preprocessor-identified contacts on the user defined thresholds. For d_{tol} and G^2_{th}, there is a clear asymptotic value, while for L_{CR} there are images for which no sensible measurement is obtained for $L_{\mathrm{CR}} > 0.5\,R_1$ as the search area now strongly overlaps with other possible contact areas in the same particle. The solution is to allow for false-positives (larger value of L_{CR}), which will be removed at later steps.

At the start of a new photoelastic experiment, suitable ranges of values were found by running the preprocessor several times, adjusting each of the thresholds until the preprocessor-detected contact network visually matches the contact network seen in the photoelastic images. We found that L_{CR} is the most difficult threshold to set correctly, and was done by comparing the detection result to the photoelastic image, as in Fig. 3.5. *From these analyses, we select the values* $d_{\mathrm{tol}} = 0.5R_1$*,* $G^2_{\mathrm{th}} = 0.15$*, and* $L_{\mathrm{CR}} = 0.25R_1$*.*

Post processing: Using the possible contact lists generated during the preprocessor tests, we ran the photoelastic solver [93, 96], and performed the post processing steps by varying one of the three parameters (F_{min}, F_{max} and e_{max}) at a time, while fixing the other ones to their default value, and measured the resulting average contact number z.

As shown in Fig. 3.9, we observe that the mean contact number z does not change significantly with the choice of threshold, except for unrealistically low values of $e_{\mathrm{max}}, F_{\mathrm{max}}$). The aim in selecting F_{min} is to exclude contacts that the solver set to a zero value. As can be seen in Figs. 3.9 (a) and (d) there is little change to z for $F < 10^{-2}$ N so we set $F_{\mathrm{min}} = 10^{-3}$ N as our default value.

We observe that z decreases from 2.5 to 3.0 after preprocessing to 1.5 to 2.5 after post processing, depending on which of the 6 images is considered. The threshold rules,

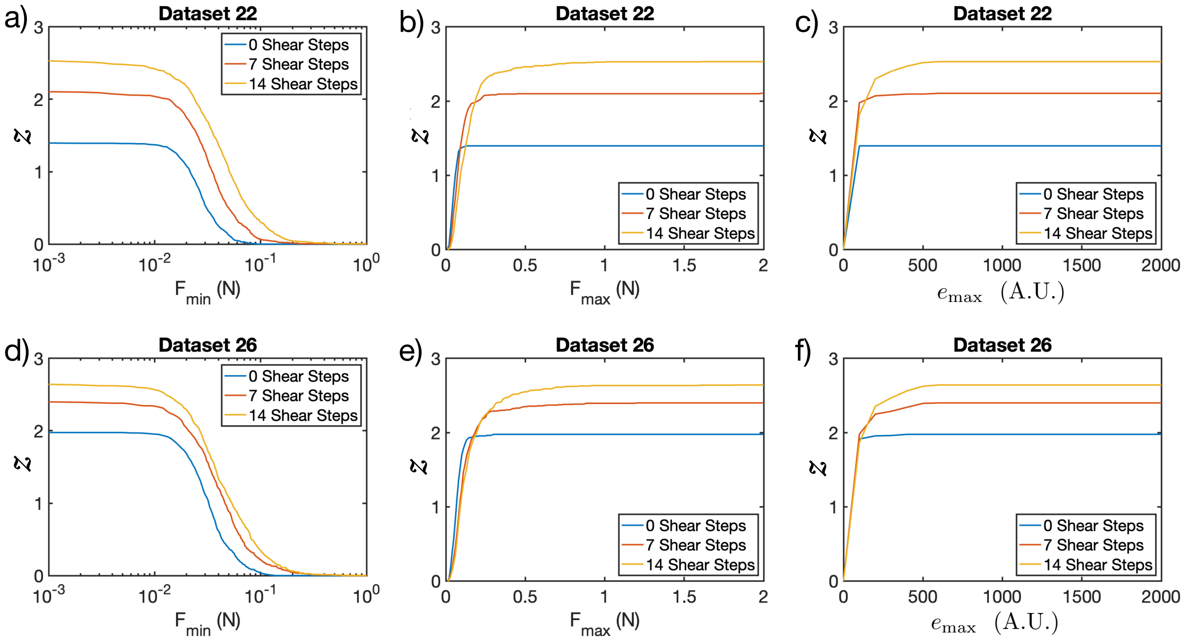

FIGURE 3.9: *Post processing robustness test:* The horizontal axis corresponds to varying $10^{-3}\,\mathrm{N} \leq F_{\min} \leq 1.0\,\mathrm{N}$, $10^{-2}\,\mathrm{N} \leq F_{\max} \leq 2.0\,\mathrm{N}$ and $0 \leq e_{\max} \leq 2000$, each varied independently (other parameters held at their default value). The different coloured lines correspond to different loads on the system.

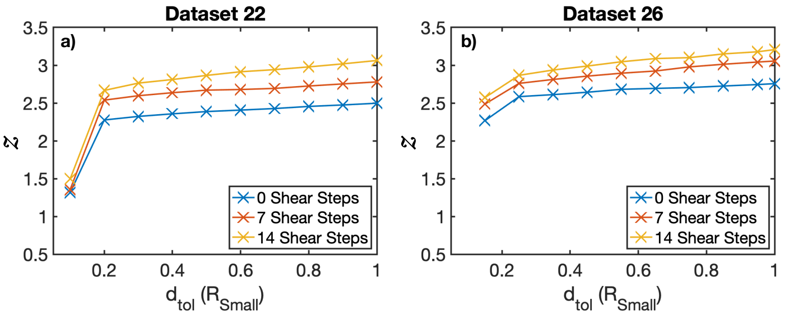

FIGURE 3.10: *Solver robustness test:* Measured z as a function of the choice of d_{tol} for the preprocessor; all other parameters are the default values. We estimate the uncertainty in z from the slope of $z(d_{\mathrm{tol}})$. The different coloured lines correspond to different loads on the system.

given above, required that only a reduction in the number of contacts is possible. *From these analyses, we set the values* $F_{\mathrm{min}} = 10^{-3}\,N$, $F_{\mathrm{max}} = 2\,N$, $e_{\mathrm{max}} = 2000$.

Solver: To determine the uncertainties in z, we examined the variability as a function of the entire data pipeline, including the solver, for variable values of d_{tol}. This tests the robustness of the process to the inclusion of false positives in the original contact list.

As shown in Fig. 3.10, for all 6 images there is only a slow dependence of z as a function of d_{tol} once a value of $d_{\mathrm{tol}} < 0.25R_1$ is surpassed. Above that value, there is a systematic error in z which is equally present in all datasets: the presence of false positives.

This result is consistent with visual observations, demonstrated by the two examples in Fig. 3.5. In comparing the full set, we observed an optimum at $d_{\mathrm{tol}} \sim 0.5R_1$. For $d_{\mathrm{tol}} < 0.25R_1$, the preprocessor missed obvious contacts (which cannot be recovered), and for $d_{\mathrm{tol}} > 0.75R_1$ it selected physically impossible contacts (some of which, but not all, were later trimmed by the postprocessor). Thus, it is better to err on the side of the largest d_{tol} that works for all datasets (see Fig. 3.8), and this is consistent with a choice of $d_{\mathrm{tol}} = 0.5R_1$. Our estimate of the uncertainty z is, therefore, half the change across a reasonable set of choices for d_{tol}, averaged over all 6 example images, which leads to an uncertainty in z of ± 0.1.

Appendix 3.B Rigid clusters: the pebble game

3.B.1 Pebble game algorithm

A rigid cluster is defined as the set of connected rigid bonds in a network that are mutually rigid with respect to each other. A rigid cluster with no redundant bonds is a minimally rigid cluster. Generically, a connected cluster (or network) with N vertices is minimally rigid in two dimensions if and only if it has $2N - 3$ bonds and no subcluster of n vertices has more than $2n - 3$ bonds, which is Laman's theorem [11]. This theorem is applicable to two-dimensional systems with central force constraints, such as bar-joint networks or frictionless packings described in terms of the contact network, with $2N$ denoting the number of degrees of freedom and 3 denoting the number of trivial, global zero modes, i.e. two translations and one rotation. The straightforward three-dimensional central-force extension of Laman's theorem does not rigorously hold [111]. However, mathematicians have been able to characterize the generic rigidity of rigid bodies connected by bars, i.e. body-bar rigidity, in arbitrary dimensions via a tight (k, k) network containing N vertices and M bonds such that every subset of $N' \leq N$ vertices connects with at most $kN' - l$ bonds and $M = kN - l$ [112].

The *(k,l) pebble game* [45, 113] provides a combinatorial algorithm for determining which bonds in a network are rigid, from which the rigid clusters can then be determined. The integer k represents the number of degrees of freedom for each particle, and the positive integer l represents the number of global degrees of freedom for the system. The original $(2, 3)$ pebble game by Jacobs and Hendrickson is applicable to frictionless packings [45] which have two translational degrees of freedom per particle, while the extension to general (k, l) was developed by Lee and Streinu [113] and is the one relevant to frictional packings [26]. We provide here a brief description of the algorithm:

Initially, k pebbles are "placed" on each vertex of the network (Fig. 3.11a). These vertices represent the *constraint network* defined by the contacts between the particles. To conduct the pebble game, there is an additional *directed network* constructed from the constraint network upon which the pebbles are moved around (Fig. 3.11b-e). As pebbles are moved around, two rules must be obeyed:

Rule 1 No more than k pebbles can be present on any vertex.

Rule 2 A directed bond is accepted into the directed network when at least a total of $l + 1$ pebbles are present at the two vertices defining the bond.

As each bond of the (undirected) constraint network is considered in turn, testing to see whether its associated bond is accepted into the directed network, the valid moves along are:

Move A A pebble found via a depth-first search starting a vertex x may be moved along the path with the arrows of the directed path reversed until reaching vertex x.

Move B If there is a directed bond is accepted into the directed network via Rule 2, then the found pebble is removed from the directed network.

The pebble game is played until all bonds in the constraint network have been considered. If, for example, there are more than l pebbles that have not been removed from the directed network, then the constraint network is floppy.

This algorithm ensures that the bonds accepted into the directed network map to independent constraints in the constraint network, so if there are l pebbles left over and bonds that have not been accepted into the directed network, then these correspond to redundant bonds. Note that such bonds are not necessarily unique since

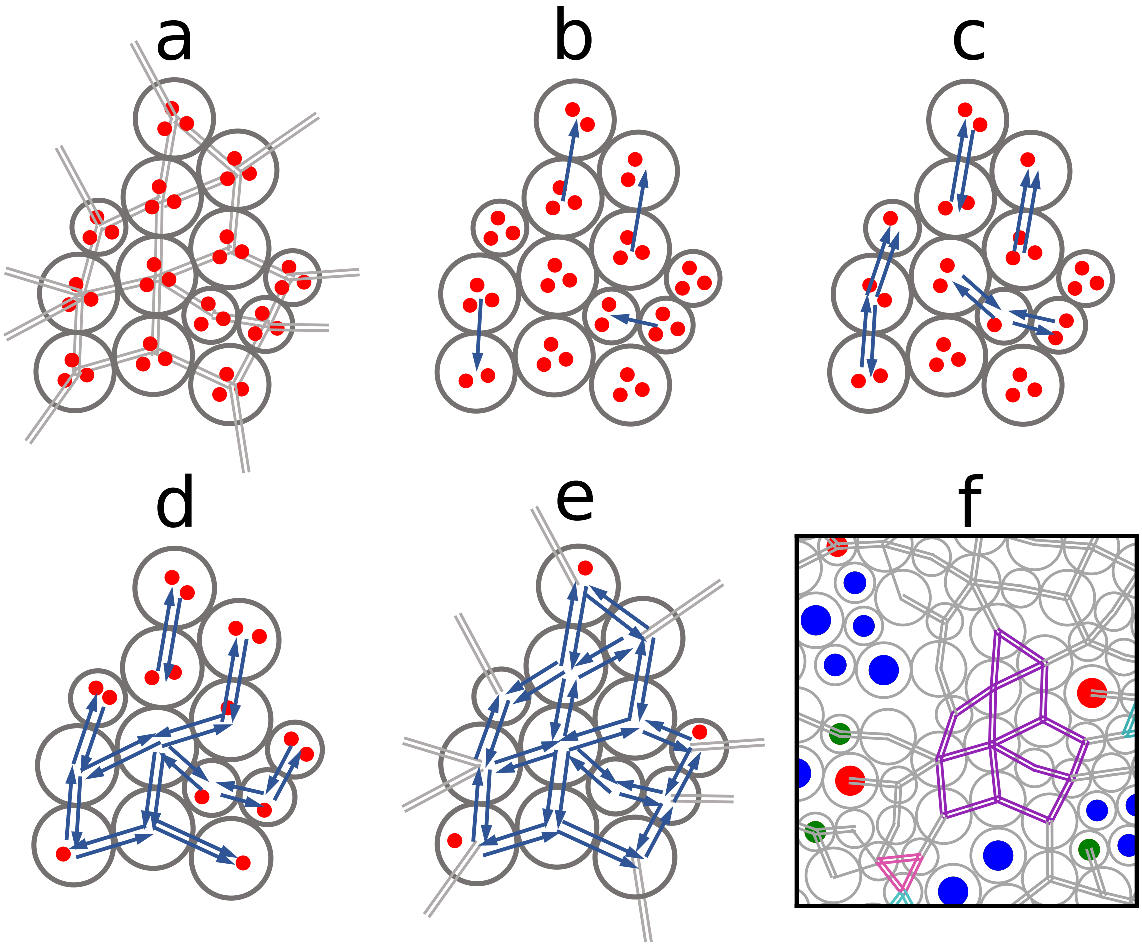

FIGURE 3.11: Implementation of the pebble game for a subset of a packing (a)-(e) and the corresponding rigid cluster (f).

they may change depending on the order in which the constraint network bonds are considered.

Now let us complete the application of the (k, l) pebble game to frictional packings. In such systems, the translational and rotational degrees of freedom must both be considered. For a 2D frictional granular system, we play a $k = 3$ pebble game, named for the two translational plus one rotational degree of freedom for each particle. The system itself has $l = 3$ global degrees of freedom (two translational plus one rotational).

In order to assign bonds for the correct number of independent constraints in the constraint network, it is necessary to ascertain whether each contact is below, or at, the Coulomb criterion. For frictional contacts (contacts below the Coulomb threshold), the normal and tangential components are independent and a double bond is assigned to the constraint network. For sliding contacts, the tangential and normal forces are no longer independent, and a single bond is assigned to the constraint network.

Once the constraint network is constructed, we then play the $(3,3)$ pebble game for that constraint network. This has been done for both frictional packings [26, 8] and rigid-beam [112] networks, with the double-bond structure having different meanings between the two cases. This is illustrated in Fig. 3.11. Note that there are specific gearing motions (even cycles) that are not correctly captured by the frictional $(3,3)$ pebble game [75]. As free gearing motions are only possible for systems without 3-cycles (particles in a triangle), they are vanishingly rare in disordered granular packings. We have therefore argued previously that near the frictional jamming transition, the algorithm is reasonably proficient [8]. This paper, in which we observe a very strong correlation with the rigid regions gives quantitative evidence of its suitability.

To account for boundaries in the experimental system, each of the 4 walls is treated as a boundary particle which has a bond with some of its neighboring particles. Since the boundary is not photoelastic, we determine which particles are in contact with it by examining all particles located less than $1.2R_1$ from the boundary. For each candidate particle, we accept it as a particle in contact with a boundary particle if the vector sum of its forces is non-zero, within a tolerance. We include an additional normal force between the candidate particle and the boundary particle so that the vector sum of the candidate particle is zero and then determine whether the contact is included as a single or double bond using the Coulomb criterion.

Once the constraint network is formed, we perform the $(3,3)$ pebble game on that set of bonds. Fig. 3.11 shows pictorially how the pebble game is implemented on a subset of an experimental packing with $\mu = 0.3$.

The pebble game for frictional packings is implemented in the *Pebbles* class of the rigid analysis python library [114].

3.B.2 Floppy hole analysis

To analyse the structure of the rigid cluster, we identify *floppy holes* containing rattler particles and floppy bonds in their interior. For example, the central hole in the rigid cluster of Fig. 3.12 contains 22 particles, of which 9 are outright rattlers (marked blue), while the other ones are connected to each other and to the rigid cluster by floppy bonds (marked grey). To automatically identify such holes, we need to identify the faces of the planar graph associated to the rigid cluster (in blue in Fig. 3.12a): the floppy holes simply correspond to the faces with a sufficiently large area to contain particles in their interior.

We construct a half-edge data structure by starting from a given bond and an orientation *from* particle i *to* particle j, and then moving counterclockwise by selecting the *next* bond from the bonds emanating from j that makes the largest angle with ij within the interval $(-\pi, \pi)$. Repeating this procedure moves counterclockwise around a face and will eventually close the loop by selecting ij as the *next* bond. Repeating this algorithm for all bonds and orientations that are not part of a face already allows us to identify the individual faces of the graph. When determining the faces, the effectively extended boundary particles are moved outward from the packing to avoid singular behaviour of the algorithm caused by intersecting contacts (i.e. a non-planar graph).

To identify the faces that correspond to floppy holes, we first compute the mean area per particle by dividing area of the system by the total number of particles, or $A_0 = \frac{L_x L_y}{N}$, where L_x and L_y are the lateral dimensions of the region. This will be the fundamental hole area unit. Then we compute hole area A for all faces using the formula for a non-intersecting planar polygon. Empirically, a hole with size A/A_0 smaller than 2 is not big enough to contain at least one particle in it, and we define floppy holes to be faces with $A/A_0 \geq 2$. The faces identified as floppy holes for the sample in Fig. 3.12a are shown in color in Fig. 3.12b, including the central hole in a muddy color.

When compiling the hole statistics as shown in Fig. **[fig:holes]**b, we normalise n_h such that the integral under each curve is equal to the mean number of holes per sample. We also compute the shape of the floppy holes using the dimensionless shape parameter $p_0 = P/\sqrt{A}$, where P is the floppy hole perimeter and A is its area. In Fig. **[fig:holes]**b, we also plot floppy holes per sample as a function of shape parameter for different z.

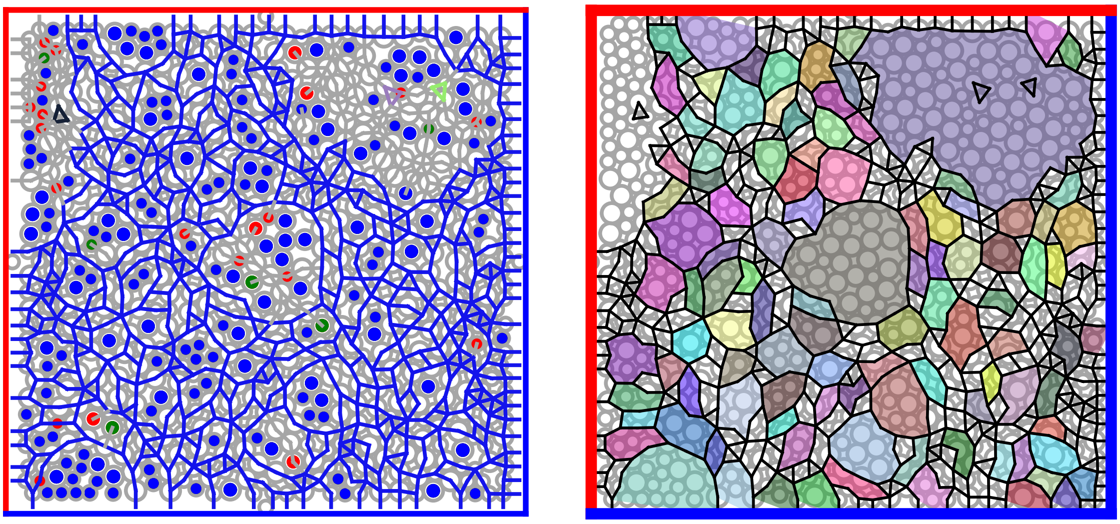

FIGURE 3.12: Rigid cluster plot and corresponding colored floppy hole decomposition of one sample with $z = 2.58$. The irregularly shaped floppy regions outside of the rigid cluster are topologically not holes within the rigid cluster and do not form part of the analysis.

Appendix 3.C Rigid regions: the dynamical matrix

3.C.1 Frictional equations of motion

We invoke the well-established Cundall-Strack model [115] as a reasonable model for the equations of motion for our frictional experimental system. This is the same model that was used to establish the frictional pebble game [26]. The equations of motion for individual particles are

$$\begin{aligned} m_i \ddot{\mathbf{r}}_i &= \mathbf{F}_i + \sum_{j\,n.\,i} \mathbf{F}_{ij} \\ I_i \ddot{\theta}_i &= T_i + \frac{1}{2} \sum_{j\,n.\,i} \mathbf{r}_{ij} \times \mathbf{F}_{ij}, \end{aligned}$$

where m_i is the mass of particle i and I_i is its moment of inertia, and the sums are over particles in direct contact. Here the first equation is for the forces, and the second is for the torques; we have made the approximation that force moments apply at the middle of the lever arm connecting particles.

The pair forces can be decomposed into three contributions:

1. The elastic central forces due to deformation of the cylindrical particles, $\mathbf{F}_{ij}^{el} = -K_n(R_i + R_j - |\mathbf{r}_{ij}|)\hat{\mathbf{n}}_{ij}$, where K_n is the (vertically integrated) Young's modulus of the particles. Note that such a *harmonic* force is appropriate for cylinders with a continuous contact line as in the experiment, while *Hertzian* forces are appropriate for a contact point.

2. The frictional forces between particles, which in a tangential frictional loading scenario can be written in a differential form $d\mathbf{F}_{ij}^{\mu} = K_t dt$, where dt is the tangential displacement (see below).

3. The viscous dissipative forces, which we assume are dominated by dissipation within the elastic material, and we estimate $\mathbf{F}^v_{ij} = -\zeta(\mathbf{v}_i - \mathbf{v}_j)$ for particles in contact, and 0 otherwise.

Finally, there are also some single-particle dissipative forces due to interaction with the air flow around the particles, which we roughly estimate as $\mathbf{F}^v_i = -\zeta_{\text{air}}\mathbf{v}_i$ and $T_i = -\zeta_{\text{air}} R_i \dot{\theta}_i$.

3.C.2 Effective potential for friction

In the limit of quasistatic deformations, the dissipative velocity-dependent terms will vanish, and the elastic and frictional forces will dominate. We therefore consider only the latter in our dynamical matrix approach. In the limit of small displacements (and only in this limit), we can recast the frictional forces as an effective potential. Consider the local geometry of a frictional contact shown in Figure 3.13.

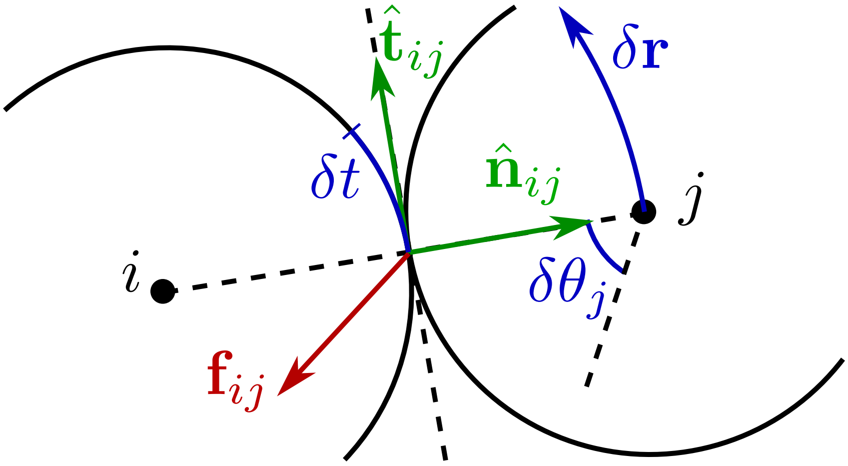

FIGURE 3.13: Local geometry around a frictional contact.

- Particle i at position $\mathbf{r}_i$ is joined to particle j at position $\mathbf{r}_j$ through the contact $\mathbf{r}_{ij} = \mathbf{r}_j - \mathbf{r}_i$.
- The normalised contact vector is the contact normal $\hat{\mathbf{n}} = \mathbf{r}_{ij}/|\mathbf{r}_{ij}|$.

- The tangential unit vector at the contact is $\hat{\mathbf{t}} = (n_y, -n_x)$
- The total force at the contact from j on i is $\mathbf{f} = -f_n\hat{\mathbf{n}} + f_t\hat{\mathbf{t}}$, where we have chosen $f_n > 0$, i.e. directed towards i.

Translations are parameterized by $\delta\mathbf{r} = \delta\mathbf{r}_j - \delta\mathbf{r}_i$, while rotations are initially parametrized by the two angular displacements $\delta\theta_i$ and $\delta\theta_j$. However, inspecting Fig. 3.13 reveals that the amount of tangential sliding *at* the contact is determined by both rotations and translations, which can be written as

$$\delta t = \delta\mathbf{r} \cdot \hat{\mathbf{t}} - (R_i\delta\theta_i + R_j\delta\theta_j). \tag{3.3}$$

To better understand this expression, here are two illustrative examples. First consider two equal-sized particles in a gearing motion. In this case, $\delta\theta_i = -\delta\theta_j$ and $\delta t = 0$. Second, consider now a purely tangential translation of particle j while i remains fixed, for which the tangential sliding is $\delta t = |\delta\mathbf{r}_j|$. In this second case, there must be a compensating gearing motion of the second particle, so that we again have $\delta t = 0$ if $R_j\delta\theta_j = |\delta\mathbf{r}_j|$.

We can now carefully consider the effect of a frictional force. In Figure 3.14, we schematically show the evolution of a representative frictional contact. At time 0, the contact is made by particles i and j coming sufficiently close. For simplicity, we will assume that f_n, the magnitude of the normal force, is approximately constant at short times; a reasonable assumption for a dense, slowly sheared packing. Upon contact, in phase 1 (tangential force loading), the increment in frictional force is given by $\delta f_t = K_t\delta dt$, where δdt is the the infinitesimal amount of frictional tangential loading. We can also directly write $f_t = K_t dt$, during this phase tangential motion is reversible.

In phase 2, the contact hits the Coulomb criterion $|f_t| = \mu f_n$, and then continues sliding, where for simplicity, we have assumed that the static and dynamic friction coefficients are the same. During phase 2, the tangential sliding coordinate dt continues to increase. In phase 3, the contact motion reverses, so that we again have $\delta f_t = K_t \delta dt$, and the frictional force falls below the Coulomb threshold. If the frictional force hits $f_t = -\mu f_n$, we enter phase 4 where the contact slides in the opposite direction and dt continues to decrease.

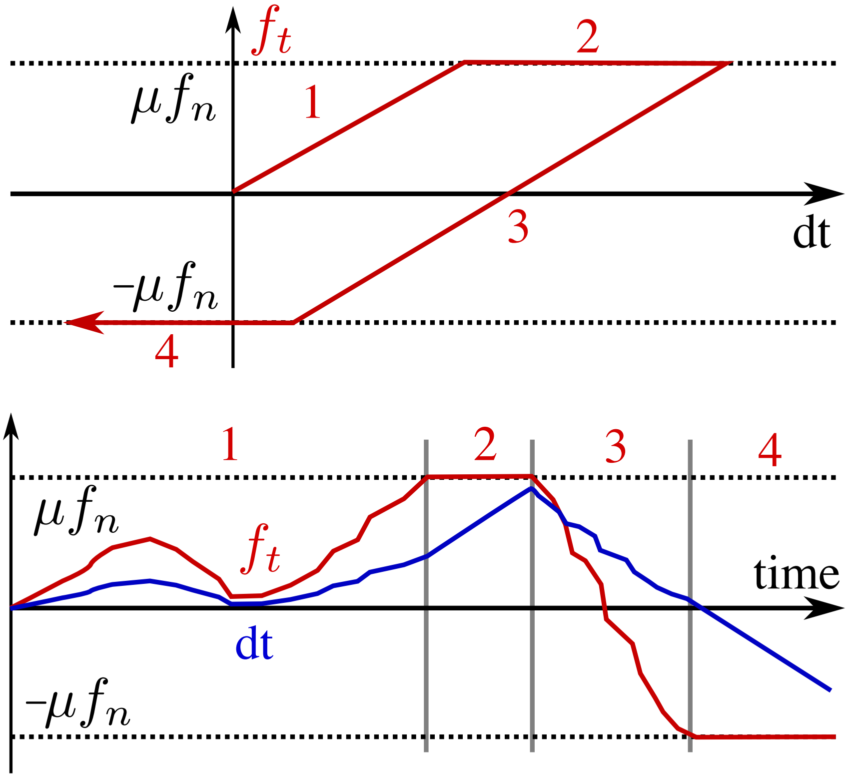

FIGURE 3.14: Schematic evolution of a frictional contact. Top: Magnitude of the frictional force as a function of tangential sliding coordinate. Bottom: Magnitude of the frictional force and amount of tangential sliding as a function of time.

We can write an effective potential in linear response for phases 1 and 3, if we neglect the likelihood of transitioning between phases during an infinitesimal displacement. The only complicated situation that potentially arises regularly is when a sliding contact reverses direction, i.e. during the transition from phase 2 to phase 3. As tested in our simulations of [26], for slowly sheared systems where the motion is primarily in a single direction, this occurs extremely rarely. This will, however, generate a major source of hysteresis when the shear is reversed. In our experiments, we do not take data at that instant of reversal, but only after the shear step has already occurred, putting us into phase 3 or 4.

During phase 1, we can write an effective potential

$$V_{\text{eff}}^{f} = \frac{1}{2} K_t dt^2. \tag{3.4}$$

We can see this by taking the explicit gradient of the potential in the local $\hat{\mathbf{n}}$, $\hat{\mathbf{t}}$ coordinate system, with coordinates $\delta n = \delta \mathbf{r} \cdot \hat{\mathbf{n}}$ and $\delta t = \delta \mathbf{r} \cdot \hat{\mathbf{t}}$. Note that dt is a scalar quantity, so despite $\hat{\mathbf{n}}$ and $\hat{\mathbf{t}}$ being a moving frame, the covariant derivative is the same as the ordinary derivative. Therefore, the effective potential remains valid for finite displacements and we have

$$\begin{aligned} \mathbf{F}_t &= -\nabla_{\mathbf{r}_i} V_{\text{eff}}^{f} = -K_t dt \nabla_{\mathbf{r}_i} dt \\ &= -K_t dt \left[\frac{\partial dt}{\partial \delta n} \hat{\mathbf{n}} + \frac{\partial dt}{\partial \delta t} \hat{\mathbf{t}} \right] = -K_t dt \hat{\mathbf{t}}. \end{aligned}$$

During phase 3, the same potential applies with a shift, $V_{\text{eff}}^{f} = \frac{1}{2} K_t (dt - dt_r)^2$, where dt_r is the tangential displacement at the moment of the transition between phases 2 and 3. During phases 2 and 4, the tangential force is a constant, and the effective potential is simply $V_{\text{eff}}^{f} = \pm \mu f_n dt$.

3.C.3 The dynamical matrix with friction

The dynamical matrix provides the equations of motion for a particle within its local potential, as has traditionally been done for analyzing the vibrational modes of crystals [116]. In the context of jammed systems [58, 117], rigid regions are constructed by locating all bonds for which the relative motion of the two connected particles falls below a threshold value, and is thereby treated as zero: that contact is said to be rigid. Even though frictional particles are governed by nonconservative forces, we can nonetheless calculate an effective dynamical matrix using our effective potential. Following the method that was only outlined in Refs. [62, 84], we begin by expanding the equations of motion for each particle i about its equilibrium position to obtain

$$\begin{aligned} \delta \ddot{r}^{i}_{\alpha\beta} &= -D^{ij}_{\alpha\beta} \delta r^{j}_{\beta} + \text{dissipation}(\delta \dot{r}) + O(\delta r^2), \\ D^{ij}_{\alpha,\beta} &= \frac{1}{\sqrt{m_{i,\alpha} m_{j,\beta}}} \frac{\partial^2 V_{ij}}{\partial r_{i,\alpha} \partial r_{j,\beta}}. \end{aligned} \tag{3.5}$$

Here $D^{ij}_{\alpha,\beta}$ is the dynamical matrix of the system, and the indices (i, j) label all disks, while (α, β) labels the two spatial x, y components and the angular component $\delta\theta$, and m denotes the particle mass or the moment of inertia depending on the type of component.

Using this framework of relative motions, we can then write the linearized interparticle potential around the contact as

$$V_{ij} = \frac{1}{2} \left[K_n (\delta \mathbf{r} \cdot \hat{\mathbf{n}})^2 - \frac{f_n}{|\mathbf{r}_{ij}|} \left(\delta \mathbf{r} \cdot \hat{\mathbf{t}} \right)^2 + \delta V^{f}_{\text{eff}} \right], \tag{3.6}$$

where the last term is the effective frictional potential rewritten for an infinitesimal displacement, $V^{f}_{\text{eff}} = K_t \delta t^2$ for phase 1 and 3, i.e. a loading contact (stick), and $V^{f}_{\text{eff}} = \pm \mu f_n \delta t$ for a sliding contact. The first term is simply the spring potential responsible for the elastic normal forces. The second (negative) term might seem counterintuitive: it comes from the existing normal force at the contact f_n, the so-called pre-stress term. A detailed derivation of the first two terms can be found in [101].

Fully written out in coordinates, the linearised equations of motion in the quasistatic regime (in the absence of damping) are

$$m_i \delta \ddot{\mathbf{r}}_i = -\sum_j \left[\frac{\partial^2 V_{ij}}{\partial \mathbf{r}_i \partial \mathbf{r}_j} \cdot \delta \mathbf{r}_j + \frac{\partial^2 V_{ij}}{\partial \mathbf{r}_i \partial (R_j \theta_j)} \delta(R_j \theta_j) \right],$$

$$\frac{I_i}{R_i^2} R_i \delta \ddot{\theta}_i = -\sum_j \left[\frac{\partial^2 V_{ij}}{\partial (R_i \theta_i) \partial \mathbf{r}_j} \cdot \delta \mathbf{r}_j + \frac{\partial^2 V_{ij}}{\partial (R_i \theta_i) \partial (R_j \theta_j)} \delta(R_j \theta_j) \right].$$

In the second equation we have used the particle radius R_i to give all coordinates the same dimensions of length. Since the moment of inertia for a cylinder about its central axis is $\frac{1}{2} m_i R_i^2$, the prefactor in the second equation is just $m_i/2$.

Based on these equations, we construct the dynamical matrix from its 3×3 i, j sub-elements between particles i, j where we are now using the notation $r_{i,\alpha} = (x_i, y_i, R_i \theta_i)$, and similarly $m_{i,\alpha} = (m_i, m_i, m_i/2)$. In simulations [62, 26], we previously set $m_i = 1$ for the spatial equations of motion, and even $I_i / R_i^2 = 1$, which corresponds to making the approximation that the particles are all roughly the same size, and are hollow cylinders. For this derivation, we will continue to carry the mass and inertia prefactors in order to arrive at a general result that can be used with experimental data.

We can now derive the 3×3 sub-element of the dynamical matrix. Since we have used a local coordinate system to define the local potential, we choose (without loss of generality) $\hat{\mathbf{x}} = \hat{\mathbf{n}}_{ij}$ and $\hat{\mathbf{y}} = \hat{\mathbf{t}}_{ij}$, so that we can write $\delta \mathbf{r} = (\delta x_j - \delta x_i, \delta y_j - \delta y_i)$. Later, we will have to rotate this back into a global frame of reference for the full matrix. In this local set of coordinates, the effective potential is

$$\begin{aligned}
V_{ij} &= \frac{1}{2}\left[K_n(\delta x_j - \delta x_i)^2 - \frac{f_n}{r_0}\left(\delta y_j - \delta y_i\right)^2 + \delta V_{\text{eff}}^{f}\right], \\
\delta V_{\text{eff}}^{f} &= K_t((\delta y_j - \delta y_i) - (R_i\delta\theta_i + R_j\delta\theta_j))^2 \quad \text{frictional}, \\
\delta V_{\text{eff}}^{f} &= \pm\mu f_n((\delta y_j - \delta y_i) - (R_i\delta\theta_i + R_j\delta\theta_j)) \quad \text{sliding}.
\end{aligned}$$

As we can readily see, all second derivatives of $\delta V_{\text{eff}}^{f}$ for sliding contacts are 0, so that *sliding contacts do not contribute to the dynamical matrix*. Practically, for sliding contacts, we set $K_t = 0$ in the equations below. Then off-diagonal elements of the dynamical matrix are given by

$$\hat{\mathbf{D}}^{ij} = \frac{1}{\sqrt{m_i m_j}}\begin{bmatrix} -K_n & 0 & 0 \\ 0 & -K_t + \frac{f_n}{r_0} & K_t/\sqrt{2} \\ 0 & -K_t/\sqrt{2} & K_t/2 \end{bmatrix}. \tag{3.7}$$

The contact ij also contributes to the ii element of the dynamical matrix, as moving particle i itself will also affect its force state. We have a contribution of (note sign changes):

$$\hat{\mathbf{D}}^{ii}_{\text{from}\, j} = \frac{1}{m_i}\begin{bmatrix} K_n & 0 & 0 \\ 0 & K_t - \frac{f_n}{r_0} & K_t/\sqrt{2} \\ 0 & K_t/\sqrt{2} & K_t/2 \end{bmatrix}. \tag{3.8}$$

We then perform rotation of these matrices into a general, global coordinate system, using the angle of the contact normal with the x-axis: $\hat{n}_{ij} = (n_x, n_y) = (\cos\phi, \sin\phi)$ and $\hat{t}_{ij} = (n_y, -n_x) = (\sin\phi, -\cos\phi)$.

Since the experimental data is in a form where each contact is single-counted only, this means we also need to use the information above to construct the ji contact, and add to the jj diagonal element. The derivation for these is identical, except for swapping the j and i labels, so in their local coordinates the results of Eq. 3.8 and Eq. 3.7 are identical.

However, more subtly, $\hat{\mathbf{n}}_{ji} = -\hat{\mathbf{n}}_{ij}$ and $\hat{\mathbf{t}}_{ji} = -\hat{\mathbf{t}}_{ij}$, while the axis of rotation in our coordinate system (z) is not affected. Since the nn, nt, tn and tt terms have two unit vector components, the signs cancel and nothing changes. For the $\alpha\alpha$ term, nothing changes. However, for the off-diagonal components $n\alpha$, αn, $t\alpha$ and αt, the sign *will* change. Then *if* we use the $\hat{\mathbf{n}}_{ij}$ and $\hat{\mathbf{t}}_{ij}$ as a basis for the flipped contacts as well, we have the following contributions:

$$\hat{\mathbf{D}}^{ij} = \frac{1}{\sqrt{m_i m_j}} \begin{bmatrix} -K_n & 0 & 0 \\ 0 & -K_t + \frac{f_n}{r_0} & -K_t/\sqrt{2} \\ 0 & K_t/\sqrt{2} & K_t/2 \end{bmatrix} \tag{3.9}$$

The contact ji also contributes to the self-element jj of the dynamical matrix and we have a contribution

$$\hat{\mathbf{D}}^{jj}_{\text{from } i} = \frac{1}{m_j} \begin{bmatrix} K_n & 0 & 0 \\ 0 & K_t - \frac{f_n}{r_0} & -K_t/\sqrt{2} \\ 0 & -K_t/\sqrt{2} & K_t/2 \end{bmatrix} \tag{3.10}$$

The dynamical matrix for frictional packings is implemented in the *Hessian* class of the rigid analysis python library [114].

3.C.4 Mapping out rigid regions

Now that we have constructed the dynamical matrix, we can compute all its eigenvalues and eigenvectors accordingly. In Fig. 3.15, we show distributions of computed eigenvalues for four samples with a range of z. From each plot we observe two peaks

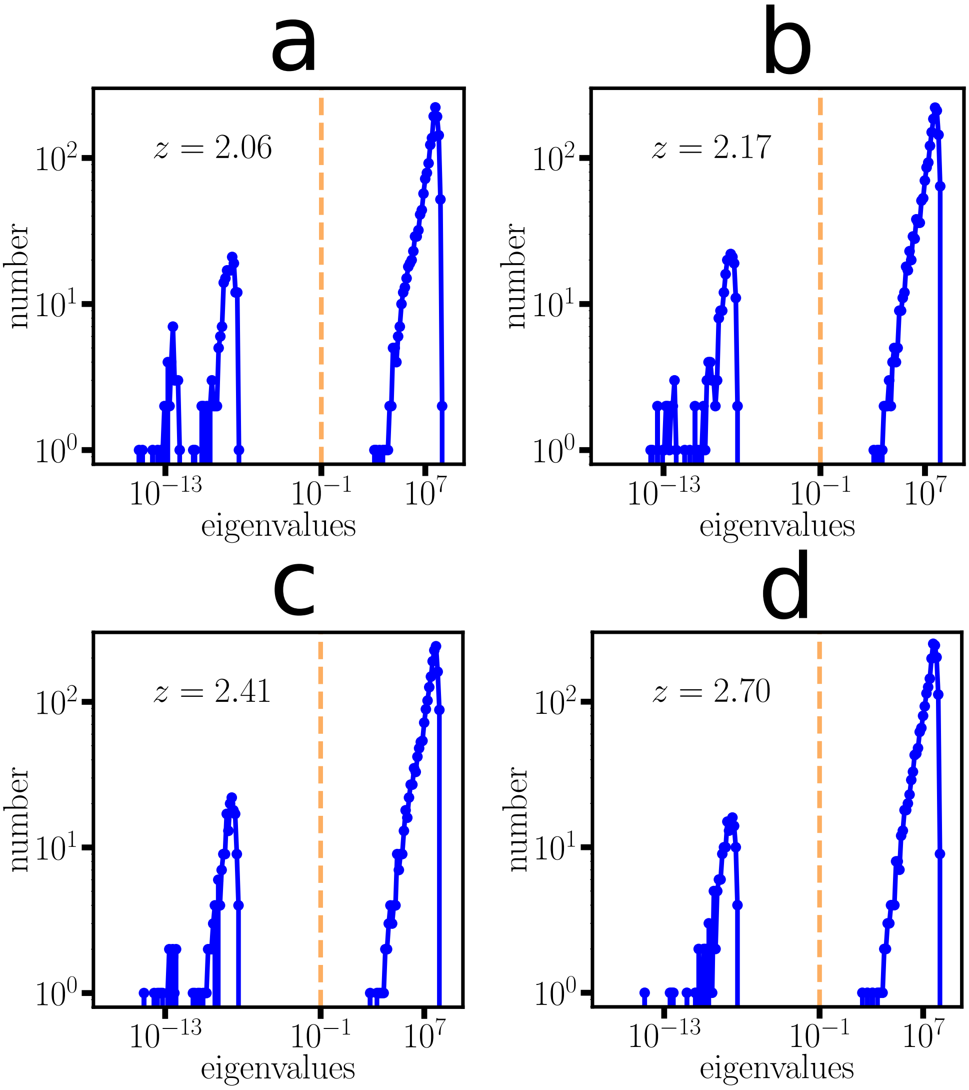

FIGURE 3.15: Distribution of eigenvalues for four different samples with average coordination number shown in figures.

at approximately 10^{-8} and 10^{7} and a wide gap between them. We, therefore, treat eigenvalues below 10^{-1} as zeros with their corresponding eigenvectors representing zero modes labeled as $(\mathbf{r}_{i,k}, \theta_{i,k})$ where i labels different particles and k labels different zero modes. From all N_{zero} zero modes we compute the relative translational and rotational displacements between particles i, j using

$$\delta r^2_{i,j,\text{trans}} = \frac{1}{N_{\text{zero}}} \sum_k \left[((\mathbf{r}_{j,k} - \mathbf{r}_{i,k}) \cdot \hat{\mathbf{n}})^2 + ((\mathbf{r}_{j,k} - \mathbf{r}_{i,k}) \cdot \hat{\mathbf{t}})^2 \right] \tag{3.11}$$

$$\delta \theta^2_{ij,\text{rot}} = \frac{1}{N_{\text{zero}}} \sum_k \left(\theta_{i,k} + \theta_{j,k} \right)^2 . \tag{3.12}$$

In Fig. 3.16, we plot distributions of $\delta r^2_{i,j,\text{trans}}$ and $\delta \theta^2_{ij,\text{rot}}$ respectively for all contacts and observe two peaks in relative translational displacements. Based on this, we select an appropriate rigidity threshold τ such that any relative motion below that value is treated as zero. These are considered rigid and form the rigid regions shown in Fig. 3.17. The sensitivity of our results to this threshold choice is discussed in an upcoming section.

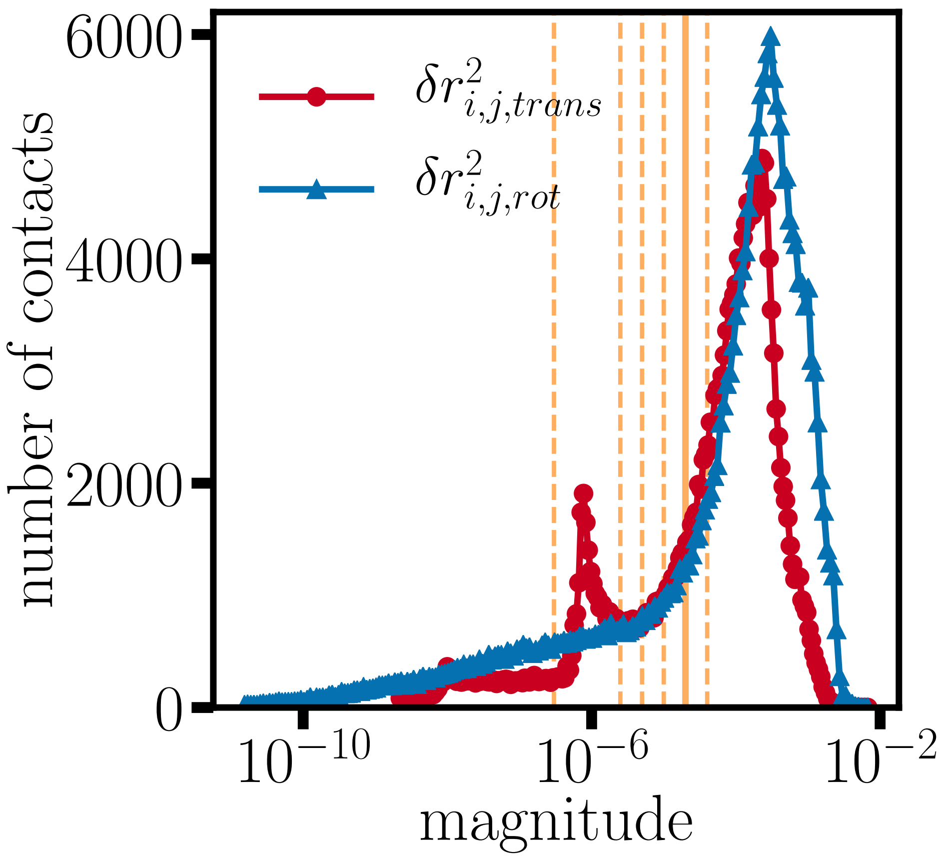

FIGURE 3.16: A semi-log plot of the distribution of all relative translational displacements (red) and rotational displacements (blue) between all pairs of particles for all samples, as a function of displacement magnitude, increasing exponentially from left to right. From left to right,the six orange lines label six rigidity thresholds, 3×10^{-7}, 2.5×10^{-6}, 5×10^{-6}, 1×10^{-5}, 2×10^{-5}, 4×10^{-5}. Contacts on the right side are treated as floppy and contacts on the left side are rigid. The solid line is the threshold used in main text.

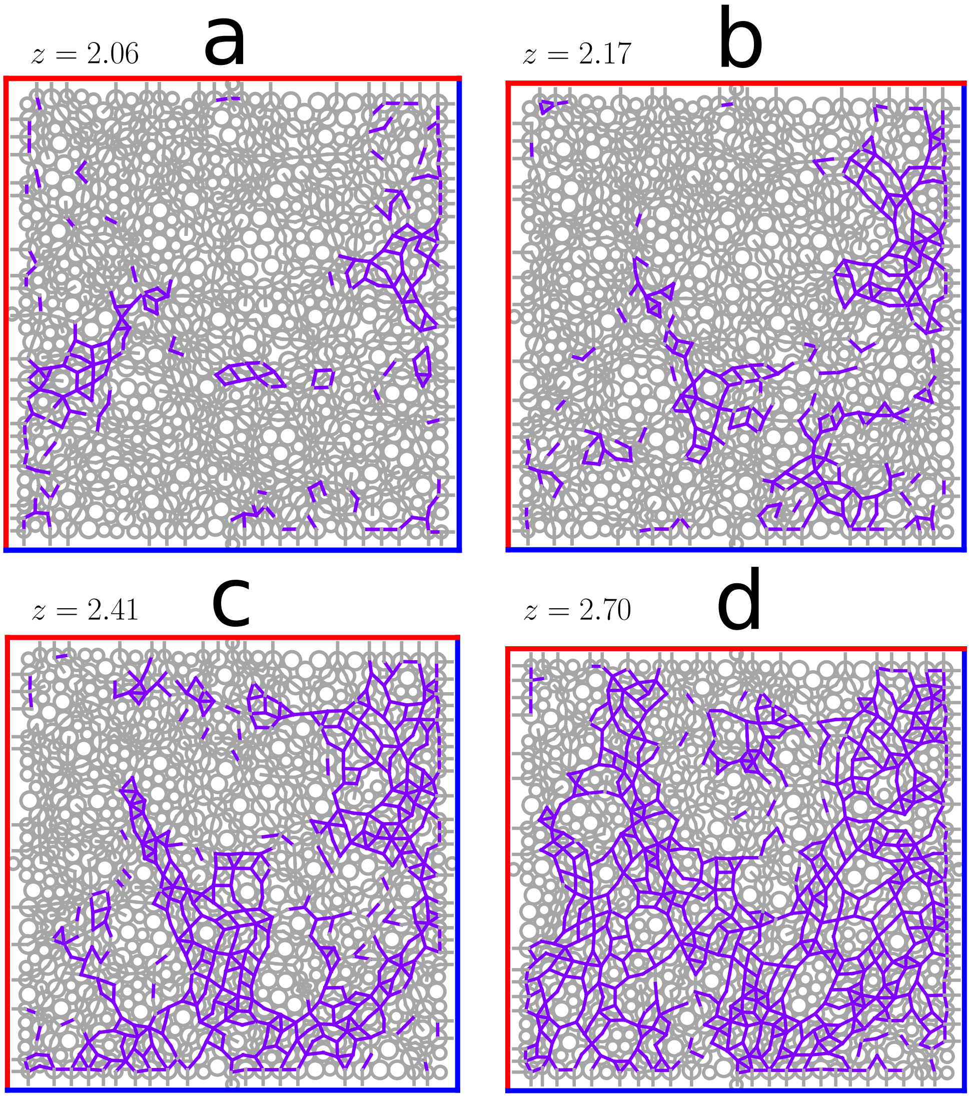

FIGURE 3.17: Representative identification of rigid regions for the same four samples in Fig. 3.15, using the dynamical matrix and rigidity threshold set to 2×10^{-5}. Purple contacts are in rigid regions under both translational and rotational considerations; grey contacts are floppy.

Appendix 3.D Determination of parameters

3.D.1 Particle parameters

To compute particle masses, we note that the Vishay particles are disk-shaped and have a density of $\rho = 1.06\,\mathrm{g/cm}^3$. For particle radii corresponding to $R_1 = 5.5$ mm and $R_2 = 7.6$ mm, and for a thickness $h = 3.1$ mm, the particle masses are then $m_1 = 3.12 \times 10^{-4}$kg, and $m_2 = 5.96 \times 10^{-4}$kg. The raw data from images are measured in pixels, with radii $R_1 = 20$ and $R_2 = 29$ pixels, and we can therefore deduce a global conversion factor of $c = 2.7 \times 10^{-4}$ m/pixels.

To estimate the stiffness coefficients, we read off the dynamical matrix equations that their units are acceleration per length, i.e. $[K_n] = [M][T^{-2}]$. Using Hertzian contact theory [118], for two cylinders with parallel axes, the force is given approximatively by $F = \frac{\pi}{4}E^*hd$, where d is the indentation depth (overlap), and E^* is the scaled Young's modulus,

$$\frac{1}{E^*} = \frac{1-\nu_1^2}{E_1} + \frac{1-\nu_2^2}{E_2}, \tag{3.13}$$

where E_i and ν_i are Young's moduli and the Poisson ratios of the two materials, respectively. If we assume that $\nu_1 = \nu_2 = 0.5$ (i.e., an incompressible material), and set $E_1 = E_2 = E$, we find $E^* = \frac{2}{3}E$. Finally, we obtain $K_n = \frac{\pi}{6}Eh$. For an order of magnitude estimate, the Young's modulus of Vishay is $E \approx 4\,\mathrm{MPa}$, and since $[E] = [M][T^{-2}][L^{-1}]$, our units are correct. For interactions between two particles, the stiffness coefficient of the harmonic elastic interaction related to normal forces is therefore $K_n = 6490\ \mathrm{kg}\cdot\mathrm{s}^{-2}$. For simplicity, we will assume that we have a Cundall-Strack-like relation for tangential motion, so that $K_t = K_n$.

The boundary of the system is significantly larger and heavier than a single particle, so that both the mass m_b and the moment of inertia I_b are much larger. Using a rough order of magnitude estimate of boundary size and shape, we arrive at

$m_b \approx 10^2(m_1 + m_2)/2$ and $I_b \approx 10^4(I_1 + I_2)/2$. Therefore, the terms in the dynamical matrix corresponding to the particle-boundary and boundary-boundary interactions will be very small, and the corresponding displacements in the normal modes are also tiny. Compared to a system without boundaries, this softly enforces the constraint of an immovable boundary. For contacts between particles p and a wall w made of dissimilar materials with Young's moduli E_p and E_b and Poisson ratios ν_p and ν_w, the effect modulus that enters the stiffness coefficient or a particle-wall contact is $\frac{1}{E^*_{pw}} = \frac{1-\nu_p^2}{E_p} + \frac{1-\nu_w^2}{E_w}$. For wall stiffness E_w lying between E_p and infinity, we obtain $E^*_{pw} = 1.0E^*_{pp} - 2.0E^*_{pp}$, in practice the wall is significantly stiffer than the particles. In the dynamical matrix, we use the same K_n and K_t for particle-boundary contacts as for particle-particle contacts.

In both methods, the pebble game and the dynamical matrix, identifying whether a contact is sliding is essential and we therefore need an estimate for the friction coefficient μ. In Fig. 3.18 we plot the probability distribution of the ratio of tangential forces to the corresponding normal forces, or *mobilisation*. While we do not see an accumulation of probability near the Coulomb threshold as in some simulated packings [82], this figure suggests that the friction coefficient is approximately $\mu = 0.3$ since the probability drops below 10^{-2} around a ratio of 0.3. With these parameters, on average 5.2% of all contacts are sliding contacts. Below, we test how our numerical methods are affected by the choice of friction coefficient.

3.D.2 Pressure calculation

The pressure on a given particle i due to its contact forces with particles j is derived from the virial part of the Irving-Kirkwood stress tensor [119],

$$\hat{\textbf{œ}}_i = \frac{1}{A_i} \sum_j \mathbf{r}_{ij} \otimes \mathbf{F}_{ij}, \tag{3.14}$$

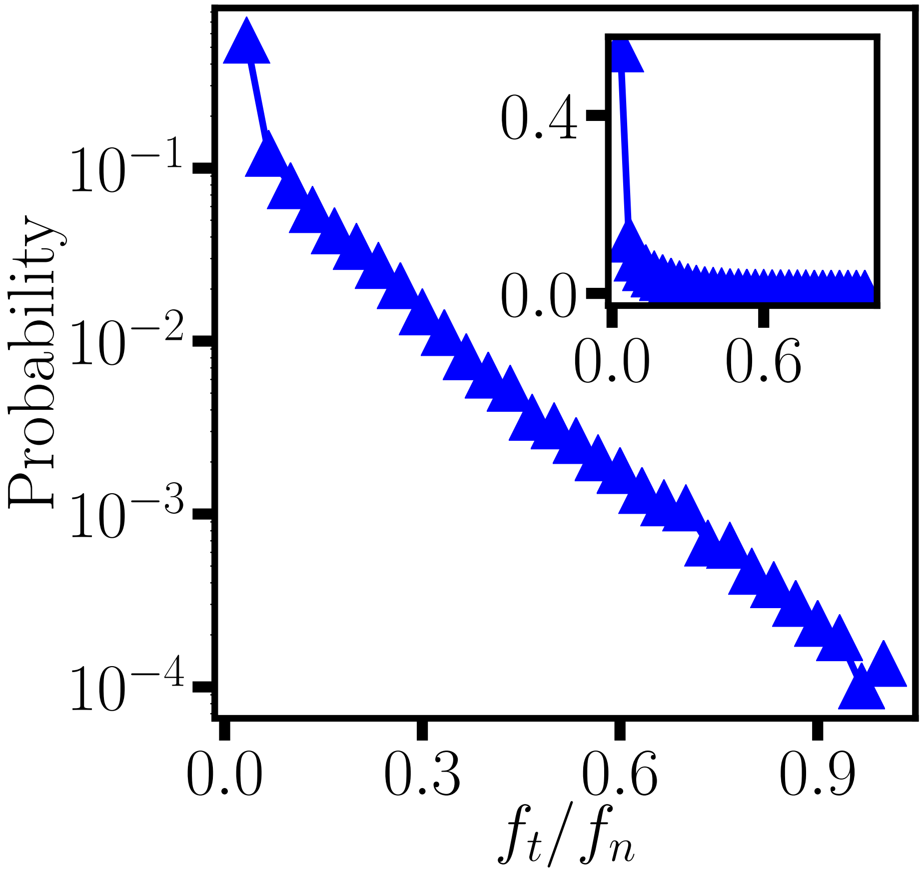

FIGURE 3.18: Semi-log plot of the probability distribution of f_t/f_n from all packings. Inset: same, on a linear axis scale.

where A_i is the area (in two dimensions) of the plane associated to particle i in a tessellation so that $\sum_i A_i = A$, the total system size. This is to ensure that the stress is an intensive quantity. With f^n_{ij} denoting the normal force between particle i and j, the local pressure on particle i, i.e. the trace of the stress tensor, is then given $p_i = \frac{1}{A_i}\sum_j f^n_{ij} r_{ij}$, where A_i is the area possessed by particle i after Voronoi tessellation. When considering every particle i in rigid cluster and its neighbor j, we then obtain the pressure within the rigid cluster as $p_{\text{in}} = \frac{\sum_i \sum_j f^n_{ij} r_{ij}}{\sum_i A_i}$. Note that a particle is in the rigid cluster if any one bond connected to it is identified as a rigid bond. Similarly, we can compute the pressure outside the rigid cluster.

3.D.3 Sensitivity to parameter choice: μ, τ

Since the decomposition of rigid clusters and the construction of dynamical matrix depend on the choice of both the friction coefficient μ and the rigidity threshold τ (for the dynamical matrix only), we need to test to what extent our results depend on those parameters. Here, we put our choice of $\mu = 0.3$ and $\tau = 2 \times 10^{-5}$ (corresponding to Fig.2a-c in the main paper) into context. We vary τ from 3×10^{-7} to 4×10^{-5}, corresponding to the cutoffs in the displacement magnitude indicated in Fig. 3.16. We also test the dependence on the friction coefficient by performing the analysis with $\mu = 0.2$ instead of $\mu = 0.3$.

In Fig. 3.19, we plot the same analysis as that presented in Fig.2a-c in the main text for each set of parameters. At the extreme end, for $\tau = 3 \times 10^{-7}$ i.e. a threshold to the left of both peaks in Fig. 3.16, we see that the fraction of rigid region decreases substantially due to the rigidity threshold being too small and the correlation between two methods at higher z disappears. However, above this threshold in τ, we observe that the correlation between the rigid clusters and the rigid regions is robust to changes in τ parameter space corresponding to the "valley" in relative translational displacement distribution shown in Fig. 3.16.

For the lower friction coefficient $\mu = 0.2$, both the rigid region fraction and rigid cluster fraction are decreased compared to $\mu = 0.3$, which can be explained by the fact that the Coulomb threshold is lower, leading to more fully mobilized sliding contacts and so more motion is allowed in both methods. The correlations between both measures remains robust however, as can be seen in the graph of the Adjusted Rand Index (see §3.E).

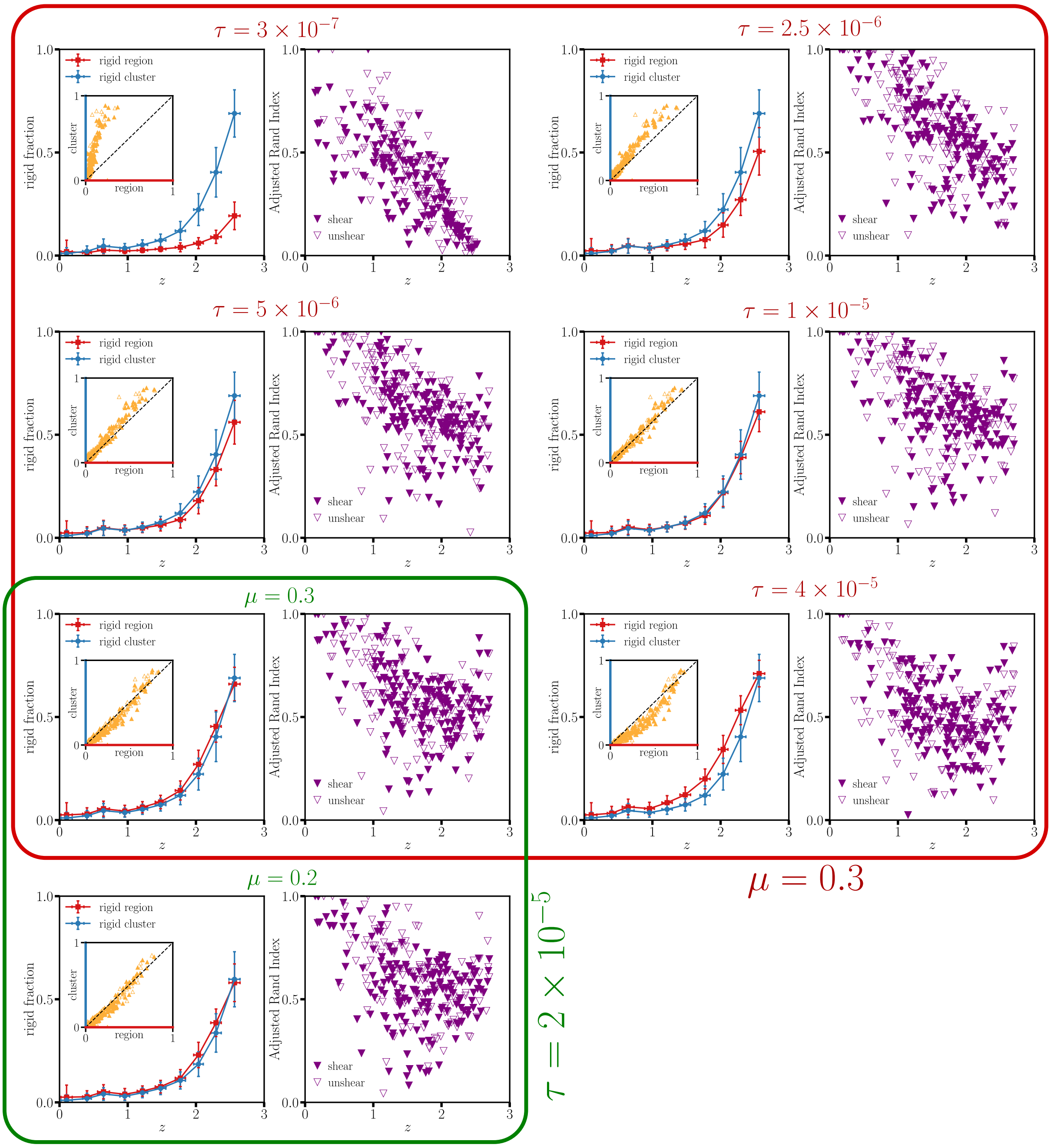

FIGURE 3.19: Robustness of the rigid cluster decomposition and rigid region analysis to changes in displacement threshold τ and friction coefficient μ. For each set of thresholds, we compute the equivalent of Fig.2a-c in the main text, i.e. the rigid fraction as a function of z, and the correlations between rigid regions (here shown as insets) and rigid clusters using the adjusted Rand index. Outlined in red: effect of changing the displacement threshold from $\tau = 3 \times 10^{-7}$ to $\tau = 4 \times 10^{-5}$. Outlined in green: effect of changing the friction coefficient from $\mu = 0.3$ to $\mu = 0.2$. The values shown in Fig.2a-c of the main text are at the intersection of the red and green sets.

Appendix 3.E Adjusted rand index (ARI)

The Rand index [97] is a commonly-used statistical measure to quantify the degree of similarity between two different data clusterings. For a given set of n elements $E = \{e_1, e_2, e_3, ..., e_n\}$, two clustering methods obtain two partitions of E, call them $X = \{x_1, x_2, ..., x_r\}$ and $Y = \{y_1, y_2, ..., y_s\}$. Every element in X and Y is a subset of E. For each pair of elements in E, there are four cases:

1. in same subset of X and in the same subset of Y
2. in same subset of X but in different subsets of Y
3. in different subsets of X but in the same subset of Y
4. in different subsets in X and in different subsets of Y

The cases a, b, c, d together count the total number of pairs of elements, $\frac{n(n-1)}{2}$. The Rand index is then defined as the fraction

$$\mathrm{RI} = \frac{a+d}{a+b+c+d}. \tag{3.15}$$

By definition, RI is a number between 0 and 1, where 0 signifies maximum anti-correlation and 1 signifies maximum correlation. For random clustering, $\mathrm{RI} = 0.5$.

Since the Rand Index is computed by counting permutations, once the number of clusters or the size distribution of those clusters vary drastically, for example in low z cases and high z cases in our project, RI cannot capture the correlation between two clustering methods effectively. We therefore use the Adjusted Rand Index (ARI) [98] to remove such effects, in which the cases (a,b,c,d) are tabulated the same way but the number of possible combinations are taken into account:

$$\mathrm{ARI} = \frac{\binom{n}{2}(a+d) - (a+b)(a+c) - (d+b)(d+c)}{\binom{n}{2}\binom{n}{2} - (a+b)(a+c) - (d+b)(d+c)} \tag{3.16}$$

Unlike the RI, the ARI takes values from -1 to 1, with 0 corresponding to random clustering.

In Fig. 3.19 we also plot ARI for each set of parameters discussed in the last section in §3.D. Except for the extreme end of $\tau = 3 \times 10^{-7}$, these ARI plots show robust correlation between the two rigid analysis methods.

Chapter 4

A minimal model for correlated chromatin dynamics

This chapter is based on work primarily presented in the manuscript "Dynamic nuclear structure emerges from chromatin crosslinks and motors" co-authored by Alison E. Patteson, Edward J. Banigan and J. M. Schwarz. Manuscript is available on arxiv. J. M. Schwarz, Edward J. Banigan and I constructed the model. I wrote code and performed all numerical analysis. Alison E. Patteson provided experimental data and suggestions from experimental perspective. J. M. Schwarz and I wrote the manuscript and all our co-authors provided valuable suggestions and edits to improve the presentation and the content of it.

4.1 Correlated chromatin motion

The cell nucleus houses the genome, or the material containing instructions for building the proteins that a cell needs to function. This material is $\sim$ 1 meter of DNA with proteins, forming chromatin, and it is packaged across multiple spatial scales to fit inside a $\sim$ 10 μm nucleus [120]. Chromatin is highly dynamic; for instance, correlated motion of micron-scale genomic regions over timescales of tens of seconds has been observed in mammalian cell nuclei [121, 122, 123, 124, 125]. This correlated motion diminishes both in the absence of ATP and by inhibition of the transcription motor RNA polymerase II, suggesting that motor activity plays a key role [121, 122]. These dynamics occur within the confinement of the cell nucleus, which is enclosed by a double membrane and 10-30-nm thick filamentous layer of lamin intermediate filaments, the lamina [126, 127, 128]. Chromatin and the lamina interact through various proteins [129, 130, 131] and form structures such as lamina-associated domains (LADs) [132, 133]. Given the complex spatiotemporal properties of a cell nucleus, how do correlated chromatin dynamics emerge and what is their interplay with nuclear shape?

Numerical studies suggest several explanations for correlated chromatin motions. A confined Rouse chain with long-range hydrodynamic interactions that is driven by extensile dipolar motors can exhibit correlated motion over long length and timescales [123]. Correlations arise due to the emergence of local nematic ordering of within the confined globule. However, such local nematic ordering has yet to be observed. In the absence of activity, a confined heteropolymer may exhibit correlated motion, with anomalous diffusion of small loci [134, 135]. However, in marked contrast with experimental results [121, 122], introducing activity in such a model does not alter the correlation length at short timescales and decreases it at longer timescales.

Since there are linkages between chromatin and the lamina, chromatin dynamics may influence the shape of the nuclear lamina. Experiments have begun to investigate this notion by measuring nuclear shape fluctuations [136]. Depletion of ATP, the fuel for many molecular motors, diminishes the magnitude of the shape fluctuations, as does the inhibition of RNA polymerase II transcription activity by α-amanitin [136]. Other studies have found that depleting linkages between chromatin and the nuclear lamina, or membrane, results in more deformable nuclei [137, 138], enhanced curvature fluctuations [139], and/or abnormal nuclear shapes [140]. Interestingly, depletion

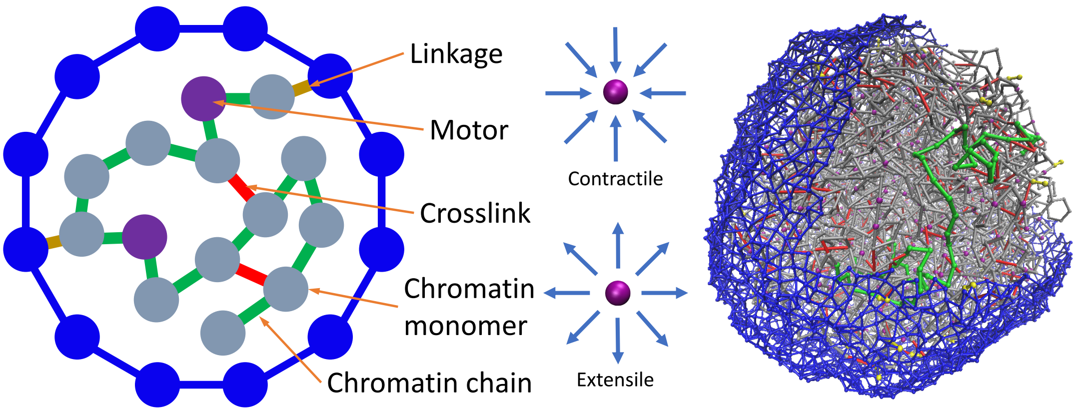

FIGURE 4.1: Left: Two-dimensional schematic of the model. Center: Schematic of the two types of motors. Right: Simulation snapshot.

of lamin A in several human cell lines leads to increased diffusion of chromatin, suggesting that chromatin dynamics is also affected by linkages to the lamina [141]. Together, these experiments demonstrate the critical role of chromatin and its interplay with the nuclear lamina in determining nuclear structure.

To understand these results mechanistically, we construct a chromatin-lamina system with the chromatin modeled as an *active* Rouse chain and the lamina as an elastic, polymeric shell with linkages between the chain and the shell. Unlike previous chain and shell models [142, 143, 139], our model has motor activity. We implement the simplest type of motor, namely extensile and contractile monopoles, representative of the scalar events addressed in an earlier two-fluid model of chromatin [144]. We also include chromatin crosslinks, which may be a consequence of motors forming droplets [145] and/or complexes [146], as well as chromatin binding by proteins, such as heterochromatin protein I (HP1) [147]. Recent rheological measurements of the nucleus support the notion of chromatin crosslinks [142, 143], as does indirect evidence from chromosome conformation capture (Hi-C) [148]. In addition, we explore how the nuclear shape and chromatin dynamics mutually affect each other by comparing results for an elastic, polymeric shell with those of a stiff, undeformable one.

4.2 Model

Interphase chromatin is modeled as a Rouse chain consisting of 5000 monomers with radius r_c connected by Hookean springs with spring constant K. We include excluded volume interactions with a repulsive, soft-core potential between any two monomers, ij, and a distance between their centers denoted as $|\vec{r}_{ij}|$, as given by $U_{ex} = \frac{1}{2}K_{ex}(|\vec{r}_{ij}| - \sigma_{ij})^2$ for $|\vec{r}_{ij}| < \sigma_{ij}$, where $\sigma_{ij} = r_{c_i} + r_{c_j}$, and zero otherwise. We include N_C crosslinks between chromatin monomers by introducing a spring between different parts of the chain with the same spring constant as along the chain. In addition to (passive) thermal fluctuations, we also allow for explicit motor activity along the chain. In simulations with motors, we assign some number, N_m, of chain monomers to be active. An active monomer has motor strength M and exerts force $\mathbf{F_a}$ on monomers within a fixed range. Such a force may be attractive or "contractile," drawing in chain monomers, or alternatively, repulsive or "extensile," pushing them away (Fig. 4.1). Since motors *in vivo* are dynamic, turning off after some characteristic time, we include a turnover timescale for the motor monomers τ_m, after which a motor moves to another position on the chromatin.

The lamina is modeled as a layer of 5000 identical monomers connected by springs with the same radii and spring constants as the chain monomers and an average coordination number $z \approx 4.5$, as supported by previous modeling [142, 143, 139] and imaging experiments [126, 127, 128]. Shell monomers also have a repulsive soft core. We model the chromatin-lamina linkages as N_L permanent springs with stiffness K between shell monomers and chain monomers (Fig. 4.1).

The system evolves via Brownian dynamics, obeying the overdamped equation of motion: $\xi \dot{\mathbf{r}}_i = (\mathbf{F_{br}} + \mathbf{F_{sp}} + \mathbf{F_{ex}} + \mathbf{F_a})$, where $\mathbf{F_{br}}$ denotes the (Brownian) thermal force, $\mathbf{F_{sp}}$ denotes the harmonic forces due to chain springs, chromatin crosslink springs, and chromatin-lamina linkage springs, and $\mathbf{F_{ex}}$ denotes the force due to excluded volume.

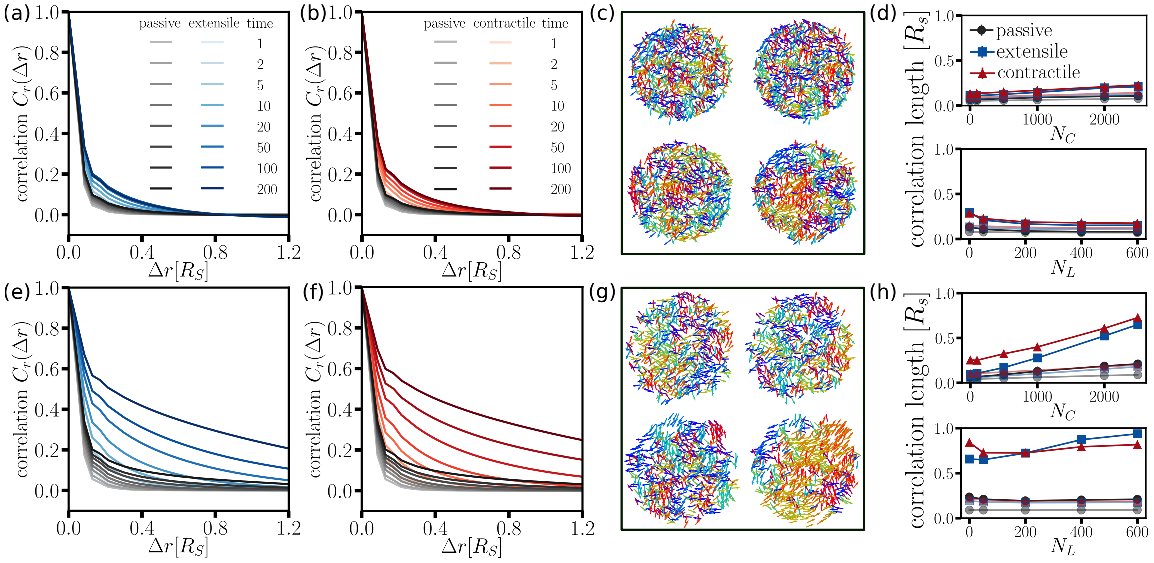

FIGURE 4.2: (a) The spatial autocorrelation function $C_r(\Delta r, \Delta\tau)$ for passive and extensile cases at different time lags, $\Delta\tau$, for the hard shell, while (b) shows the contractile and passive case. (c) Two-dimensional vector fields for $\Delta\tau = 5$ (left), 50 (right) for the passive case (top) and the contractile case (bottom). (d) The correlation length as a function of N_L and N_C for the two time lags in (c). (e∼h): The bottom row shows the same as the top row, but with a soft shell. See SM for representative fits to obtain the correlation length.

We use Euler updating, a time step of $d\tau = 10^{-4}$, and a total simulation time of $\tau = 500$. For the passive system, $\mathbf{F_a} = 0$. In addition to the deformable shell, we also simulate a hard shell by freezing out the motion of the shell monomers. To assess the structural properties in steady state, we measure both the radial globule, R_g, of the chain and the self-contact probability. After these measures do not appreciably change with time, we consider the system to be in steady state. See SM for these measurements, simulation parameters, and other simulation details.

4.3 Results

We first look for correlated chromatin motion in both hard shell and deformable shell systems. We do so by quantifying the correlations between the displacement fields at two different points in time. Specifically, we compute the normalized spatial autocorrelation function defined as $C_r(\Delta r, \Delta\tau) = \frac{1}{N(\Delta r)} \sum_{N(\Delta r)} \frac{<\mathbf{d_i}(\mathbf{r},\boldsymbol{\Delta\text{ø}})\cdot\mathbf{d_j}(\mathbf{r}+\boldsymbol{\Delta}\mathbf{r},\boldsymbol{\Delta\text{ø}})>}{<\mathbf{d}^2(\mathbf{r},\boldsymbol{\Delta\text{ø}})>}$, where $\Delta\tau$ is the time window, Δr is the distance between the centers of the two chain monomers at the beginning of the time window, $N(\Delta r)$ is the number of ij pairs of monomers within distance Δr of each other at the beginning of the time window, and $\mathbf{d_i}$ is the displacement of the i^{th} chain monomer during the time window, defined with respect to the origin of the system. Two chain monomers moving in the same direction are positively correlated, while monomers moving in opposite directions are negatively correlated.

Fig. 4.2 shows $C_r(\Delta r, \Delta\tau)$ for passive and active samples in both hard shell (Figs. 4.2 (a) and (b)) and soft shell cases for $N_C = 2500$, $N_L = 50$, and $M = 5$ (Figs. 4.2 (e) and (f)). Both the passive and active samples exhibit short-range correlated motion when the time window is small, *i.e.*, $\Delta\tau < 5$. However, for longer time windows, both the extensile and contractile active samples exhibit more long-range correlated motion than the passive case. These correlations are visible in quasi-2d spatial maps of instantaneous chromatin velocities, which show large regions of coordinated motion in the active, soft shell case (Figs. 4.2 (c) and (g)).

To extract a correlation length to study the correlations as a function of both N_C and N_L, we use a Whittel-Marten (WM) model fitting function $C_r(r) = \frac{2^{1-\nu}}{\Gamma(\nu)} \left(\frac{r}{r_{cl}}\right)^{\nu} K_{\nu} \left(\frac{r}{r_{cl}}\right)$ for each time window (Fig. 4.2 (f)) [122]. The parameter ν is approximately 0.2 for all cases studied. For the hard shell, the correlation length decreases with number of linkages (Fig. 4.2 (d)). This trend is opposite in deformable shell case with activity and long time lags (Fig. 4.2 (h)). For the hard shell, linkages effectively break up the chain into uncorrelated regions. For the soft shell, the shell deforms in response to active fluctuations in the chain. For both types of shells, the correlation length increases with the number of crosslinks (Figs. 4.2 (d) and (h)), with a more significant increase in the soft shell active case. It is also interesting to note that the lengthscale for the contractile case is typically larger than that of the extensile case, at least for smaller numbers of linkages.

Given the differences in correlation lengths between the hard and soft shell systems, we looked for net motion of the system in the soft shell case. Net motion has been observed in active particle systems confined by a deformable shell [149]. Similarly, we observe the active chain system moving faster than diffusively (see SM). In the shell's center-of-mass frame, the correlation length is decreased, but still larger than in the hard shell simulations (see SM). Interestingly, experiments demonstrating large-scale correlated motion measure chromatin motion with an Eulerian specification (*e.g.*, by particle image velocimetry) and do not subtract off the global center of mass [121, 122, 125]. However, one experiment noted that they observed drift of the nucleus on a frame-to-frame basis, but considered it negligible over the relevant time scales [122]. Additionally, global rotations, which we have not considered, could yield large-scale correlations.

We also study the mean-squared displacement of the chromatin chain to determine if the experimental feature of anomalous diffusion is present. Figs. 4.3 (a) and (c) show the mean-squared displacement of the chain with $N_L = 50$ and $N_C = 2500$ as measured with reference to the center-of-mass of the shell for both the hard shell and soft shell cases, respectively. For the hard shell, the passive chain initially moves subdiffusively with an exponent of $\alpha \approx 0.5$, which is consistent with an uncrosslinked Rouse chain with excluded volume interactions [150]. However, the passive system crosses over to potentially glassy behavior after a few tens of simulation time units. We present $N_C = 0$ case in the inset to Fig. 4.3 (a) for comparison to demonstrate that crosslinks are potentially driving a gel-sol transition as observed in prior experiments [151]. The active hard shell samples exhibit larger displacements than passive

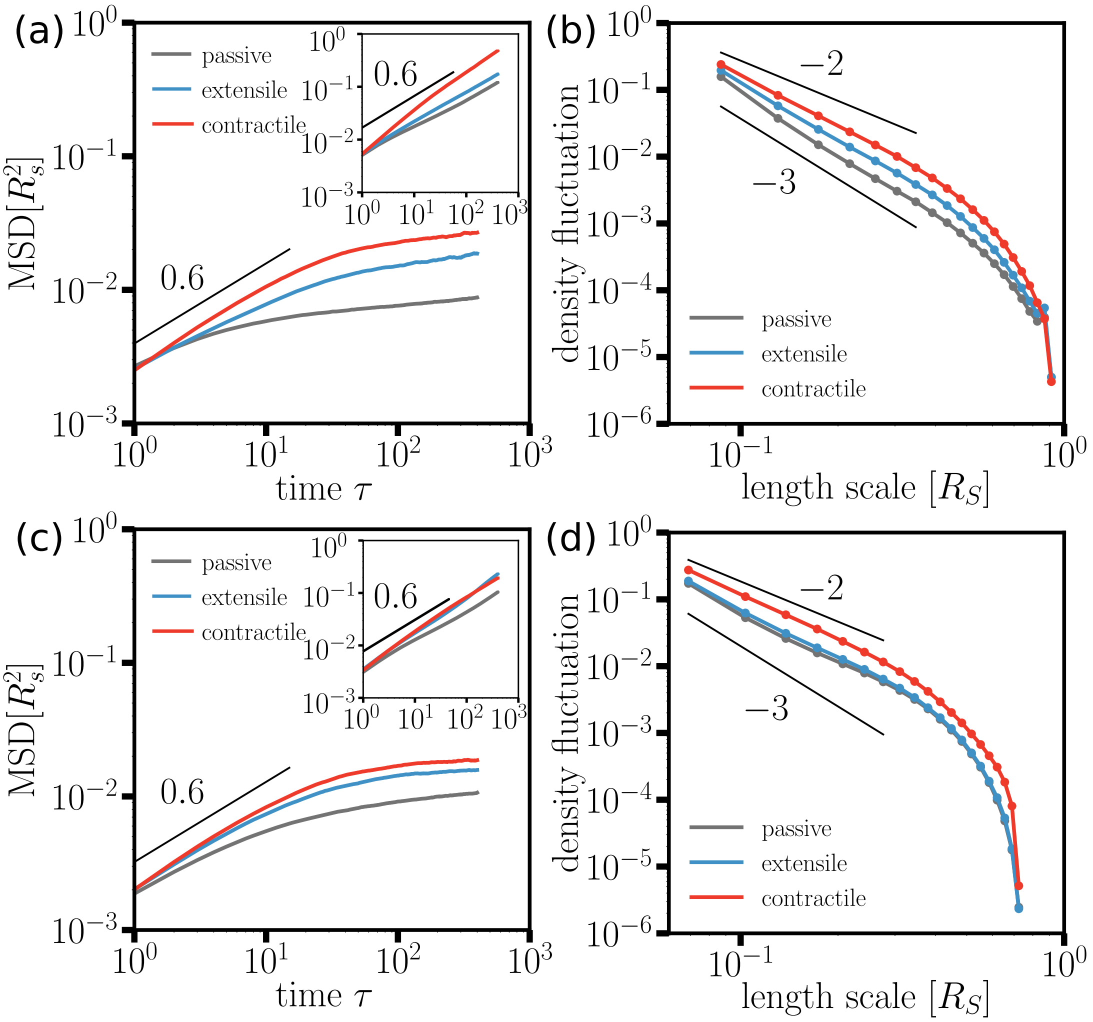

FIGURE 4.3: (a) MSD for the hard shell case with $N_C = 2500$ and $N_L = 50$. For the inset, $N_C = 0$. (b) Density fluctuations for the same parameters as in (a). Figures (c) and (d) show the soft shell equivalent to (a) and (b).

samples, with $\alpha \sim 0.6$ initially before crossing over to a smaller exponent at longer times.

Additionally, the contractile system exhibits larger displacements than the extensile system. We found that a broader spectrum of steady-state density fluctuations for the contractile system drive this behavior (Fig. 4.3 (b)). This generates regions of lower density into which the chain can move, leading to increased motility. The active cases exhibit anomalous density fluctuations, with the variance in the density falling off

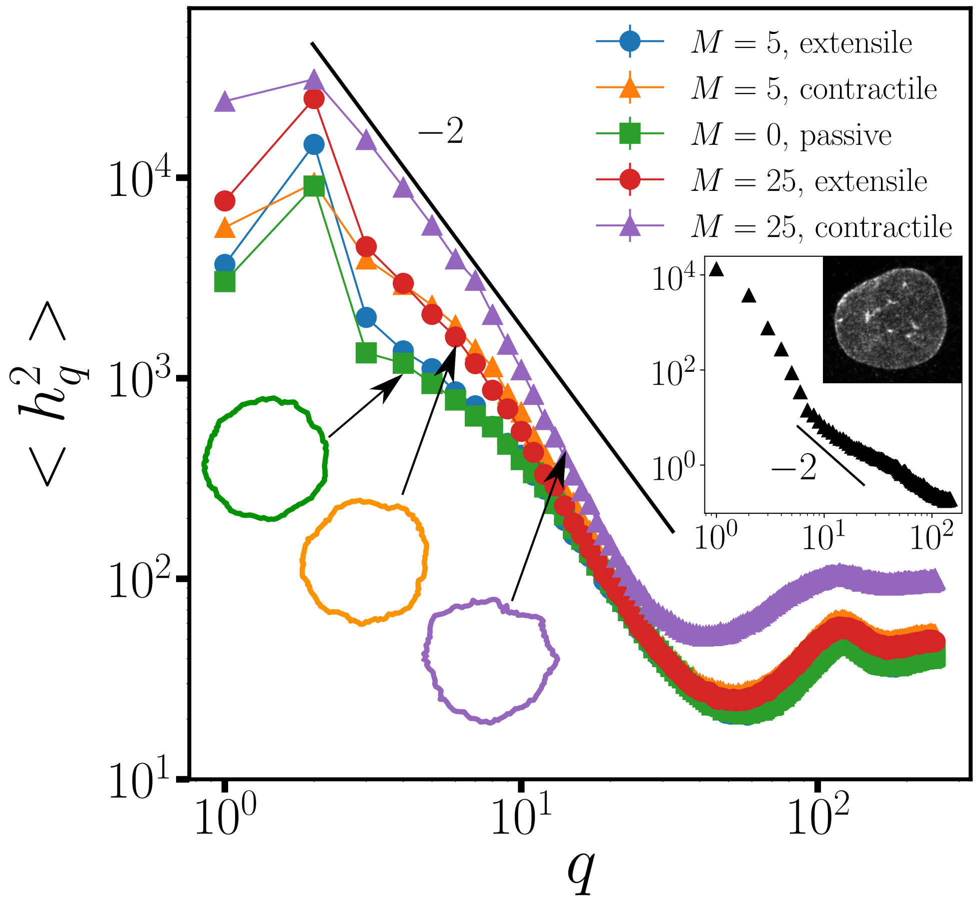

FIGURE 4.4: Power spectrum of the shape fluctuations with $N_L = 50$ and $N_C = 2500$ for the passive and both active cases. Different motor strengths are shown. The insets shows experimental data from mouse embryonic fibroblasts with an image of a nucleus with lamin A/C stained.

more slowly than inverse length cubed (in 3D). Finally, the MSD in the hard shell case is suppressed by more boundary bindings or crosslinks. For the soft shell case, we observe similar trends as the hard shell, except that the soft shell does not inhibit the potential gel-sol transition.

Next, we examine nuclear shape. In Figure 4.4, we plot the power spectrum of the shape fluctuations of the shell for a central cross-section as a function of wavenumber q for different motor strengths. We observe that the shape fluctuation spectrum is broad until saturating due to the discretization of the system. The decrease in the shape fluctuations is less significant for both the passive and extensile systems than for the contractile system with an approximate q^{-2} scaling, characteristic of membrane tension, for the former versus an approximate q^{-3} scaling for the latter. This difference could be due to the more anomalous density fluctuations in the contractile case, demonstrating that chromatin spatiotemporal dynamics directly impacts nuclear shape. We do not observe a q^{-4} contribution due to emergent bending, which was suggested by previous experiments [136] and simulations [142]. However, additional experiments measuring nuclear shape fluctuations of mouse embryonic fibroblasts (MEFs) also do not show a bending contribution (inset to Fig. 4.4 and see SM for materials and methods). Additionally, the amplitude of the shape fluctuations increases with motor strength, N_C, and N_L (see SM).

4.4 Discussion

We have studied a composite chromatin-lamina system in the presence of activity, crosslinking, and number of linkages between chromatin and the lamina. Our model captures the correlated chromatin motion on the scale of the nucleus in the presence of both activity and crosslinks (Fig. 4.2). The deformability of the shell also plays a role. We find that global translations of the composite soft shell system contribute to the correlations. We observe anomalous diffusion for the chromatin (Figs. 4.3 (a) and (c)), as has been observed experimentally [141], with a crossover to a smaller anomalous exponent driven by the crosslinking [151]. Interestingly, the contractile system exhibits a larger MSD than the extensile one, which is potentially related to the more anomalous density fluctuations in the contractile case (Figs. 4.3 (b) and (d)). Finally, nuclear shape fluctuations depend on motor strength and on amounts of crosslinking and chromatin-lamina linkages (Fig. 4.4). Notably, the contractile case exhibits more dramatic changes in the shape fluctuations as a function of wavenumber as compared to the extensile case.

Our short-ranged, overdamped model contrasts with an earlier confined, active Rouse chain interacting with a solvent via long-range hydrodynamics [123]. While both models generate correlated chromatin dynamics, with the earlier model, such correlations are generated only with extensile motors that drive local nematic ordering of the chromatin chain [123]. Moreover, our correlation lengths are significantly larger than those obtained in a confined active, heteropolymer simulation [134]. Activity in this earlier model is modeled as extra-strong thermal noise such that the correlation length decreases at longer time windows as compared to the passive case. This decrease contrasts with our results (Figs. 4.2 (d) and (h)) and experiments [122]. In addition, our model takes into account deformability of the shell and the chromatin-lamina linkages. Future experiments could potentially distinguish these mechanisms by looking for prominent features of our model, such as a dependence on chromatin bridging proteins and linkages to the lamina and effects of whole-nucleus motions.

Our modeling motivates further spatiotemporal studies of nuclear shape. Particularly interesting would be *in vivo* studies with vimentin-null cells, which have minimal mechanical coupling between the cytoskeleton and the nucleus. Vimentin is a cytoskeletal intermediate filament that forms a protective cage on the outside of the nucleus and helps regulate the nucleus-cytoplasm coupling and, thus, affects nuclear shape [152]. The amplitudes of the nuclear shape fluctuations in vimentin-null cells may increase due to a softer perinuclear shell or may decrease due to fewer linkages between the nucleus and the mechanically active cytoskeleton.

There are intriguing parallels between cell shape [153, 154, 155] and nuclear shape with cell shape being driven by an underlying cytoskeletal network—an active, filamentous system driven by polymerization/depolymerization, crosslinking, and motors, both individually and in clusters, that can remodel, bundle and even crosslink filaments. Given the emerging picture of chromatin motors acting collectively [145, 146], just as myosin motors do [156], the parallels are strengthened. Moreover, the more anomalous density fluctuations for the contractile motors as compared to the extensile motors could potentially be relevant in random actin-myosin systems typically exhibiting contractile behavior, even though either is allowed by a statistical symmetry [157]. On the other hand, distinct physical mechanisms may govern nuclear shape since the chromatin fiber is generally softer than cytoskeletal filaments and the lamina is stiffer than the cell membrane.

We now have a minimal chromatin-lamina model that can be augmented with additional factors, such as different types of motors—dipolar, quadrupolar, and even chiral, such as torque dipoles. Chiral motors may readily condense chromatin just as twirling a fork "condenses" spaghetti. Finally, it is now established that nuclear actin exists in the cell nucleus, yet its form is under investigation [158]. We propose that short, but stiff, actin filaments acting as stir bars can potentially increase the correlation length of micron-scale chromatin dynamics. Including such factors will help us further quantify nuclear dynamics to determine, for example, mechanisms for extreme nuclear shape deformations, such as nuclear blebs [159], and ultimately how nuclear spatiotemporal structure affects nuclear function.

Appendix 4.A Model

4.A.1 Algorithm

We use a Rouse chain with soft-core repulsion between each monomer capturing excluded volume effects to represent the chromatin. Since the chromatin is contained within the lamina, modeled as a polymeric shell, we present the protocol to obtain the initial configuration for the composite system. As shown in Fig. 4.5(left), we first implement a three-dimensional self-avoiding random walk in an FCC lattice for 5000 steps to generate the chain. We then surround the chain in a large polymeric, but hard, shell. To create the shell, we generate a Fibonacci sphere with 5000 nodes and identify 5000 identical monomers with these nodes. The springs between the shell monomers form a mesh and each shell monomer is connected to 4.5 other shell monomers on average. These monomers have same physical properties as the chain monomers in terms of size and spring strength.

We then shrink the shell (Fig. 4.5(center)) by moving the shell monomers inwards by the same amount. During the shrinking process, chain monomers interact with the shell monomers via the soft-core repulsion and, therefore, also move inwards. In addition, every chain monomer experiences thermal fluctuations and is constrained by elastic forces and soft-core repulsion forces. Once the shell radius reaches its destination radius after some time, we then thermalize the positions of the shell monomers and adjust rest length of springs respectively to make the mesh less lattice-like. We, thus, arrive at the initial configuration of the system Fig. 4.5(right). We obtain 100 such initialized samples to obtain an ensemble average for each measurement. The destination radius R_s is 10. We set the monomer radius to be $r_c = 0.43089$ so that the packing fraction ϕ is approximately 0.4 in the hard shell limit comparable to electron microscopy tomography experiments [160], simulations of chromatin confined within the nucleus [161], and theoretical estimates [162], while ϕ is smaller in soft-shell cases due to expansion as the shell monomers undergo thermal fluctuations.

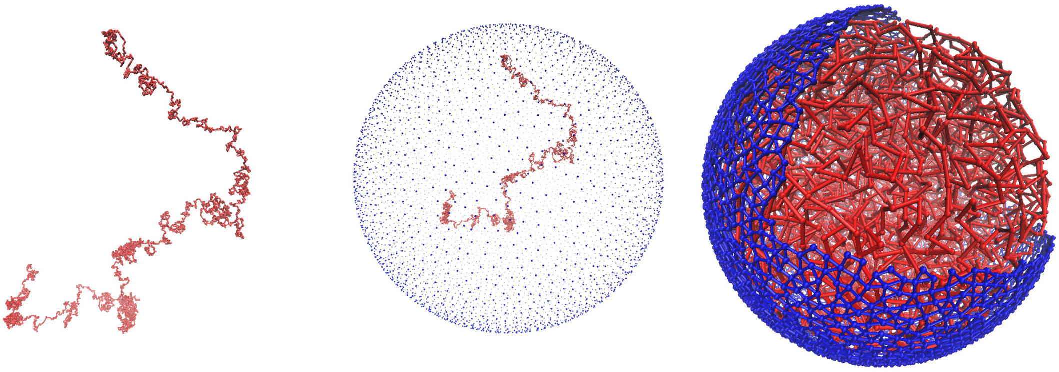

FIGURE 4.5: Left: The chain is initially generated via a self-avoiding random walk on an FCC lattice. Center: The chain is then enclosed in a Fibonacci sphere. Right: Composite system at time $\tau = 0$.

4.A.2 Parameters

In our simulations, we use the set of parameters shown in Table 1.

Diffusion constant	D	1
Thermal energy	$k_B T$	1
Simulation timestep	$d\tau$	10^{-4}
Number of chain monomers	N	5000
Radii of chain monomers	r_c	0.43089
Number of shell monomers	N_s	5000
Radii of shell monomers	r_s	0.43089
Radius of hard shell	R_s	10
Packing fraction	ϕ	0.400
Spring constant	K	140
Soft-core repulsion strength	K_{ex}	140
Number of motors	N_m	400
Motor strength	M	5/25
Turnover time for motors	τ_m	0.05
Number of crosslinks	N_C	0/100/500/1000/2000/2500
Number of linkages	N_L	0/50/200/400/600
Damping	ξ	1

We now address how the simulation parameters map to biological values. One simulation length unit corresponds to 1 μm, one simulation time unit corresponds to 0.5 seconds, and one simulation energy scale corresponds to approximately $10^{-21}\,J = k_B T$, $T = 300$ K. With this mapping, the spring constant corresponds to approximately $1.4 \times 10^{-4}\ \frac{\text{nN}}{\mu\text{m}}$ with a Young's modulus for the chain of 0.28 Pa.

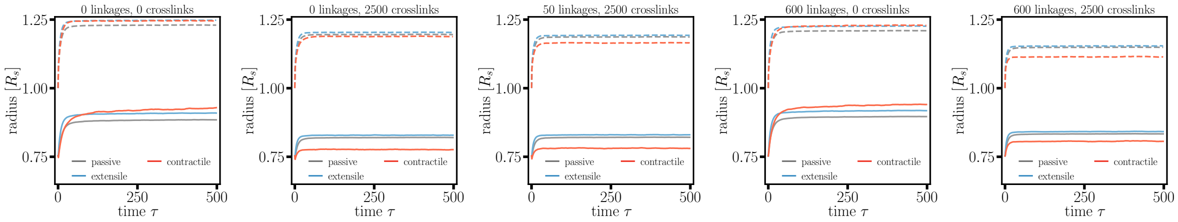

FIGURE 4.6: Radius of gyration of the chain (solid lines) and average radius of the shell(dashed lines) as function of simulation time for $N_C = 2500$ and $N_L = 50$ (middle figure). For contrast, R_g for $N_L = 0, 600$ and $N_c = 0, 2500$ are also plotted. Only the soft shell case are shown.

Appendix 4.B Simulation results

4.B.1 Globule radius

For a polymer, the radius of gyration is defined as $R_g = \sum(r_i - r_{cm})^2/N$, where $N = 5000$ is total chain monomer number. In the hard shell case, we fix the radius of the shell to $R_s = 10$. In the soft-shell case, the shell expands due to the thermal fluctuations and due to the activity of the chain inside. Fig 4.6 shows the radius of gyration of the chain (solid lines) and the average radius of shell (dashed lines) in the soft shell case as function of time. After a short-time initial expansion, both the chain's and the shell's respective radii reach a plateau by $100\,\tau$ for most parameters, indicating that the system is reaching steady state. Only for the zero crosslinks with contractile activity, does the radius of gyration continue to increase slightly over the duration of the simulation of $500\,\tau$.

4.B.2 Self-contact probability

Since the globule radius is an averaged quantity, we also look for steady state signatures in the self-contact probability, which yields information about the chromatin spatial structure. More specifically, Hi-C allows one to quantify the local chromatin interaction domains at the megabase scale [163]. Such domains are stable across different eukaryotic cell types and species [164]. To quantify such interactions in the simulations, one determines the number of monomers in the vicinity of the *ith* chain monomer. In other words, one creates an adjacency matrix. This adjacency matrix is shown Fig. 4.7 for two examples. To compute the self-contact probability, one sets a threshold distance that a pair of monomers within that range is considered to be in contact. Then the fraction of contacted pairs for each polymeric distance $1, 2, 3, 4, ...$ is calculated. This fraction as a function of polymeric distance is called the self-contact probability. See Fig. 4.8 for the self-contact probability for $N_L = N_C = 0$ at the beginning and at the end of the simulation for the soft shell case. While there is some change between the two, in Fig. 4.9, we show the self-contact probability for different times τ to demonstrate that after $\tau = 50$, the probability does not change with time, implying a steady state.

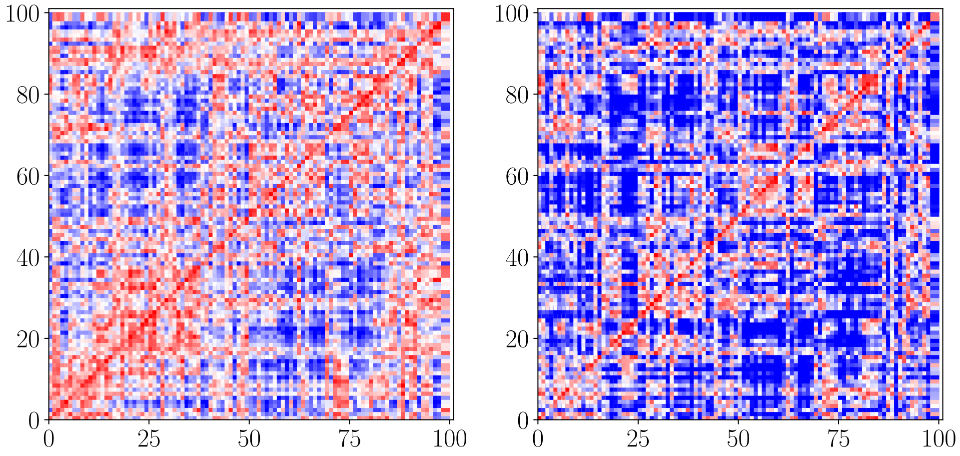

FIGURE 4.7: Contact map for a contractile system with no linkages or cross links at the beginning and at the end of the simulation, i.e. $\tau = 0$ and$\tau = 500$.

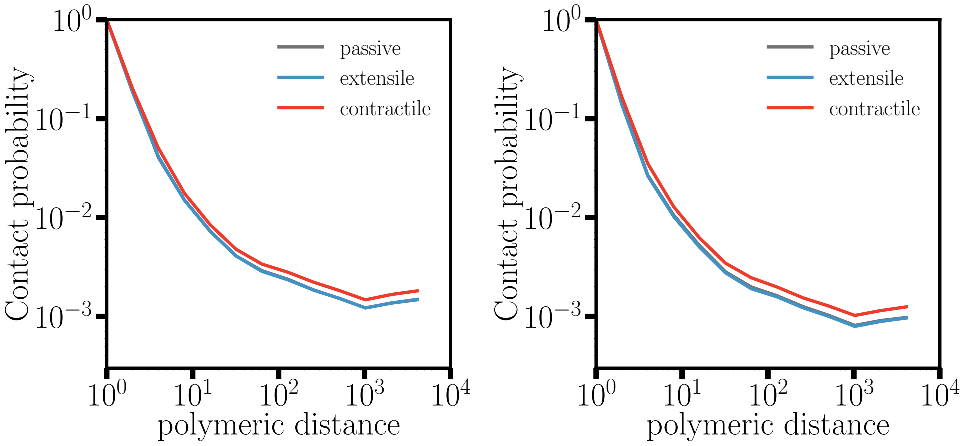

FIGURE 4.8: Final Self-contact probability at a stable state for hard shell case(left) and soft shell case(right), corresponding to right figure in previous Fig. 4.7.

4.B.3 MSD

To quantify the dynamics of the chain, we compute its mean-squared displacement (MSD) measured with respect to the center of mass of the shell. Fig. 4.10 plots the MSD of the chain during the duration of the simulation. At short time scales, the chain undergoes sub-diffusive motion and the MSD follows an exponent around $\alpha \approx 0.6$ for $N_C = 2500$ and $N_L = 50$. At longer time scales, the MSD crosses over to a smaller exponent. The value of the exponent depends on N_C and N_L. In all cases, the active systems diffuse faster than the passive system, and contractile motors enhance diffusion more than extensile motors. The insets in Fig. 4.10 show the MSD for the center of mass of the chromatin chain for the soft shell. For the crosslinked, active chain, this MSD is slightly faster than diffusive.

4.B.4 Density fluctuations

The density fluctuations are computed in the following way:

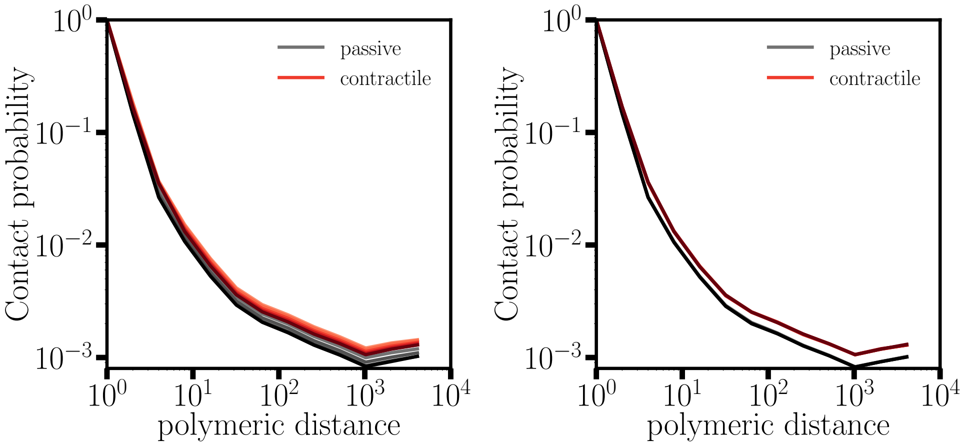

FIGURE 4.9: Self-contact probability at $\tau = 0, 1, 2, 10, 20, 50\,\tau$ (left) and for $\tau = 50$ and $\tau = 300$ (right) for soft shell passive and contractile systems with $N_C = 2500$ and $N_L = 50$.

- Select a spherical region in the system with radius r_d and count the number of monomers in that region.
- Randomly select spherical regions at other places with the same radius and count the monomers included.
- Compute the variance of counted monomer amount σ^2 for this radius r_d.
- Vary r_d and repeat the above three steps and obtain the variance for each r_d.

We plot σ^2 as a function of r_d. Typically, for a group of randomly distributed monomers in three dimensions, the density fluctuations scale as $\sigma^2 \sim r_d^{-3}$. From Fig. S7 we see that the overall density fluctuations are broader in the active cases, as compared to the passive cases. Contractile motors induce more anomalous density fluctuations, particularly in the soft shell case.

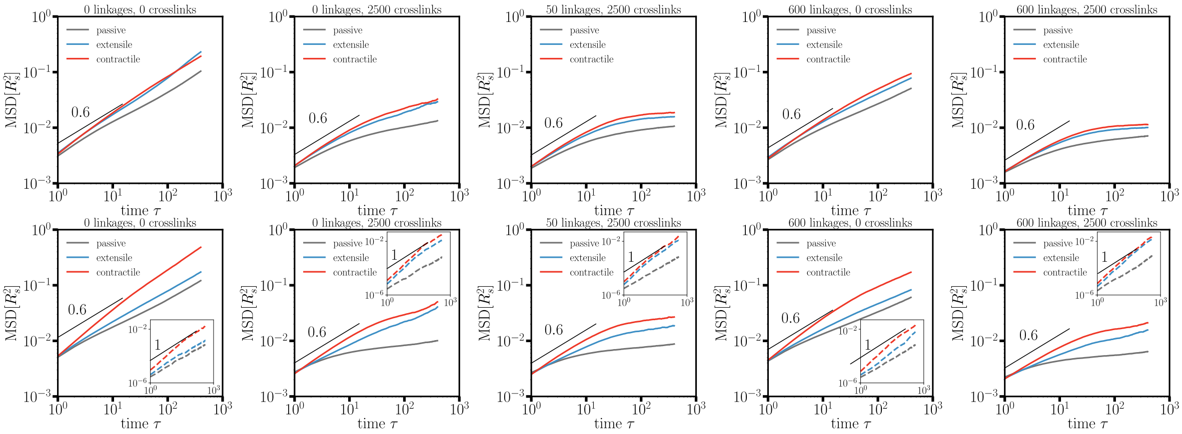

FIGURE 4.10: MSD as a function of time for $N_C = 2500$, $N_L = 50$, and $M = 5$ (middle column) and for four extreme cases (0 or 600 linkages, 0 or 2500 crosslinks) in the hard shell (top row) and the soft shell (bottom row). Insets are MSD plots of the center of mass of the chain.

4.B.5 Correlation function and correlation length

To evaluate the spatial and temporal correlation motion along the chain, we compute the spatial autocorrelation function. Suppose $\vec{d}(\vec{r}, \Delta\tau)$ is the displacement of monomer at $\vec{r}$ over time, $\vec{d}(\vec{r} + \Delta r, \Delta\tau)$ is the displacement of another monomer, which is located a distance Δr away and over the same time window. We then use the function below to compute the correlation function:

$$C(\Delta r, \Delta\tau) = \frac{\langle \vec{d}(\vec{r}, \Delta\tau) \cdot \vec{d}(\vec{r} + \Delta r, \Delta\tau) \rangle}{\langle \vec{d}^2(\vec{r}, \Delta\tau) \rangle}.$$

.

From Ref. [122] we assume the correlation function follows $C_r(r) = \frac{2^{1-\nu}}{\Gamma(\nu)} \left(\frac{r}{r_{cl}} \right)^{\nu} K_\nu \left(\frac{r}{r_{cl}} \right)$, where r_{cl} is the extracted correlation length, K_ν is the Bessel of the second type of order ν, and ν is a smoothness parameter. Larger ν denotes that the underlying spatial process is smooth, not rough, in space. In Fig. 4.12 we show the correlated function computed from numerical simulations (dots) and the fitted correlation function from the above formula (lines) for different parameters. Lines from light to dark represent

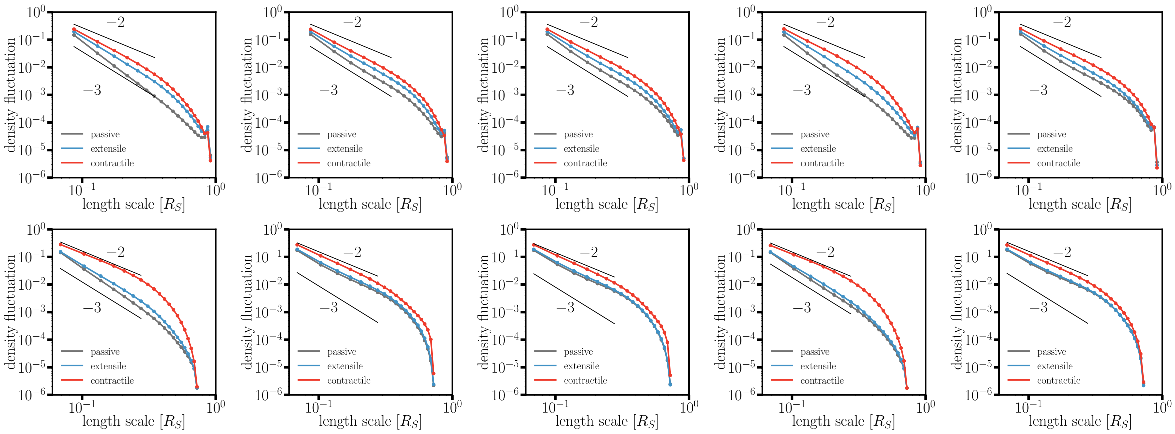

FIGURE 4.11: Density fluctuations for default sample(middle column) and four extreme samples(0 or 600 linkages, 0 or 2500 cross links) in hard-shell(top) and soft-shell(bottom) cases.

time windows from short to long ($1\,\tau$, $2\,\tau$, $5\,\tau$, $10\,\tau$, $20\,\tau$, $50\,\tau$, $100\,\tau$, $200\,\tau$). We see that the numerical results with shorter time windows fit the formula better.

In Fig. 4.13, we plot the correlation length a function of linkage number N_L and crosslink number N_C over the short time window $5\,\tau$ and the long time window $50\,\tau$. We observe that active motors clearly enhance the correlation length. It is also clear that presence of crosslinks also enhance correlation length. The correlation length is larger for the soft shell case. In the soft shell case, without subtracting the diffusion of the center of mass, the correlation length for the long time window spans almost the radius of the system. We note that the correlation length is reduced if we subtract the center of mass shell motion, however, it still remains larger than the hard shell case. A quasi-two-dimensional correlation length is computed from a slab-like region and is also shown for potential comparison to experimental results since, in the experiments, the correlated length is extracted using this method. There is not much difference between the three-dimensional correlation length and the two-dimensional correlation length with the center of mass of the shell subtracted. We also show the corrrelation length as a function of shell stiffness (with the COM of shell subtracted) to demonstrate the direct effect of shell stiffness on the correlated chromatin motion (see Fig. 4.14).

4.B.6 Shape fluctuations

To evaluate shape fluctuations of the shell, we compute it in two ways. First, in order to compare with experimental measurements, we select a random slab through the center and project the coordinates of the shell monomers in the slab to the plane where slab lies. Then, we compute the fast-Fourier-transform (FFT) for spatial deviations of these monomers from the average radius with the deviations with h_q denoting the Fourier transform of the deviation with respect to wavenumber q. In Fig. 4.15, the power spectrum of the shape fluctuations for the passive and extensile cases follow a decay exponent of -2, as expected for a stretchable shell [165]. The spectrum of the shape fluctuations increases monotonically with the number of crosslinks. The specturm varies more dramatically with contractile motors as compared to extensile motors. Moreover, the shape fluctuation spectrum also eventually saturates as a function of chromatin-lamina linkage number. In 4.16 we compute the spectrum of the shape fluctuations as characterized by the spherical harmonic functions (the Y_{lm}s with l as the dimensionless spherical wavenumber). We obtain similar trends as in Fig. 4.15. Finally, in Fig. 4.17, we plot the spectrum for different motor strengths and different shell stiffnesses.

Appendix 4.C Experiments

To measure nuclear shape fluctuations in live cells, the wild-type mouse embryonic fibroblasts (mEFs) were kindly provided by J. Eriksson, Abo Akademi University, Turku, Finland. Cells were cultured in DMEM with 25 mM Hepes and sodium pyruvate supplemented with 10% FBS, 1% penicillin/streptomycin, and nonessential amino acids. The cell cultures were maintained at 37 degrees C and 5% CO_2.

Cell nuclei were fluorescently labeled by transient transfection with pEGFP-C1-NLS, 48 h before imaging. Cell nuclei were imaged at 2-min increments for 2 h by using wide-field fluorescence with a 40× objective. To quantify the structural features of nuclei, we traced the contour, $r(\theta)$, of the NLS-GFP labeled nuclei at each time point. The shape of the nucleus was identified using a custom-written Python script, and its contour was interpolated from 0 to 2π by 150 points. Next, the shape fluctuations were calculated as $h(\theta) = r(\theta) - r_0$, where r_0 is the average radius for each cell at each time point. The wave number-dependent Fourier modes of the fluctuations, h_q, were obtained as Fourier transformation coefficients, as described in Ref [152].

The shape fluctuations were quantified for each cell by computing the Fourier mode magnitude square $h^2(q)$ and averaging over each time point. The average shape fluctuations as shown in Fig. 4 in the main text was taken as the average over 15 cells per condition from two independent experiments.

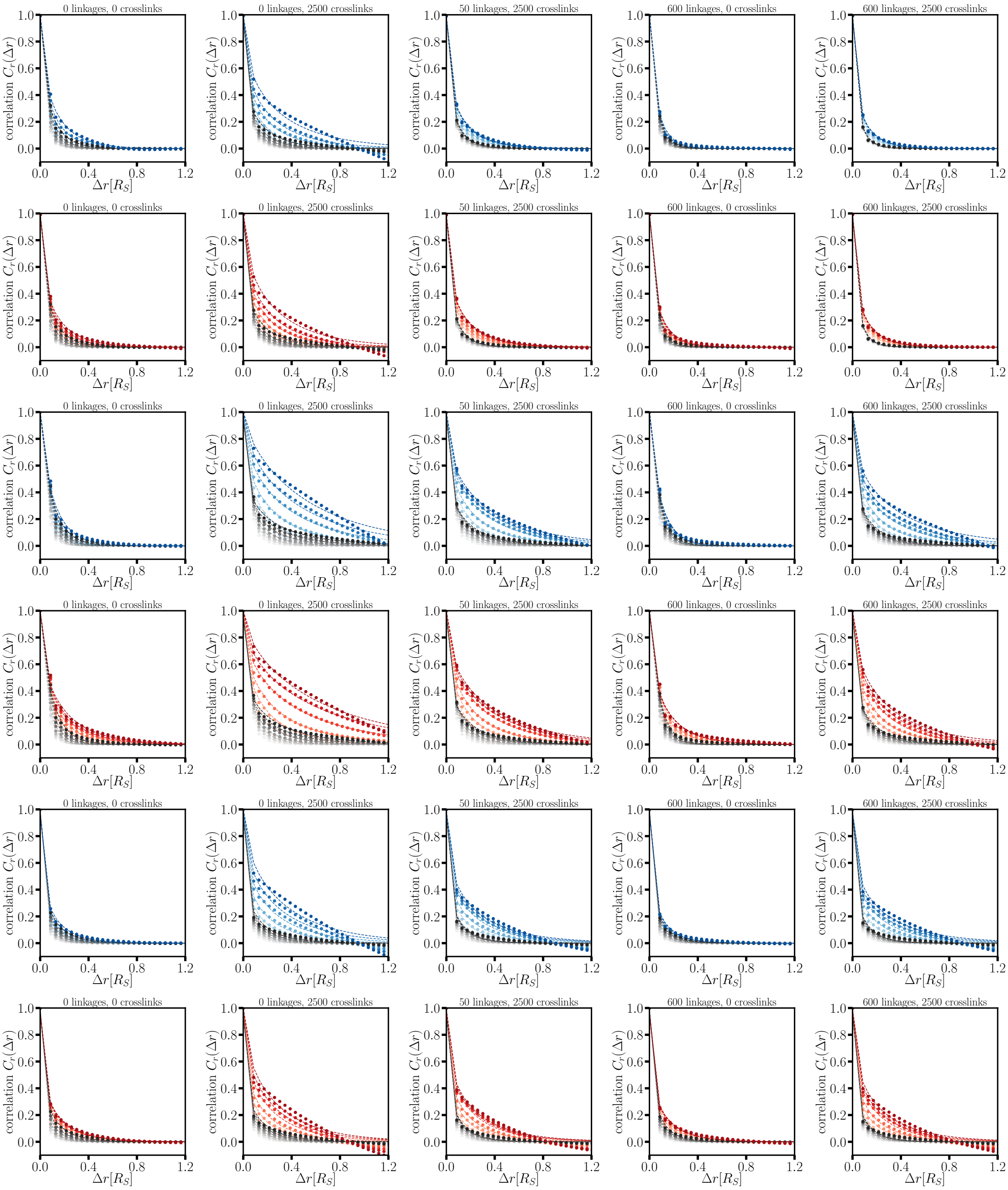

FIGURE 4.12: Correlation functions for $N_C = 2500$ and $N_L = 50$ (middle column) and four extreme cases (left column: 0 linkages and 0 crosslinks; second from left column: 0 linkages and 2500 crosslinks; second from right column: 600 linkages and 0 crosslinks; right column: 600 linkages and 2500 crosslinks). Top two rows: The three-dimensional correlation function for the hard shell; Middle two rows: The three-dimensional correlation functions for the soft shell; Bottom two rows: Two-dimensional correlation functions for the soft shell. Color varies from light to dark as time lag equals $1\,\tau$, $2\,\tau$, $5\,\tau$, $10\,\tau$, $20\,\tau$, $50\,\tau$, $100\,\tau$, $200,\tau$, respectively. Symbols denote the numerical results, while the dashed line represent the fitted correlation functios. Greyscale: passive. Bluescale: active with extensile motors. Redscale: active with contractile motors.

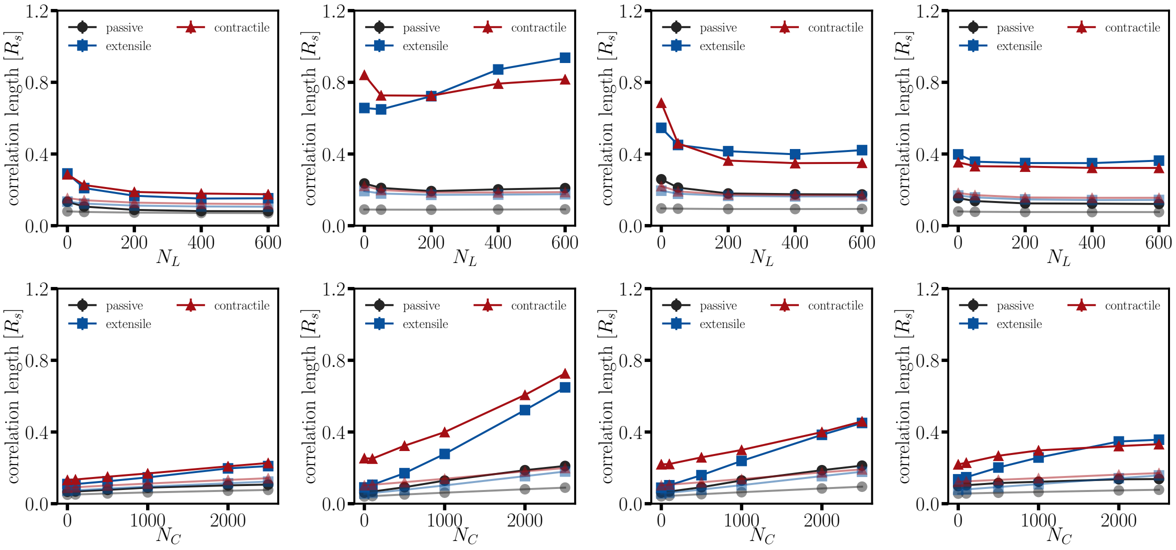

FIGURE 4.13: Plot of correlation length as function of linkage number N_L (top row) or crosslink number N_C (bottom row) for time windows $5\,\tau$ (light) and $50\,\tau$ (dark). From left to right columns: The three-dimensional correlation length for the hard shell; the three-dimensional correlation length for the soft shell; three-dimensional correlation length for the soft shell with the COM motion subtracted; two-dimensional correlation length for the soft shell with the COM motion subtracted.

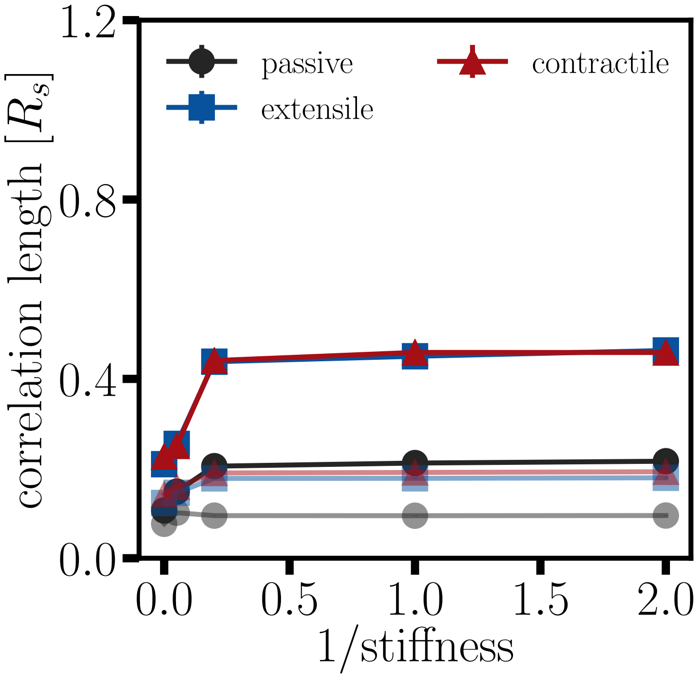

FIGURE 4.14: Plot of the correlation length as a function of shell stiffness for time windows $\Delta\tau = 5, 50$. Here $N_C = 2500$, $N_L = 50$, and $M = 5$.

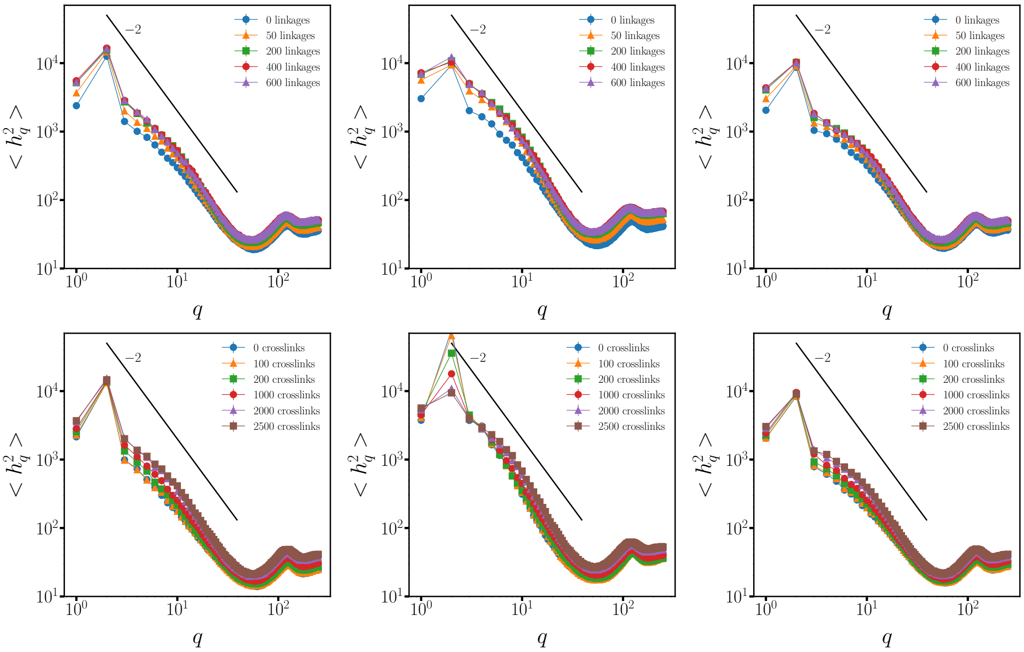

FIGURE 4.15: Shape fluctuation of a random slab at the end of simulation as a function of number of boundary linkages(top) or cross links(bottom). Left: Extensile motor case. Middle: Contractile motor case. Right: Passive case

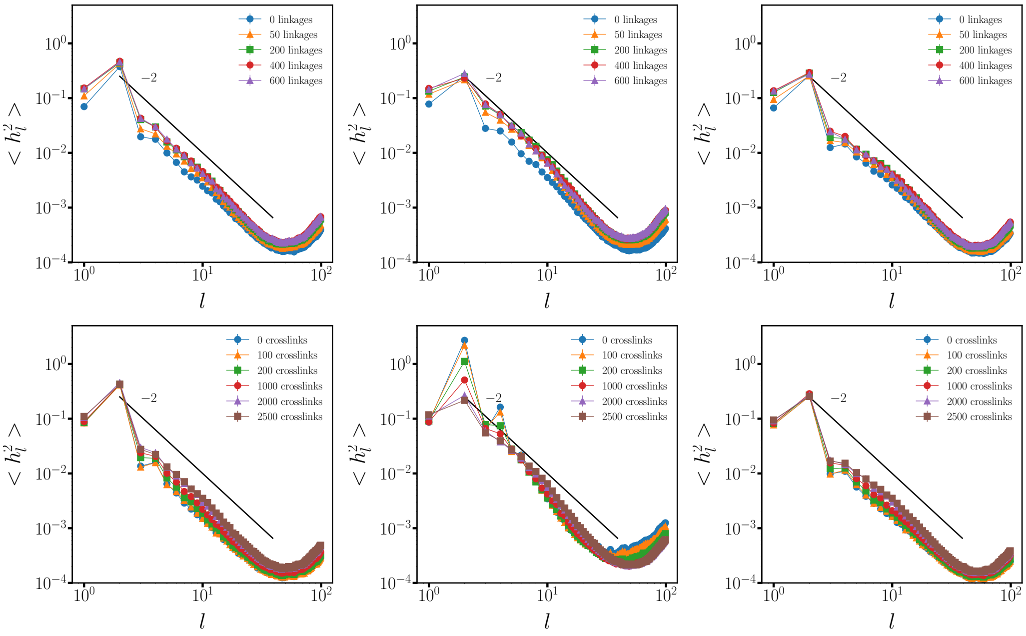

FIGURE 4.16: Power spectrum of the shape fluctuations in spherical harmonics, where l is the dimensionless spherical wavenumber for different chromatin-lamina linkages (top row) or crosslinks (bottom row). Left column: Extensile motor case. Middle column: Contractile motor case. Right column: Passive case.

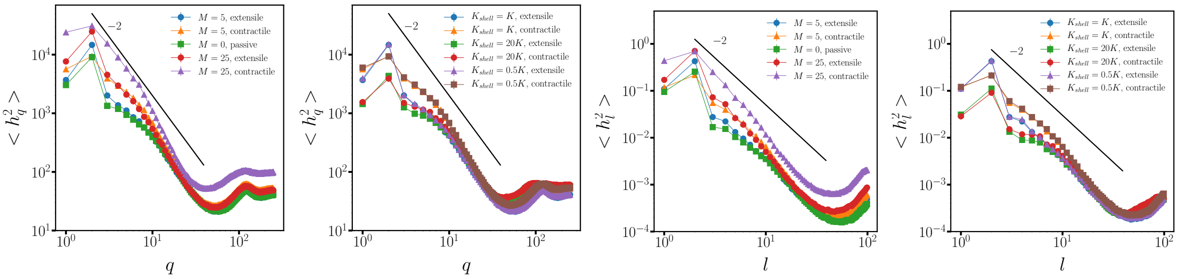

FIGURE 4.17: Power spectrum of the shape fluctuations for different motor strengths or shell stiffnesses. Left two: q plot. Right two: Y_{lm} plot.

Chapter 5

Discussion

So far, we have presented some history and some new insights into the rigidity/jamming transition in frictional packings and into the mechanims driving correlated chromatin dynamics and its affect on nuclear shape fluctuations. There are many next steps. Specifically, following my work, further research can be conducted in directions discussed briefly below:

While the relationship between rigidity percolation and the jamming transition is close, given the similar, static mechanical properties, there are also differences. For example, the springs in rigidity percolation are permanent, while in granular packings, there are rearrangements. Understanding the interplay between instantaneous topological properties and dynamical properties over some time scale is challenging but necessary if we are to make headway into predicting granular properties. One can implement rearrangements in networks and ask how the rigidity changes with time in a controlled way.

The feature that the pebble game algorithm requires only information about the topological constraints makes it a useful tool. So far, in two-dimensional central-force rigidity percolation problems, the (2,3) pebble game is a hundred percent success. With our frictional (3,3) pebble game, the algorithm is not rigorous, but reasonable near the transition. Variations of the frictional (3,3) pebble game can be implemented to make it more rigorous in two dimensions. It would be awesome to extend the frictional (3,3) pebble game to three dimensions. For the (3,6) pebble in three dimensions, there are known counterexamples hindering the rigor of the algorithm (rooted in Laman's theorem extended to three dimensions).

In chapter 4, our numerical results show that with chromatin crosslinks, the mean-squared displacement of the chromatin cross overs to a very small anomalous diffusion exponent over some time scale. It may be that the system is becoming glassy. It would be interesting to investigate that how such a glassy state responds to different types of external perturbations. Given the low packing fraction, there is plenty of space for the polymer to reconfigure if we shear it, compress it, or put spiral motors to stir it. Watching the near glassy state break would be an interesting avenue of research.

The nuclear envelope contains and protects genetic material. It also interacts with cytoskeleton from the "outside" to affect nuclear shape fluctuations and even form nuclear blebs. Thus, we must to understand more dynamical features of nuclear envelope in terms of nuclear bleb formation. In our chromatin model, we incorporated boundary linkages between the deformable shell and chromatin, to focus on the interplay between the nuclear envelope and the "stuff" inside the cell nucleus. It would be important to extend this model to contain external perturbations. These perturbations could come from localized poking or pulling by cytoskeletal fibers on the outside. There is also the possibility that the environment exerts a large-scale pressure on nucleus. Taking these additional factors into account, we can then ask how the nuclear envelope will deform under competition between the inside and the outside to arrive at a more complete understanding of nuclear structure.

Finally, I have presented this thesis in two acts. Could one not consider bridging the gap between these two acts? Indeed, there has been study of the jamming of granular chains [166]. Of course, it seems that a jammed/rigid cell nucleus would be a dead cell nucleus and so perhaps we could arrive at quantitative understanding of what sets the size of a cell nucleus and its chromatin packing fraction by invoking the principle of preventing chromatin from jamming!

Bibliography

[1] Walter H. Stockmayer. "Theory of Molecular Size Distribution and Gel Formation in Branched Polymers II. General Cross Linking". In: *J. Chem. Phys.* 12 (1944), p. 125.

[2] Paul J. Flory. "Molecular Size Distribution in Three Dimensional Polymers. I. Gelation". In: *J. Am. Chem. Soc.* 63 (1941), pp. 3083–3090.

[3] J. Adler. "Bootstrap percolation". In: *Physica A: Statistical Mechanics and its Applications* 171 (1991), pp. 453–621.

[4] A. Aharony and D. Stauffer. *Introduction to Percolation Theory*. 1994.

[5] Iwan Jensen. "Enumerations of Lattice Animals and Trees". In: *Journal of Statistical Physics* 102 (2001), pp. 865–881.

[6] Shechao Feng and Pabitra N. Sen. "Percolation on Elastic Networks: New Exponent and Threshold". In: *Phys. Rev. Lett.* 52 (3 1984), pp. 216–219. DOI: `10.1103/PhysRevLett.52.216`. URL: `https://link.aps.org/doi/10.1103/PhysRevLett.52.216`.

[7] Shechao Feng, M. F. Thorpe, and E. Garboczi. "Effective-medium theory of percolation on central-force elastic networks". In: *Phys. Rev. B* 31 (1 1985), pp. 276–280. DOI: `10.1103/PhysRevB.31.276`. URL: `https://link.aps.org/doi/10.1103/PhysRevB.31.276`.

[8] Kuang Liu, S. Henkes, and J. M. Schwarz. "Frictional Rigidity Percolation: A New Universality Class and Its Superuniversal Connections through Minimal Rigidity Proliferation". In: *Phys. Rev. X* 9 (2 2019), p. 021006. DOI: 10.1103/PhysRevX.9.021006. URL: https://link.aps.org/doi/10.1103/PhysRevX.9.021006.

[9] M. F. Thorpe and R. B. Stinchcombe. "Two exact soluble models of Rigidity Percolation". In: *Phil. Trans. A Math. Phys. Eng. Sci.* 372 (2014). URL: https://doi.org/10.1098/rsta.2012.0038.

[10] J. Clerk Maxwell F.R.S. "L. On the calculation of the equilibrium and stiffness of frames". In: *The London, Edinburgh, and Dublin Philosophical Magazine and Journal of Science* 27.182 (1864), pp. 294–299. DOI: 10.1080/14786446408643668. URL: https://doi.org/10.1080/14786446408643668.

[11] G. Laman. "On graphs and the rigidity of plane skeletal structures". In: *J. Eng. Math.* 4 (1970), p. 331. URL: https://link.springer.com/article/10.1007\%2FBF01534980.

[12] S. Pellegrino and C. R. Calladine. "Matrix analysis of statically and kinematically indeterminate frameworks". In: *Int. J. Solids Structures* 22 (1986), p. 409.

[13] D. J. Jacobs and M. F. Thorpe. "Generic Rigidity Percolation: The Pebble Game". In: *Phys. Rev. Lett.* 75 (22 1995), pp. 4051–4054. DOI: 10.1103/PhysRevLett.75.4051. URL: https://link.aps.org/doi/10.1103/PhysRevLett.75.4051.

[14] D. J. Jacobs and M. F. Thorpe. "Generic rigidity percolation in two dimensions". In: *Phys. Rev. E* 53 (4 1996), pp. 3682–3693. DOI: 10.1103/PhysRevE.53.3682. URL: https://link.aps.org/doi/10.1103/PhysRevE.53.3682.

[15] C. Moukarzel and P. M. Duxbury. "Stressed Backbone and Elasticity of Random Central-Force Systems". In: *Phys. Rev. Lett.* 75 (22 1995), pp. 4055–4058. DOI:

10.1103/PhysRevLett.75.4055. URL: https://link.aps.org/doi/10.1103/PhysRevLett.75.4055.

[16] Leyou Zhang et al. "Rigidity percolation by next-nearest-neighbor bonds on generic and regular isostatic lattices". In: *Phys. Rev. E* 91 (3 2015), p. 032124. DOI: 10.1103/PhysRevE.91.032124. URL: https://link.aps.org/doi/10.1103/PhysRevE.91.032124.

[17] P. N. Pusey and W. van Megen. "Observation of a glass transition in suspensions of spherical colloidal particles". In: *Phys. Rev. Lett.* 59 (18 1987), pp. 2083–2086. DOI: 10.1103/PhysRevLett.59.2083. URL: https://link.aps.org/doi/10.1103/PhysRevLett.59.2083.

[18] A M Kraynik. "Foam Flows". In: *Annual Review of Fluid Mechanics* 20.1 (1988), pp. 325–357. DOI: 10.1146/annurev.fl.20.010188.001545. URL: https://doi.org/10.1146/annurev.fl.20.010188.001545.

[19] F. Bolton and D. Weaire. "Rigidity loss transition in a disordered 2D froth". In: *Phys. Rev. Lett.* 65 (27 1990), pp. 3449–3451. DOI: 10.1103/PhysRevLett.65.3449. URL: https://link.aps.org/doi/10.1103/PhysRevLett.65.3449.

[20] D. J. Durian. "Foam Mechanics at the Bubble Scale". In: *Phys. Rev. Lett.* 75 (26 1995), pp. 4780–4783. DOI: 10.1103/PhysRevLett.75.4780. URL: https://link.aps.org/doi/10.1103/PhysRevLett.75.4780.

[21] Andrea J. Liu and Sidney R. Nagel. "Jamming is not just cool anymore". In: *Nature* 396 (1998), pp. 21–22. URL: https://www.nature.com/articles/23819.

[22] Corey S. O'Hern et al. "Jamming at zero temperature and zero applied stress: The epitome of disorder". In: *Phys. Rev. E* 68 (1 2003), p. 011306. DOI: 10.1103/PhysRevE.68.011306. URL: https://link.aps.org/doi/10.1103/PhysRevE.68.011306.

[23] T. S. Majmudar et al. "Jamming Transition in Granular Systems". In: *Phys. Rev. Lett.* 98 (5 2007), p. 058001. DOI: `10.1103/PhysRevLett.98.058001`. URL: `https://link.aps.org/doi/10.1103/PhysRevLett.98.058001`.

[24] Michio Otsuki and Hisao Hayakawa. "Critical scaling near jamming transition for frictional granular particles". In: *Phys. Rev. E* 83 (5 2011), p. 051301. DOI: `10.1103/PhysRevE.83.051301`. URL: `https://link.aps.org/doi/10.1103/PhysRevE.83.051301`.

[25] Dapeng Bi et al. "Jamming by shear". In: *Nature* 480 (2011), pp. 355–358. URL: `https://www.nature.com/articles/nature10667`.

[26] Silke Henkes et al. "Rigid Cluster Decomposition Reveals Criticality in Frictional Jamming". In: *Phys. Rev. Lett.* 116 (2 2016), p. 028301. DOI: `10.1103/PhysRevLett.116.028301`. URL: `https://link.aps.org/doi/10.1103/PhysRevLett.116.028301`.

[27] Shelley Sazer and Helmut Schiessel. "The Biology and Polymer Physics Underlying Large Scale Chromosome Organization". In: *Traffic* 19 (Nov. 2017). DOI: `10.1111/tra.12539`.

[28] Gary Felsenfeld and Mark Groudine. "Controlling the double helix". In: *Nature* 421 (2003), pp. 448–453.

[29] Erez Lieberman-Aiden et al. "Comprehensive Mapping of Long-Range Interactions Reveals Folding Principles of the Human Genome". In: *Science* 326.5950 (2009), pp. 289–293. ISSN: 0036-8075. DOI: `10.1126/science.1181369`. eprint: `https://science.sciencemag.org/content/326/5950/289.full.pdf`. URL: `https://science.sciencemag.org/content/326/5950/289`.

[30] A. Y. Grosberg, S. K. Nechaev, and E. I. Shakhnovich. “The role of topological constraints in the kinetics of collapse of macromolecules”. In: *J. Phys. France* 49 (1988), pp. 2095–2100.

[31] A. Grosberg et al. “Crumpled globule model of the three-dimensional structure of DNA”. In: *Europhys. Lett.* 23 (1993), pp. 373–378.

[32] Mirny LA. “The fractal globule as a model of chromatin architecture in the cell”. In: *Chromosome Res.* 19 (2011), pp. 37–51.

[33] Alexandra Zidovska, David A. Weitz, and Timothy J. Mitchison. “Micron-scale coherence in interphase chromatin dynamics”. In: *Proceedings of the National Academy of Sciences* 110.39 (2013), pp. 15555–15560. ISSN: 0027-8424. DOI: `10.1073/pnas.1220313110`. eprint: `https://www.pnas.org/content/110/39/15555.full.pdf`. URL: `https://www.pnas.org/content/110/39/15555`.

[34] M. Doi and S. F. Edwards. *The Theory of Polymer Dynamics*. Oxford Science Publications, 1986.

[35] Dino Osmanovic and Yitzhak Rabin. “Dynamics of active Rouse chains”. In: *Soft Matter* 13 (2017), p. 963.

[36] David Saintillan, Michael J. Shelley, and Alexandra Zidovska. “Extensile motor activity drives coherent motions in a model of interphase chromatin”. In: *Proceedings of the National Academy of Sciences* 115.45 (2018), pp. 11442–11447. ISSN: 0027-8424. DOI: `10.1073/pnas.1807073115`. eprint: `https://www.pnas.org/content/115/45/11442.full.pdf`. URL: `https://www.pnas.org/content/115/45/11442`.

[37] Fabian Erdel et al. “Mouse Heterochromatin Adopts Digital Compaction States without Showing Hallmarks of HP1-Driven Liquid-Liquid Phase Separation”. In: *Molecular Cell* 78.2 (2020), 236 –249.e7. ISSN: 1097-2765. DOI: `https://doi.`

org/10.1016/j.molcel.2020.02.005. URL: http://www.sciencedirect.com/science/article/pii/S1097276520300757.

[38] Edward J. Banigan, Andrew D. Stephens, and John F. Marko. "Mechanics and Buckling of Biopolymeric Shells and Cell Nuclei". In: *Biophysical Journal* 113.8 (2017), pp. 1654 –1663. ISSN: 0006-3495. DOI: https://doi.org/10.1016/j.bpj.2017.08.034. URL: http://www.sciencedirect.com/science/article/pii/S0006349517309293.

[39] Yagmur Turgay et al. "The molecular architecture of lamins in somatic cells". In: *Nature* 543 (2017), pp. 261–264.

[40] Julia Mahamid et al. "Visualizing the molecular sociology at the HeLa cell nuclear periphery". In: *Science* 351.6276 (2016), pp. 969–972. ISSN: 0036-8075. DOI: 10.1126/science.aad8857. eprint: https://science.sciencemag.org/content/351/6276/969.full.pdf. URL: https://science.sciencemag.org/content/351/6276/969.

[41] Ryosuke Nagashima et al. "Single nucleosome imaging reveals loose genome chromatin networks via active RNA polymerase II". In: *J Cell Biol.* 218 (2019), pp. 1511–1530.

[42] R. R. Tremblay, A. R. Day, and A. M. S. Tremblay. "Splay Rigidity in the Diluted Central-Force Elastic Network". In: *Phys. Rev. Lett.* 56 (13 1986), pp. 1425–1425. DOI: 10.1103/PhysRevLett.56.1425. URL: https://link.aps.org/doi/10.1103/PhysRevLett.56.1425.

[43] A. R. Day, R. R. Tremblay, and A. M. S. Tremblay. "Rigid Backbone: A New Geometry for Percolation". In: *Phys. Rev. Lett.* 56 (23 1986), pp. 2501–2504. DOI: 10.1103/PhysRevLett.56.2501. URL: https://link.aps.org/doi/10.1103/PhysRevLett.56.2501.

[44] Stéphane Roux and Alex Hansen. "Surface exponent in percolation and central-force percolation: A test for splay rigidity". In: *Phys. Rev. B* 38 (7 1988), pp. 5170–5173. DOI: `10.1103/PhysRevB.38.5170`. URL: `https://link.aps.org/doi/10.1103/PhysRevB.38.5170`.

[45] Donald J. Jacobs and Bruce Hendrickson. "An Algorithm for Two-Dimensional Rigidity Percolation: The Pebble Game". In: *Journal of Computational Physics* 137.2 (1997), pp. 346 –365. ISSN: 0021-9991. DOI: `https://doi.org/10.1006/jcph.1997.5809`. URL: `http://www.sciencedirect.com/science/article/pii/S0021999197958095`.

[46] Cyril Domb and Joel Lebowitz. *Phase Transitions and Critical Phenomena*. Academic Press, 2000. ISBN: 9780122203183.

[47] C. Moukarzel, P. M. Duxbury, and P. L. Leath. "First-order rigidity on Cayley trees". In: *Phys. Rev. E* 55 (5 1997), pp. 5800–5811. DOI: `10.1103/PhysRevE.55.5800`. URL: `https://link.aps.org/doi/10.1103/PhysRevE.55.5800`.

[48] C. Moukarzel and P. M. Duxbury. "Comparison of rigidity and connectivity percolation in two dimensions". In: *Phys. Rev. E* 59 (3 1999), pp. 2614–2622. DOI: `10.1103/PhysRevE.59.2614`. URL: `https://link.aps.org/doi/10.1103/PhysRevE.59.2614`.

[49] M. V. Chubynsky and M. F. Thorpe. "Algorithms for three-dimensional rigidity analysis and a first-order percolation transition". In: *Phys. Rev. E* 76 (4 2007), p. 041135. DOI: `10.1103/PhysRevE.76.041135`. URL: `https://link.aps.org/doi/10.1103/PhysRevE.76.041135`.

[50] Yacov Kantor and Itzhak Webman. "Elastic Properties of Random Percolating Systems". In: *Phys. Rev. Lett.* 52 (21 1984), pp. 1891–1894. DOI: `10.1103/`

PhysRevLett.52.1891. URL: https://link.aps.org/doi/10.1103/PhysRevLett.52.1891.

[51] Shechao Feng and Muhammad Sahimi. “Position-space renormalization for elastic percolation networks with bond-bending forces”. In: *Phys. Rev. B* 31 (3 1985), pp. 1671–1673. DOI: 10.1103/PhysRevB.31.1671. URL: https://link.aps.org/doi/10.1103/PhysRevB.31.1671.

[52] Lawrence M. Schwartz et al. “Behavior of depleted elastic networks: Comparison of effective-medium and numerical calculations”. In: *Phys. Rev. B* 32 (7 1985), pp. 4607–4617. DOI: 10.1103/PhysRevB.32.4607. URL: https://link.aps.org/doi/10.1103/PhysRevB.32.4607.

[53] Jian Wang. “The bond bending model on triangular lattice and square lattice”. In: *Z. Physik B* 101 (1996), pp. 141–144.

[54] Moumita Das, D. A. Quint, and J. M. Schwarz. “Redundancy and Cooperativity in the Mechanics of Compositely Crosslinked Filamentous Networks”. In: *PLOS ONE* 7.5 (May 2012), pp. 1–11. DOI: 10.1371/journal.pone.0035939. URL: https://doi.org/10.1371/journal.pone.0035939.

[55] D. A. Head, F. C. MacKintosh, and A. J. Levine. “Nonuniversality of elastic exponents in random bond-bending networks”. In: *Phys. Rev. E* 68 (2 2003), p. 025101. DOI: 10.1103/PhysRevE.68.025101. URL: https://link.aps.org/doi/10.1103/PhysRevE.68.025101.

[56] T. S. Majmudar et al. “Jamming Transition in Granular Systems”. In: *Phys. Rev. Lett.* 98 (5 2007), p. 058001. DOI: 10.1103/PhysRevLett.98.058001. URL: https://link.aps.org/doi/10.1103/PhysRevLett.98.058001.

[57] Wouter G. Ellenbroek et al. “Rigidity Loss in Disordered Systems: Three Scenarios”. In: *Phys. Rev. Lett.* 114 (13 2015), p. 135501. DOI: 10.1103/PhysRevLett.

114.135501. URL: https://link.aps.org/doi/10.1103/PhysRevLett.114.135501.

[58] M van Hecke. “Jamming of soft particles: geometry, mechanics, scaling and isostaticity”. In: *Journal of Physics: Condensed Matter* 22.3 (2009), p. 033101. DOI: 10.1088/0953-8984/22/3/033101. URL: https://doi.org/10.1088\%2F0953-8984\%2F22\%2F3\%2F033101.

[59] Andrea J. Liu and Sidney R. Nagel. “The Jamming Transition and the Marginally Jammed Solid”. In: *Annual Review of Condensed Matter Physics* 1.1 (2010), pp. 347–369. DOI: 10.1146/annurev-conmatphys-070909-104045.

[60] A. J. Liu et al. *The jamming scenario-an introduction and outlook*. URL: https://arxiv.org/abs/1006.2365.

[61] Kostya Shundyak, Martin van Hecke, and Wim van Saarloos. “Force mobilization and generalized isostaticity in jammed packings of frictional grains”. In: *Phys. Rev. E* 75 (1 2007), p. 010301. DOI: 10.1103/PhysRevE.75.010301. URL: https://link.aps.org/doi/10.1103/PhysRevE.75.010301.

[62] S. Henkes, M. van Hecke, and W. van Saarloos. “Critical jamming of frictional grains in the generalized isostaticity picture”. In: *EPL (Europhysics Letters)* 90.1 (2010), p. 14003. DOI: 10.1209/0295-5075/90/14003. URL: https://doi.org/10.1209\%2F0295-5075\%2F90\%2F14003.

[63] George Y. Onoda and Eric G. Liniger. “Random loose packings of uniform spheres and the dilatancy onset”. In: *Phys. Rev. Lett.* 64 (22 1990), pp. 2727–2730. DOI: 10.1103/PhysRevLett.64.2727. URL: https://link.aps.org/doi/10.1103/PhysRevLett.64.2727.

[64] J. M Schwarz, A. J Liu, and L. Q Chayes. “The onset of jamming as the sudden emergence of an infinitek-core cluster”. In: *Europhysics Letters (EPL)* 73.4 (2006),

pp. 560–566. DOI: 10.1209/epl/i2005-10421-7. URL: https://doi.org/10.1209\%2Fepl\%2Fi2005-10421-7.

[65] J. Barré. "Hierarchical models of rigidity percolation". In: *Phys. Rev. E* 80 (6 2009), p. 061108. DOI: 10.1103/PhysRevE.80.061108. URL: https://link.aps.org/doi/10.1103/PhysRevE.80.061108.

[66] Miron Kaufman and Robert B. Griffiths. "Exactly soluble Ising models on hierarchical lattices". In: *Phys. Rev. B* 24 (1 1981), pp. 496–498. DOI: 10.1103/PhysRevB.24.496. URL: https://link.aps.org/doi/10.1103/PhysRevB.24.496.

[67] D Wilkinson and J F Willemsen. "Invasion percolation: a new form of percolation theory". In: *Journal of Physics A: Mathematical and General* 16.14 (1983), pp. 3365–3376. DOI: 10.1088/0305-4470/16/14/028. URL: https://doi.org/10.1088\%2F0305-4470\%2F16\%2F14\%2F028.

[68] L. Henneberg. *Die graphische Statik der starren Systeme*. 1911.

[69] P. L. Leath. "Cluster size and boundary distribution near percolation threshold". In: *Phys. Rev. B* 14 (11 1976), pp. 5046–5055. DOI: 10.1103/PhysRevB.14.5046. URL: https://link.aps.org/doi/10.1103/PhysRevB.14.5046.

[70] D Wilkinson and M Barsony. "Monte Carlo study of invasion percolation clusters in two and three dimensions". In: *Journal of Physics A: Mathematical and General* 17.3 (1984), pp. L129–L135. DOI: 10.1088/0305-4470/17/3/007. URL: https://doi.org/10.1088\%2F0305-4470\%2F17\%2F3\%2F007.

[71] Carl P. Goodrich, Andrea J. Liu, and Sidney R. Nagel. "The Principle of Independent Bond-Level Response: Tuning by Pruning to Exploit Disorder for Global Behavior". In: *Phys. Rev. Lett.* 114 (22 2015), p. 225501. DOI: 10.1103/

PhysRevLett.114.225501. URL: https://link.aps.org/doi/10.1103/PhysRevLett.114.225501.

[72] Jorge H. Lopez, L. Cao, and J. M. Schwarz. "Jamming graphs: A local approach to global mechanical rigidity". In: *Phys. Rev. E* 88 (6 2013), p. 062130. DOI: 10.1103/PhysRevE.88.062130. URL: https://link.aps.org/doi/10.1103/PhysRevE.88.062130.

[73] Dion J. Koeze and Brian P. Tighe. "Sticky Matters: Jamming and Rigid Cluster Statistics with Attractive Particle Interactions". In: *Phys. Rev. Lett.* 121 (18 2018), p. 188002. DOI: 10.1103/PhysRevLett.121.188002. URL: https://link.aps.org/doi/10.1103/PhysRevLett.121.188002.

[74] Estelle Berthier et al. "Rigidity percolation control of the brittle-ductile transition in disordered networks". In: *Phys. Rev. Materials* 3 (7 2019), p. 075602. DOI: 10.1103/PhysRevMaterials.3.075602. URL: https://link.aps.org/doi/10.1103/PhysRevMaterials.3.075602.

[75] Daniel Lester and Ruru Li. "The frictional pebble game: An algorithm for rigidity percolation in saturated frictional assemblies". In: *Journal of Computational Physics* 369 (2018), pp. 225 –236. ISSN: 0021-9991. DOI: https://doi.org/10.1016/j.jcp.2018.05.016. URL: http://www.sciencedirect.com/science/article/pii/S0021999118303085.

[76] R. D'Souza and J. Nagler. "Anomalous critical and supercritical phenomena in explosive percolation". In: *Nat. Phys.* 11 (2015), pp. 531 –538.

[77] Shlomo Alexander. In: *Physics Reports* 296 (1998), p. 65.

[78] T. C. Lubensky et al. In: *Reports on Progress in Physics* 78.7 (2015), pp. 1–30.

[79] S. Dagois-Bohy et al. In: *Phys. Rev. Lett.* 109 (2012), p. 095703.

[80] C. P. Goodrich et al. In: *Phys. Rev. E* 90 (2014), p. 022138.

[81] Leonardo E Silbert et al. "Geometry of frictionless and frictional sphere packings". In: *Phys. Rev. E* 65.3 (2002), p. 031304.

[82] Kostya Shundyak, Martin van Hecke, and Wim van Saarloos. "Force mobilization and generalized isostaticity in jammed packings of frictional grains". In: *Phys. Rev. E* 75.1 (2007), p. 010301.

[83] Leonardo E Silbert, Andrea J Liu, and Sidney R Nagel. "Vibrations and diverging length scales near the unjamming transition". In: *Phys. Rev. Lett.* 95.9 (2005), p. 098301.

[84] Ellák Somfai et al. "Critical and noncritical jamming of frictional grains". In: *Phys. Rev. E* 75.2 (2007), p. 020301.

[85] Liu Wenwei et al. "Equation of state for random sphere packings with arbitrary adhesion and friction". In: *Soft Matter* 13 (2017), p. 421.

[86] Harukuni Ikeda et al. "Jamming with Tunable Roughness". In: *Phys. Rev. Lett.* 124 (20 2020), p. 208001.

[87] Wouter G Ellenbroek et al. "Rigidity loss in disordered systems: Three scenarios". In: *Phys. Rev. Lett.* 114.13 (2015), p. 135501.

[88] Shang Zhang et al. "Correlated rigidity percolation and colloidal gels". In: *Phys. Rev. Lett.* 123.5 (2019), p. 058001.

[89] R Li and D. R. Lester. "Hierarchical Jamming in Frictional Particle Assemblies". In: *arxiv:2002.00313* (2020).

[90] H. A. Vinutha and Srikanth Sastry. "Force networks and jamming in shear-deformed sphere packings". In: *Phys. Rev. E* 99 (1 2019), p. 012123. DOI: `10.1103/PhysRevE.99.012123`. URL: `https://link.aps.org/doi/10.1103/PhysRevE.99.012123`.

[91] James G. Puckett and Karen E. Daniels. “Equilibrating Temperaturelike Variables in Jammed Granular Subsystems”. In: *Phys. Rev. Lett.* 110.5 (2013), p. 058001.

[92] Ephraim S. Bililign, Jonathan E. Kollmer, and Karen E. Daniels. “Protocol Dependence and State Variables in the Force-Moment Ensemble”. en. In: *Phys. Rev. Lett.* 122.3 (Jan. 2019). (Visited on 01/25/2019).

[93] Karen E. Daniels, Jonathan E. Kollmer, and James G. Puckett. “Photoelastic force measurements in granular materials”. In: *Review of Scientific Instruments* 88.5 (May 2017), p. 051808. (Visited on 05/26/2017).

[94] Aghil Abed Zadeh and *et al.* “Enlightening force chains: a review of photoelasticimetry in granular matter”. en. In: *Granular Matter* 21.4 (2019), p. 83. (Visited on 11/21/2019).

[95] Hu Zheng, Joshua A. Dijksman, and R. P. Behringer. “Shear jamming in granular experiments without basal friction”. In: *EPL* 107.3 (2014), p. 34005.

[96] Jonathan E. Kollmer. *Photo-Elastic Granular Solver (PEGS)*. https://github.com/jekollmer/PE

[97] W. M. Rand. “Objective criteria for the evaluation of clustering methods”. In: *Journal of the American Statistical Association* 66.336 (1971), p. 846.

[98] L. Hubert and P. Arabie. “Comparing partitions”. In: *Journal of Classification* 2.1 (1985), p. 193.

[99] George Y. Onoda and Eric G. Liniger. “Random loose packings of uniform spheres and the dilatancy onset”. en. In: *Phys. Rev. Lett.* 64.22 (May 1990), pp. 2727–2730. (Visited on 08/06/2019).

[100] Stefanos Papanikolaou, Corey S. O’Hern, and Mark D. Shattuck. “Isostaticity at Frictional Jamming”. In: *Phys. Rev. Lett.* 110 (19 2013), p. 198002.

[101] M. Wyart, S. R. Nagel, and T. A. Witten. “Geometric origin of excess low-frequency vibrational modes in weakly connected amorphous solids”. en. In: *EPL (Europhysics Letters)* 72.3 (Nov. 2005), p. 486. (Visited on 09/10/2013).

[102] C.-H. Liu et al. “Force Fluctuations in Bead Packs”. In: *Science* 269.5223 (1995), pp. 513–515.

[103] Daniel Howell, R. P. Behringer, and Christian Veje. “Stress Fluctuations in a 2D Granular Couette Experiment: A Continuous Transition”. In: *Phys. Rev. Lett.* 82 (26 1999), pp. 5241–5244.

[104] K. P. Krishnaraj and Prabhu R. Nott. “Coherent Force Chains in Disordered Granular Materials Emerge from a Percolation of Quasilinear Clusters”. In: *Phys. Rev. Lett.* 124 (19 2020), p. 198002.

[105] Antoinette Tordesillas, David M. Walker, and Qun Lin. “Force cycles and force chains”. In: *Phys. Rev. E* 81 (1 2010), p. 011302.

[106] Chad Giusti et al. “Topological and geometric measurements of force-chain structure”. In: *Phys. Rev. E* 94 (3 2016), p. 032909.

[107] Jennifer M. Rieser et al. “Divergence of Voronoi Cell Anisotropy Vector: A Threshold-Free Characterization of Local Structure in Amorphous Materials”. In: *Phys. Rev. Lett.* 116 (8 2016), p. 088001.

[108] Sumantra Sarkar et al. “Shear-induced rigidity of frictional particles: Analysis of emergent order in stress space”. In: *Phys. Rev. E* 93 (4 2016), p. 042901.

[109] M. Wyart and M. E. Cates. “Discontinuous Shear Thickening without Inertia in Dense Non-Brownian Suspensions”. In: *Phys. Rev. Lett.* 112 (9 2014), p. 098302.

[110] Romain Mari et al. “Discontinuous shear thickening in Brownian suspensions by dynamic simulation”. In: *Proceedings of the National Academy of Sciences* 112.50 (2015), pp. 15326–15330.

[111] B. Servatius and H. Servatius. *Rigidity Theory and Applications*. Ed. by M. F. Thorpe and P. M. Duxbury. Kluwer Academic/Plenum Publishers, 1999.

[112] T.-S. Tay. “Rigidity of multi-graphs I. linking rigid bodies in n-space”. In: *J. Comb. Theory Ser. B* 36 (1984), pp. 95–112.

[113] A. Lee and I. Streinu. “Pebble game algorithms and sparse graphs”. In: *Discrete Mathematics* 308 (8 2008), pp. 1425–1437.

[114] S. Henkes. *Rigid Library*. https://github.com/silkehenkes/RigidLibrary.

[115] P.A. Cundall and O. D. L. Strack. In: *G/'eotechnique* 29 (1 1979), pp. 47–65.

[116] N.W. Ashcroft and N.D. Mermin. *Solid State Physics*. Philadelphia: Saunders College, 1976.

[117] Andrea J. Liu and Sidney R. Nagel. “The Jamming Transition and the Marginally Jammed Solid”. In: *Annual Review of Condensed Matter Physics* 1.1 (Aug. 2010), pp. 347–369.

[118] K. L. Johnson. *Contact Mechanics*. Cambridge University Press, May 1985. (Visited on 01/27/2020).

[119] JH Irving and John G Kirkwood. “The statistical mechanical theory of transport processes. IV. The equations of hydrodynamics”. In: *The Journal of chemical physics* 18.6 (1950), pp. 817–829.

[120] J. H. Gibcus and J. Dekker. “The hierarchy of the 3D genome”. In: *Mol. Cell* 49.5 (2013), pp. 773–782.

[121] A. Zidovska, D. Weitz, and T. Mitchison. “Micron-scale coherence in interphase chromatin dynamics”. In: *Proc. Natl. Acad. Sci. U. S. A.* 110 (2013), pp. 15555–15560.

[122] Shaban H. A., R. Barth, and K. Bystricky. "Formation of correlated chromatin domains at nanoscale dynamic resolution during transcription". In: *Nucleic Acids Res.* 46 (2018), pp. 11202–11212.

[123] D. Saintillan, M. J. Shelley, and A. Zidovska. "Extensile motor activity drives coherent motions is a model of interphase chromatin". In: *Proc. Natl. Acad. Sci. U. S. A.* 115 (2018), pp. 11442–11447.

[124] R. Barth, K. Bystricky, and H. A. Shaban. "Coupling chromatin structure and dynamics by live super-resolution imaging". In: *Sci. Adv.* 6 (2020), eaaz2196.

[125] H. A. Shaban et al. "Hi-D: nanoscale mapping of nuclear dynamics in single living cells". In: *Genome Biol.* 21 (2020), pp. 1–21.

[126] T. Shimi et al. "Structural organization of nuclear lamins A, C, B1, and B2 revealed by superresolution microscopy". In: *Mol. Biol. Cell* 26 (2015), pp. 4075–4086.

[127] J. Mahamid and et al. "Visualizing the molecular sociology at the HeLa cell nuclear periphery". In: *Science* 351 (2016), pp. 969–972.

[128] Y. Turgay and et al. "The molecular architecture of lamins in somatic cells". In: *Nature* 543 (2017), pp. 261–264.

[129] T. Dechat and et al. "Nuclear lamins: major factors in the structural organization and function of the nucleus and chromatin". In: *Genes Dev.* 22 (2008), pp. 832–853.

[130] I. Solovei and et al. "LBR and lamin A/C sequentially tether peripheral heterochromatin and inversely regulate differentiation". In: *Cell* 152 (2013), pp. 584–598.

[131] R. de Leeuw, Y. Gruenbaum, and O. Medalia. "Nuclear lamins: thin filaments with major functions". In: *Trends Cell Biol.* 28 (2018), pp. 34–45.

[132] L. Guelen and et al. “Domain organization of human chromosomes revealed by mapping of nuclear lamina interactions”. In: *Nature* 453 (2008), pp. 948–951.

[133] B. van Steensel and A. S. Belmont. “Lamina-associated domains: Links with chromosome architecture, heterochromatin, and gene repression”. In: *Cell* 169 (2017), pp. 780–791.

[134] L. Liu et al. “Chain organization of human interphase chromosome determines the spatiotemporal dynamics of chromatin loci”. In: *PLoS Comp. Biol.* 14 (2018), e1006617.

[135] M. DiPierro et al. “Anomalous diffusion, spatial coherence, and viscoelasticity from the energy landscape of human chromosomes”. In: *Proc. Natl. Acad. Sci. U. S. A.* 115 (2018), pp. 7753–7758.

[136] F. Y. Chu, S. C. Haley, and A. Zidovska. “On the origin of shape fluctuations of the cell nucleus”. In: *Proc. Natl. Acad. Sci. U. S. A.* 114 (2017), pp. 10338–10343.

[137] C. Guilluy and et al. “Isolated nuclei adapt to force and reveal a mechanotransduction pathway in the nucleus”. In: *Nat. Cell Biol.* 16 (2014), pp. 376–381.

[138] S. M. Schreiner et al. “The tethering of chromatin to the nuclear envelope supports nuclear mechanics”. In: *Nat. Comm.* 6 (2015), p. 7159.

[139] Maria Chiara Lionetti et al. “Chromatin and cytoskeletal tethering determine nuclear morphology in progerin expressing cells”. In: *Biophys. J.* 118 (2020), pp. 3219–2332.

[140] A. D. Stephens, E. J. Banigan, and J. F. Marko. “Chromatin’s physical properties shape the nucleus and its functions”. In: *Curr. Opin. Cell Biol.* 58 (2019), pp. 76–84.

[141] I. Bronshtein and et al. “Chromatin and cytoskeletal tethering determine nuclear morphology in progerin expressing cells”. In: *Nat. Comm.* 6 (2015), p. 8044.

[142] E. J. Banigan, A. D. Stephens, and J. F. Marko. "Mechanics and buckling of biopolymeric shells and cell nuclei." Biophysical journal vol. 113,8 (2017): 1654-1663. doi:10.1016/j.bpj.2017.08.034". In: *Biophys. J.* 113 (2017), pp. 1654–1663.

[143] A. D. Stephens et al. "Chromatin and lamin A determine two different mechanical response regimes of the cell nucleus". In: *Mol. Biol. Cell* 28 (2017), pp. 1984–1996.

[144] R. Bruinsma et al. "Chromatin hydrodynamics". In: *Biophys. J.* 106 (2014), pp. 1871–1881.

[145] I. I. Cisse and et al. "Real-time dynamics of RNA polymerase II clustering in live human cells". In: *Science* 341 (2013), pp. 664–667.

[146] R. Nagashima and et al. "Single nucleosome imaging reveals loose genome chromatin networks via active RNA polymerase II". In: *J. Cell Biol.* 218 (2019), pp. 1511–1530.

[147] F. Erdel and et al. "Mouse Heterochromatin Adopts Digital Compaction States without Showing Hallmarks of HP1-Driven Liquid-Liquid Phase Separation". In: *Cell* 78 (2020), pp. 236–249.

[148] H. Belaghzal and et al. In: *biorXiv:704957* (2019).

[149] M. Paoluzzi et al. "Shape and displacement fluctuations in soft vesicles filled by active particles". In: *Sci. Reps.* 6 (2016), p. 34146.

[150] M. Rubinstein and R. H. Colby. *Polymer Physics*. New York: Oxford University Press, 2003.

[151] N. Khanna et al. "Chromosome dynamics near the sol-gel phase transition dictate the timing of remote genomic interactions". In: *Nat. Comm.* 10 (2019), p. 2771.

[152] A. E. Patteson and et al. “Vimentin protects cells against nuclear rupture and DNA damage during migration”. In: *J. Cell Biol.* 218 (2019), pp. 4079–4092.

[153] K. Keren et al. “Mechanism of shape determination in motile cells”. In: *Nature* 453.7194 (2008), pp. 475–480.

[154] J. Y. Tinevez and et al. “Role of cortical tension in bleb growth”. In: *Proc. Natl. Acad. Sci.* 106 (2009), pp. 18581–18586.

[155] E. L. Barnhart et al. “An adhesion-dependent switch between mechanisms that determine motile cell shape”. In: *PLoS Biol* 9 (2011), e1001059.

[156] C. A. Wilson and et al. “Myosin II contributes to cell-scale actin network treadmilling through network disassembly”. In: *Nature* 465 (2010), pp. 373–377.

[157] G. Koenderink and E. Paluch. “Architecture shapes contractility in actomyosin networks”. In: *Curr. Op. Cell Biol.* 50 (2018), pp. 79–85.

[158] B. J. Belin, T. Lee, and R. D. Mullins. “DNA damage induces nuclear actin filament assembly by Formin-2 and Spire-1/2 that promotes efficient DNA repair”. In: *eLIFE* 4 (2015), e07735.

[159] Stephens A. D. and et al. “Chromatin histone modifications and rigidity affect nuclear morphology independent of lamins”. In: *Mol. Biol. Cell* 29 (2018), pp. 220–233.

[160] H. D. Ou et al. “ChromEMT: Visualizing 3D chromatin structure and compaction in interphase and mitotic cells”. In: *Science* 357 (2017), (6349):eaag0025.

[161] M. Falk et al. “Heterochromatin drives compartmentalization of inverted and conventional nuclei”. In: *Nature* 570 (2019), pp. 395–399.

[162] Hongsuk Kang et al. “Confinement-Induced Glassy Dynamics in a Model for Chromosome Organization”. In: *Phys. Rev. Lett.* 115 (19 2015), p. 198102. DOI: `10.1103/PhysRevLett.115.198102`. URL: `https://link.aps.org/doi/10.1103/PhysRevLett.115.198102`.

[163] E. Lieberman-Aiden et al. “Comprehensive Mapping of Long-Range Interactions Reveals Folding Principles of the Human Genome”. In: *Science* 326 (2009), pp. 289–293.

[164] J. Dekker and L. Mirny. “The 3D genome as moderator of chromosomal communication”. In: *Cell* 164 (2016), pp. 1110–1121.

[165] L. D. Landau et al. *Theory of Elasticity*. 3rd ed. Butterworth-Heinemann, 2012.

[166] L. M. Lopatina, C. J. Olson Reichhardt, and C. Reichhardt. “Jamming in granular polymers”. In: *Phys. Rev. E* 84 (1 2011), p. 011303. DOI: `10.1103/PhysRevE.84.011303`. URL: `https://link.aps.org/doi/10.1103/PhysRevE.84.011303`.

KUANG LIU

247 Physics Building, Syracuse, NY 13244 ◇ (315)350-6890 ◇ kuangliu.physics@gmail.com kliu11@syr.edu

EDUCATION

Doctoral Program in Physics *Fall 2014 - Present*
Department of Physics, Syracuse University GPA: 3.77/4.0

Bachelor of Science, Physics *September 2009 - June 2013*
Department of Physics, Peking University GPA: 3.0/4.0

EXPERIENCE

Research Assistant *Fall 2015 - Present*
for J. M. Schwarz in Syracuse University

- Analyzed frictional rigidity percolation phase transition in two-dimensional lattice. Found a second order transition and numerically determined critical exponents depending on friction coefficients
- Developed dynamical matrix for a 2D frictional granular packing to analyze its rigidity and did comparison with results from pebble game algorithm and real experiments. Found high correlation among three approaches once system reaches isostaticity
- Assisted analysis of brittle-ductile transition in disordered networks obtained from a frictional granular packing. Found strong correlation between locations of ruptures in experiment and rigidity decomposition from (3,3) pebble game algorithm
- Developed model of chromatin dynamics using C++ and Python. Study mechanisms of coherent motion of chromatin, nuclear envelope shape fluctuation and nuclear blebbing

Teaching Assistant for PHY 211 *Spring 2015; Fall 2018*

- Responsible for leading 3 one-hour recitation sections twice per week to increase student comprehension of Introductory Newtonian Mechanics, in addition to grading

Teaching Assistant for PHY 212 *Fall 2014; Fall 2015; Spring 2019*

- Responsible for leading 3 one-hour recitation sections twice per week to increase student comprehension of Introductory Electromagnetism, in addition to grading

Teaching Assistant for PHY 221 *Spring 2016; Spring 2017*

- Responsible for leading 3 two-hour Lab sections once per week to increase student comprehension of Introductory Newtonian Mechanics, in addition to grading

Teaching Assistant for PHY 215 *Fall 2017*

- Responsible for leading 1 one-hour recitation sections twice per week to increase student comprehension of Introductory Newtonian Mechanics, in addition to grading

TECHNICAL SKILLS

Languages	C, C++, Python
Software	LaTeX, Origin, Mathematica, Matlab

PUBLICATIONS

- **”Frictional Rigidity Percolation: A New Universality Class and Its Superuniversal Connections through Minimal Rigidity Proliferation”**
  Kuang Liu, Silke E. Henkes, and J. M. Schwarz
  Phys. Rev. X **9**, 021006

- **”Rigidity percolation control of the brittle-ductile transition in disordered networks”**
  Estelle Berthier, Jonathan E. Kollmer, Silke E. Henkes, Kuang Liu, J. M. Schwarz, and Karen E. Daniels
  Phys. Rev. Materials **3**, 075602

- **”Sponge-like rigid structures in frictional granular packings”**
  Kuang Liu, Jonathan E. Kollmer, Karen E. Daniels, J. M. Schwarz, and Silke E. Henkes
  arxiv:2006.00557 *in peer review*

- **”Dynamic nuclear structure emerges from chromatin crosslinks and motors”**
  Kuang Liu, Alison E. Patteson, Edward J. Banigan, and J. M. Schwarz
  arxiv:2008.07417

REFERENCES

J. M. Schwarz
229A Physics Building,
Dept. of Physics
Syracuse University
Syracuse, NY 13244
jmschw02@syr.edu (Phone: 607.342.0876)

Silke Henkes
School of Mathematics
University of Bristol
University Walk, Clifton
Bristol BS8 1TW
silke.henkes@bristol.ac.uk

Alison Patteson
229C Physics Building,
Dept. of Physics
Syracuse University
Syracuse, NY 13244
aepattes@syr.edu

Welcome to my website